BRNO UNIVERSITY OF TECHNOLOGY

FACULTY OF MECHANICAL ENGINEERING

ÚSTAV MATERIÁLOVÝCH VĚD A INŽENÝRSTVÍ
INSTITUTE OF MATERIALS SCIENCE AND ENGINEERING

LOMOVÉ CHOVÁNÍ OCELÍ A JEJICH SVARŮ PRO ENERGETIKU

FRACTURE BEHAVIOR OF STEELS AND THEIR WELDS FOR POWER INDUSTRY

DISERTAČNÍ PRÁCE
DOCTORAL THESIS

AUTOR PRÁCE Ing. Samer Al Khaddour
AUTHOR

VEDOUCÍ PRÁCE Prof. Ing. Ivo Dlouhý, CSc
SUPERVISOR

BRNO 2017

Acknowledgments

I would like first to take this opportunity to express my sincere thanks and gratitude to my supervisor Prof. Ivo Dlouhý at Brno University of Technology for the continuous support of my Ph.D study and related research, for his patience, motivation, critical comments and suggestions. His guidance helped me in all the time of research and writing of this thesis.

I want to thank Dr. Zdeněk Chlup and Dr. Hynek Hadraba who have been supporting me during my doctoral studies, by helping me to understand every detail of the experiments. I greatly appreciate Dr. Luděk Stratil for generously sharing his time and knowledge. He is always ready to help with a smile. I gratefully acknowledge Ing. Pavel Čupera, Bc. Radek Vácha for the help with sample preparation and settings of machines. I am grateful to my dear colleagues, particularly those from Brittle Fracture Group in IPM for their friendship and support.

I am extremely grateful to Prof. Harry Bhadeshia and Dr. Aseel Abdulbaky Al Hamdany, Department of Materials Science and Metallurgy University of Cambridge for providing me with Software for Bayesian neural networks.

I would like to thank South Moravian Centre for International Mobility "JCMM" for the financial support which provides me the opportunity to pursue research at Brno University of Technology during my study.

I would also like to thank my parents, they were always supporting me and encouraging me with their best wishes. Finally, I would like to thank my wife, Nermin, who was always there cheering me up and stood by me through the good times and bad. Thanks to Celena the best daughter I could ever have, for her smiles encourage me to efficiently.

Abstract

The aim of the study is to verify the validity of the master curve concept for evaluation of the dissimilar weld joint and/or thermally aged weld joints. In addition, the thesis is focused on development of quantitative models for the prediction of reference temperature characterising position of the fracture toughness transition on the temperature axis using experimental data collected from tensile tests, together with a powerful computational technique known as neural network.

This study focuses on the evaluation of the fracture behaviour of welds carried out by fusion welding. It aims to investigate the fracture behaviour in transition region of the structural steels and welds with ferritic basic microstructures by means of reference temperature. In order to obtain the reference temperature artificial neural network is used exploting tensile test and hardness test data.

Creating a model using neural network method requires a sufficient amount of data and it is sometimes not possible to accomplish easily. Creating a truly general model requires a combination of data and metallurgical knowledge. So, the aim of this work is also to develop artificial neural network enabling to predict the reference temperature. In total 29 experimental data sets from low alloy steels have been applied to validate the model of reference temperature prediction. The tensile tests have been done at general yield temperature of circumferential notched tensile tests (purely general yield temperature) and at room temperature (purely ductile fracture temperature). To build the model all parameters of tensile test and hardness values were used as input variables.

The study indicated that the reference temperature characterizing the fracture toughness transition behaviour in low alloy steels with predominantly ferritic structure is predictable on the basis of selected characteristics of tensile test.

Keywords: Steels; Fracture toughness; Tensile test; Artificial neural networks; Reference temperature, Master curve.

Abstrakt

Práce byla zaměřena na ověření platnosti koncepce master křivky pro hodnocení heterogenních svarových spojů, resp. teplotně stárnutých svarů. Současně bylo cílem disertace vyvinout kvantitativní model pro predikci referenční teploty lokalizující tranzitní oblast na teplotní ose za použití dat získaných z tahové zkoušky, a to za použití metody umělých neuronových sítí.

Studie je současně zaměřena na heterogenní svarový spoj připravený tavným svařováním. Je zacílena na hodnocení lomového chování v tranzitní oblasti nejméně odolné části svaru, tj. tepelně ovlivněné zóny ferritické oceli v blízkosti zóny natavení s vysokolegovaným materiálem. Pro predikci referenční teploty master křivky je použita zmíněná metoda neuronových sítí, a to za použití dat z tahových zkoušek a měření tvrdosti. Predikovaná referenční teplota byla ověřována na základě výsledku experimentálních měření.

Vytvoření modelu za použití neuronových sítí vyžaduje dostatečné množství dat a není vždy snadno tuto podmínku splnit. V případě sledovaného problému to znamenalo použití dat z dostatečně věrohodných zdrojů (skupiny Křehký lom ÚFM AVČR) a se známou metalurgickou historií. Smysl práce je tak možno spatřovat ve vývoji modelu neuronové sítě, která bude dostatečně přesně predikovat referenční teplotu.

Celkově byla pro tyto účely použita data z 29 nízkolegovaných ocelí. Pro účely vývoje byly použity kromě hladkých zkušebních tyčí, rovněž tahové zkoušky s obvodovým vrubem testované při kritické teplotě křehkosti (mez makroplastických deformací) a při teplotě pokojové. Při tvorbě modelu byla postupně v různých kombinacích využita všechna data z uvedených zkoušek.

Studie ukázala, že referenční teplota charakterizující tranzitní chování lomové houževnatosti oceli s převažující feritickou strukturou je jedinečným parametrem predikovatelným na základě vybraných charakteristik tahových zkoušek.

Klíčová slova: Oceli, Lomová houževnatost, Tahová zkouška, Referenční teplota, Umělá neuronová síť, Master křivka.

Bibliographic citation

Al Khaddour, S. Fracture behavior of steels and their welds for power industry. Brno: Brno University of Technology, Faculty of Mechanical Engineering, 2017. PhD Thesis 131 pp. Supervisor Prof. Ing. Ivo Dlouhý, CSc.

Claim

I hereby confirm that I am the sole author of the written work here enclosed and that I have compiled it in my own words. The work was made under the supervision of Prof. Ing. Ivo Dlouhý, CSc.

Brno, 19.01.2017 …….

Ing. Samer Al Khaddour

TABLE OF CONTENTS

1 INTRODUCTION

Mechanical testing is important for evaluating the main properties of engineering materials during service and for developing new materials. Evaluating the characteristics of a material during the application of a load helps us to know if the material is strong enough and rigid enough to resist the loads that it will experience in service. In this sense, a specific role belongs to the evaluation of the material's response to an external load with the presence of opening cracks, defects and or sharp notches. A number of experimental techniques for the mechanical testing of engineering materials have been developed, such as fatigue testing, fracture toughness determination, hardness testing, impact and tensile testing. In the frame of these mechanical tests, a specific role belongs to fracture toughness determination. Fracture toughness, which is a very important property of any material in design applications, is described as a stress intensity factor quantifying a stress field required to force a pre-existing defect/flaw to propagate. The linear-elastic fracture toughness of a material is determined from the critical value of stress intensity factor K_{Ic} at which a crack in the material begins to grow, whereas elastic- plastic fracture toughness includes a determination of energy required for the crack propagation.

For transition behaviour characterisation of low-alloy steels in various structural applications master curve concept is rapidly becoming an essential part. It is based on the finding that most ferritic steels with yield strength up to 750 MPa are characterized by the same shape of the fracture toughness transition curve, including the scatter band. The transition behaviour characterizing the particular steel is then defined by the position of this transition curve on the temperature axis. A reference temperature T_0 has been introduced for the positioning the transition region. In order to determine the reference temperature and the position of the fracture toughness transition curve on the temperature axis, it is essential to carry out a minimum number of valid standard fracture toughness tests. It is often difficult to use these tests for the purposes of estimating embrittlement during exploitation due to a lack of material or due to need to characterise selected location of the component e.g. highly dissimilar materials like weld joints. For similar case the master curve concept brings one very unique advantage. Only one parameter, the reference temperature, is needed for full quantification of fracture toughness transition region. So the effort may be concentrated on how to obtain the reference temperature by procedure other than direct standard measurement.

This study focuses on the evaluation of the fracture behaviour of welds carried out by fusion welding. It aims to investigate the fracture behaviour in transition region of the structural steels and welds with ferritic basic microstructures by means of reference temperature. In order to obtain the reference temperature artificial neural network is used exploiting tensile test and hardness test data on the input side.

Creating a model using neural network method requires a sufficient amount of data and it is sometimes not possible to accomplish easily. Creating a truly general model requires a combination of data and metallurgical knowledge. So, the aim of this work is also to develop artificial neural network enabling to predict the reference temperature. The design of the model is described and to test its validity, prediction is compared with experimental values and expectations; in total 29 data sets from low alloy steels are applied for the analysis.

The study is organized as follows. In section 2, a background of fracture mechanics is presented, and the determination of fracture toughness parameters in terms of K_{IC}, K_{JC} with a description of corresponding fracture behaviour in ductile to brittle transition region. Master Curve concept is used in order to quantify the fracture toughness temperature dependence in the transition region. Miniaturized test specimens for fracture toughness determination have been also included in the theoretical part of the study. The aims of thesis are included in section 3. Section 4 is devoted to the selected experimental details, e.g. the material description of the experimental specimens and test methods applied. Finally selected results of experimental investigation are presented in section 5. After section 6 dealing with discussion of results conclusions are summarised in section 7.

2 THEORETICAL BACKGROUND

2.1 Fracture Mechanics Background

2.1.1 Linear Elastic Fracture Mechanics (LEFM)

Consider a plate subjected to a remote stress where the plate width is larger than the length of crack, see Fig. 1, the stress field at the crack tip in linear elastic material behavior is given by the following equation [1]:

$$\sigma_{ij} = \frac{K}{\sqrt{2\pi r}} f_{ij}(\theta) + T\delta_{1i}\delta_{1j} + C_{ij2}(\theta) r^{1/2} + \cdots + C_{ijn}(\theta) r^{\frac{n-1}{2}} + \cdots \quad (1)$$

r, θ	Polar coordinate system
σ_{ij}	Stress tensor component
$f_{ij}(\theta)$	Dimensionless angular function
K	Stress intensity factor
T	Constant stress in the x-direction

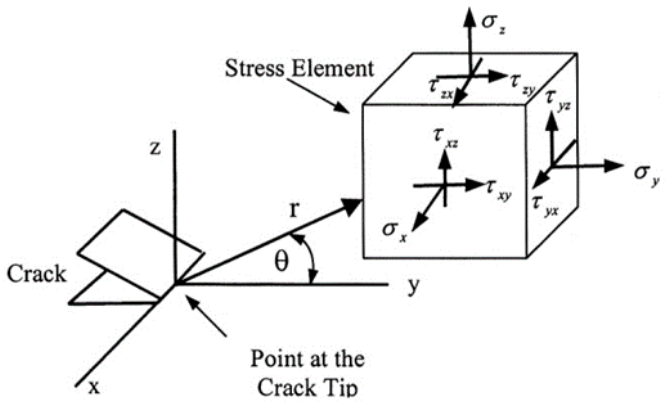

Fig. 1 Definition of the coordinate axes ahead of a crack tip [2].

Dimensionless functions $f_{ij}(\theta)$ and $g_{ij}(\theta)$ depend on the mode of loading, $g_{ij}(\theta)$ which depend on the geometry of the cracked body [3, 4]. The separate components of the stress tensor/stress field could be then quantified using the stress intensity factor in the following way:

$$\sigma_{xx} = \frac{K_I}{\sqrt{2\pi r}} cos\left(\frac{\theta}{2}\right)\left[1 - sin\left(\frac{\theta}{2}\right) sin\left(\frac{3\theta}{2}\right)\right], \quad (2)$$

$$\sigma_{yy} = \frac{K_I}{\sqrt{2\pi r}} cos\left(\frac{\theta}{2}\right)\left[1 + sin\left(\frac{\theta}{2}\right) sin\left(\frac{3\theta}{2}\right)\right], \quad (3)$$

$$\sigma_{zz} = \frac{K_I}{\sqrt{2\pi r}} cos\left(\frac{\theta}{2}\right) sin\left(\frac{\theta}{2}\right) sin\left(\frac{3\theta}{2}\right). \quad (4)$$

In the crack plane for $\theta = 0$ the shear stress is zero, the normal stress for Mode I loading in a linear elastic material is given by:

$$\sigma_{xx} = \sigma_{yy} = \frac{K_I}{\sqrt{2\pi r}}. \quad (5)$$

Eq. 5 is only valid near the crack tip, where the 1/√r singularity dominates the stress field. Stresses far from the crack tip are governed by the remote boundary conditions [5].

Irwin introduced three different loading modes classification. In the first mode of loading, also known as the opening mode, the load is normal to the crack plane [6].

Fig. 2 describes a schematic model of the plastic zone and the stresses ahead of the crack tip. The elastic stress distribution indicates that $\sigma_y \to \infty$ as $r \to 0$. Actually, σ_y is limited to σ_{ys} as shown by the elastic-plastic stress distribution. This means that $\sigma_y \to \infty$ occurs mathematically, not physically.

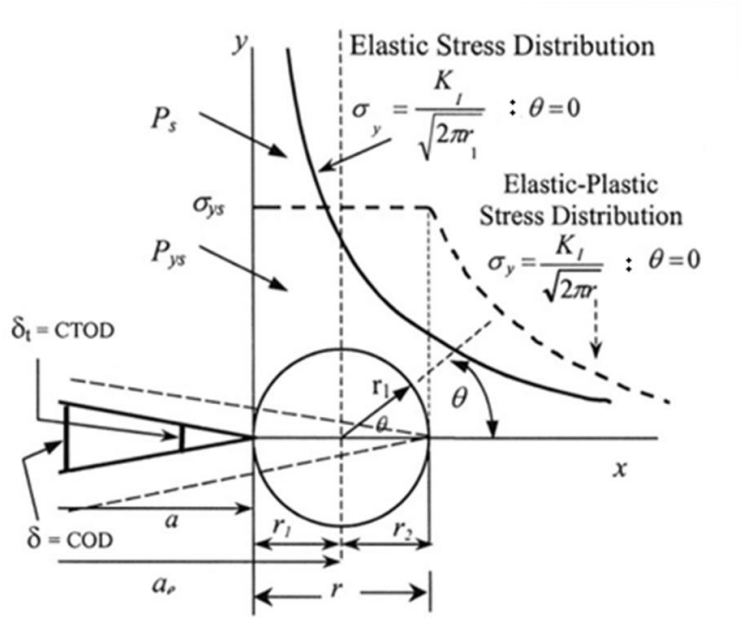

Fig. 2 Crack tip plastic zone model [2].

It is recognized that plastic deformation will occur at the crack tip as a result of the high stresses that are generated by the sharp stress concentration. To estimate the extent of this plastic deformation, Irwin [7] equated the yield strength to the y-direction stress along the x-axis and solved for the radius. The radius value determined was the distance along the

x-axis where the stress perpendicular to the crack direction would equal the yield strength; thus, he found that the extent of plastic deformation, i.e. radius of the plastic zone $r_y$was:

$$r_y = \frac{1}{2\pi}\left(\frac{K_I}{\sigma_{YS}}\right)^2. \quad (6)$$

2.1.2 Elastic Plastic Fracture Mechanics

LEFM applies when the nonlinear deformation of the material is confined to a small region near the crack tip [2]. Thus an important restriction to the use of LEFM is that the plastic zone size at the crack tip must be small. There are two elastic-plastic parameters introduced quantifying describing the crack tip stress field in elastic-plastic materials, the first parameter is the crack tip opening displacement *CTOD* and the second one is the *J* contour integral [8].

Wells [9] performed an approximate analysis that is related to *CTOD,* which is the displacement at the original crack tip. He observed that blunting of initially sharp cracks occur prior to fracture. The degree of crack tip blunting increases in proportion to the toughness of the material. Thus he proposed the crack tip opening displacement (*CTOD)* as a measure of fracture toughness [10].

Irwin [7] showed that crack tip plasticity makes the crack behave as if it were slightly longer. Alternatively, *CTOD* can be related to energy release, and it is given as following [4]:

$$\delta = \frac{K_I^2}{m\sigma_{YS}\,E} = \frac{G}{m\sigma_{YS}}, \quad (7)$$

where δ is *CTOD*, *m* is a dimensionless constant, which is approximately 1.0 for plane stress and 2.0 for plane strain.

The *J*-integral concept has been introduced by R. Rice for two dimensional domains containing cracks. For an arbitrary counter clockwise path Γ around the crack tip as shown in the Fig. 3 the strain energy density is given as [4, 11], where σ_{ij} and ε_{ij} are the stress and strain tensor components.

$$w = \int_0^{\varepsilon_{ij}} \sigma_{ij}\, d\varepsilon_{ij}, \quad (8)$$

Following, *J*-integral can be given by definition as:

$$J = \int_\Gamma \left(w dy - T_i \frac{\partial u_i}{\partial x} ds\right), \quad (9)$$

where $T_i = \sigma_{ij} n_j$ is traction vector, u_i displacement vector.

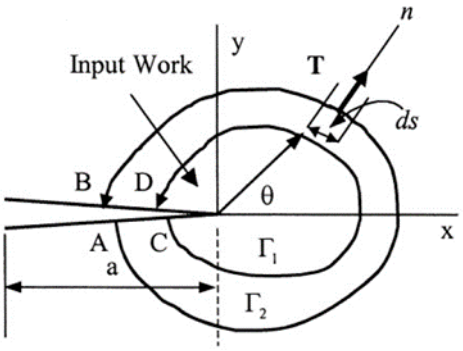

Fig. 3 Crack tip coordinate system and typical line integral contour [2].

Rice [11] proved that in case of nonlinear elastic material the *J*-integral does not depend on the path of integration around the crack tip. The single parameters K, J or $CTOD$ are valid under small scale yielding conditions, where these parameters can describe the crack tip conditions, but single parameter approach becomes invalid in the case of excessive plasticity, where the size and geometry of the test specimens affected the fracture. Rice [11] proved that for the special case of a linear elastic material, the stress energy release rate G is equal to the value of the *J*-integral, and therefore, the stress intensity factor can be evaluated by the following equations [12-14]:

$$K_J = \sqrt{J.E^*} = \sqrt{\frac{J.E}{1-v^2}}, \tag{10}$$

where $E^* = \frac{E}{1-v^2}$ for plane strain and $E^* = E$ for plane stress.

2.1.3 Experimental Determination of the Fracture Toughness

All brittle materials contain a population of small cracks and flaws that have different sizes, geometries and orientations [4]. When the value of tensile stress at the crack tip exceeds the value of critical stress, a crack forms and then propagates, causing a fracture. The crack tip stress intensity factor describing the stress field depends on load and crack vs specimen geometry/configuration, its critical value, i.e. fracture toughness then depends on the material, temperature, environment and rate of loading [15].

For determining fracture toughness, standard testing conditions and test specimens geometry and dimensions have to be used. The compact test (CT) specimens and the single-edge notched bend specimens (SENB) that are usually used to characterize fracture initiation and crack growth are permitted in ISO 12135 and similar standards [16]. The stress intensity factor corresponding to the (CT) specimens is obtained from the following expression:

$$K_Q = \left[\frac{F_Q}{B.W^{1/2}}\right].g\left(\frac{a_0}{W}\right), \tag{11}$$

where the crack length should be about $\frac{a_0}{W} \approx 0.5$, $g\left(\frac{a_0}{W}\right)$ is a geometrical function of dimensionless crack length of $\frac{a_0}{W}$, B and W are the thickness and the width of specimens respectively, are a_0 is the initial crack length. The function and $g\left(\frac{a_0}{W}\right)$ is given by the following expression:

$$g\left(\frac{a_0}{W}\right) = \frac{\left(2+\frac{a_0}{W}\right)\left[0.886 + 4.64\frac{a_0}{W} - 13.32\left(\frac{a_0}{W}\right)^2 + 14.72\left(\frac{a_0}{W}\right)^3 - 5.6\left(\frac{a_0}{W}\right)^4\right]}{\left(1-\frac{a_0}{W}\right)^{1.5}}. \tag{12}$$

The force F_Q is a critical force of load determined by corresponding way [16] force load-load displacement force.

In order to validate K_Q as K_{IC} values the following requirements according the standard ASTM E399 [15] must be fulfilled:

$$B, a, (W-a) \geq 2.5\left(\frac{K_Q}{\sigma_{YS}}\right)^2, \tag{13}$$

$$0.45 \leq \frac{a}{W} \leq 0.55, \tag{14}$$

$$F_{max} \leq 1.10F_Q, \tag{15}$$

where σ_{YS} represents the yield stress at the test temperature applied. That means, the value of K_{IC} is not valid if the plastic zone at the crack tip is too large. The plastic zone has to be very small when compared to zone of elastic singularity and relevant dimensions (thickness) of specimens Thus, K_{IC} is a function of applied force and test specimen size, geometry, and crack size. The validity of the K_{IC} value determined by this test method depends upon the establishment of a sharp-crack condition at the tip of the fatigue crack in a specimen having a size adequate to ensure predominantly linear-elastic, plane-strain conditions. Once the conditions (13) and (15) have not been met, the fracture toughness must be determined according to EPFM concept.

Practically, the *J*-integral calculation consists of an elastic and plastic component determination. This is given by the following equation:

$$J_Q = J_e + J_P. \tag{16}$$

The elastic component J_e is calculated using the value of linear elastic stress intensity factor K_e as calculated from fracture load according to the expression:

$$J_e = \frac{K_e^2(1-v^2)}{E}. \tag{17}$$

In general, the plastic component J_P is calculated as follows

$$J_P = \frac{\eta U_p}{(B_N . b_0)}, \tag{18}$$

where U_p is the plastic part of the area under curve of force versus load line displacement, B_N is the specimen net thickness, b_0 is the uncracked ligament. Here $\eta_p = 2 + 0.522\, b_0/w$ for a compact specimen; η_p is a dimensionless constant which depends only on the crack length and geometry of the specimen [17].

The values of *J*-integral are usually converted to their equivalent values in terms of stress intensity factor K_{Jc} from the following expression:

$$K_{Jc} = \sqrt{\frac{J_C E}{(1-v^2)}} = \sqrt{J_c E'}. \tag{19}$$

2.2 Brittle Fracture of Low Alloyed Steels

Two types of brittle fracture can be can be distinguished by the fracture path. In transgranular fracture, the fracture travels along specific crystallographic planes [18]. That means the fracture prefers the path of least resistance against deformation. Intergranular fracture is the crack traveling along the grain boundaries, and not through the actual grains [19]. In this case, the grain boundaries are the preferred fracture path, e.g. taking place when the phase at the grain boundary is weak and brittle.

Cleavage fracture occurs by direct separation along specific crystallographic planes by means of a simple rupturing of atomic bonds. Alfa iron, basic lattice of ferritic steels, undergoes cleavage along its cubic planes (100). This gives the characteristic flat surface appearance within a grain on the fracture surface. As in polycrystalline material, the adjacent grains have different orientation (Fig. 4), the cleavage crack changes direction at the grain boundary in order to continue along the given crystallographic planes.

Since the cleavage fracture involves braking of atomic bonds, sufficient stress is needed to overcome the cohesive strength of the material. This cohesive strength is related to microscopic cleavage fracture stress. Once the local stress component of the applied stress is higher than the cleavage fracture stress the cleavage fracture nucleation can occur. The

cleavage fracture stress is a material property which is generally defined based on tensile test of smooth specimen as the lowest fracture stress value on its temperature dependence.

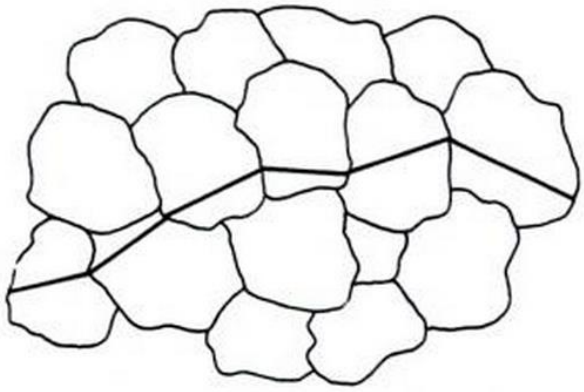

Fig. 4 Cleavage spreading through grains [4].

There are different models describing this event on a microstructure level. Thus, from micromechanical view point, two conditions for cleavage fracture at the crack tip are needed: certain level of the effective strain and a load stress higher than the cleavage (critical) fracture stress σ_{CF} over some microstructurally important distance.

Stroh [20] suggested that the dislocation pile-up causes the condition of the shear stress to nucleate a microcrack. He also suggested inclusion of the effect of the grain size in his model. Cottrell [21] proposed that the fracture process should be controlled by the critical crack growth stage through applying tensile stress, which needed higher stress than the crack nucleation. Zener and Stroh [20] suggested that the crack nucleation of cleavage fracture occurs when the shear stress created by pile-up of n dislocations of Burgers vector at a grain boundary reaches a critical value. Carbides and/or other hard particles could cause the cleavage fracture, if a macroscopic crack provides sufficient stress concentration to overcome the atomic bonds, the micro crack propagate into the ferrite matrix. The fracture stress for a penny-shaped crack produced by a spherical particle is given by the following expression [8]:

$$\sigma_F = \left(\frac{\pi E \gamma_P}{(1-\nu^2)C_0}\right)^{1/2}, \tag{20}$$

where γ_P represents the plastic work which is required to create a unit area of fracture surface in the ferrite, and C_0 represents the particle diameter. Suitable models for ferritic steel have been studied in order to understand the relationship between the cleavage fracture stress and microstructure. In tempered alloy steels for example, the spherical carbide usually

play the critical role, and in mild steels, cleavage fracture usually initiates at grain boundary carbides. These models are given at the end of the section [3].

These above described concepts were accepted also in Ritchie Knott and Rice model [22] often used for quantification of initiation condition for cleavage brittle fracture, see Fig. 5. Firstly, they postulated that the critical distance in which the cleavage nucleation condition must be fulfilled is equal to two grain diameters for mild steel material. Later, they found there is not a consistent relationship between the critical distance and the grain size. Curry and Knott found that the critical sample volume of material must be higher for those having local stress higher than σ_{CF} [22]. The relationship between the critical volume of material and critical distance may depend on the average spacing of cleavage nucleation sites [4]. This model also enables us to explain why cleavage fracture toughness data tends to be widely scattered. The statistical models of Curry and Knott were treated as a weakest link phenomenon. The probability of fracture is equal to the probability observing at least one critical fracture-triggering particle [23]. The probability of fracture can be obtained by the following equation:

$$F = 1 - exp\left(-\left[\frac{K_{Ic}}{\theta_K}\right]^4\right), \tag{21}a$$

$$F = 1 - exp\left(-\left[\frac{J_c}{\theta_J}\right]^2\right), \tag{21}b$$

where the crack tip conditions are defined by $K\ or\ J$, and θ_K or θ_J are material properties that depend on microstructure and temperature.

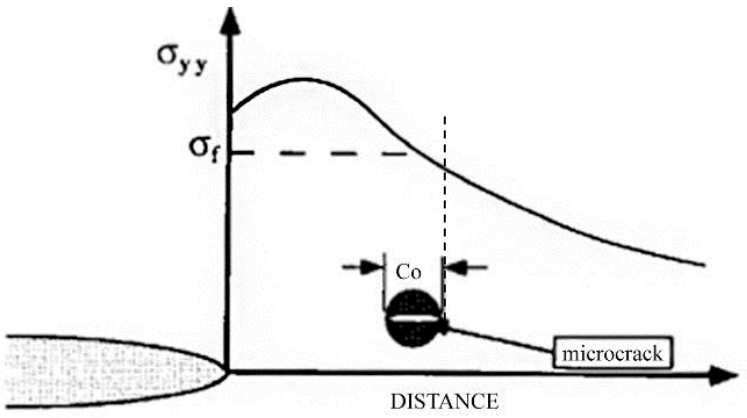

Fig. 5 Initiation of cleavage fracture at a microcrack that forms in a second phase particle ahead of a macroscopic crack [4].

Cleavage fracture is always preceded by local plastic deformation. The first necessary condition for cleavage fracture is plastic deformation, but it is not a sufficient condition. According to RKR, the local stress value must be higher than the critical σ_{CF} value. If the stress ahead of the macroscopic crack is sufficient, the microcrack propagates into the ferrite matrix [24].

$$\sigma_{CF} = R_e = \frac{2Gv.\gamma_m}{k_y} d^{-1/2}. \tag{22}$$

Note that in real ferritic steels, and in their weld joints in particular, different cleavage fracture nucleation micromechanisms and fracture initiation can take place. Observed micromechanism thus may change from the weakest link behaviour to accumulation of damage sites, both showing typical fracture patterns on fracture surfaces (Fig. 6).

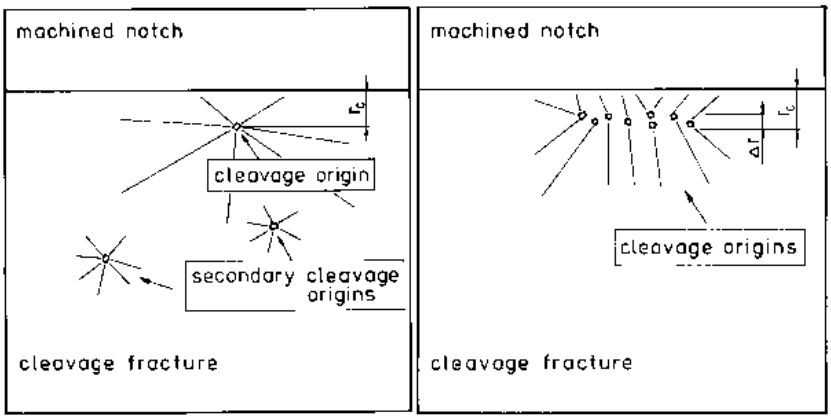

Fig. 6 Typical fracture patterns on fracture surfaces for weakest link behaviour (left) and accumulation of damage sites concept (right) [24].

The particular micromechanical behaviour of the given steel is then affected by different effects. Both the external factors (loading rate, temperature, structural defects and notches as stress concentrators) and the internal factors (chemical composition, microstructure including grain size, and impurity effects, operational degradation effects onto microstructure, including e.g. the carbide coarsening or impurity diffusion to grain boundaries or selected cleavage planes) affect the cleavage fracture and also affect the brittle to ductile transition.

In contrast, there are cases of unsuccessful cleavage fracture events. Unsuccessful event means that cleavage crack nucleation does not cause brittle fracture initiation. The first case occurs when a microcrack ahead of the macroscopic crack has been arrested at the particle/matrix interface, as shown in Fig. 7a). The second case happens when a microcrack is arrested at the grain boundary as shown in Fig. 7b), where the crack is unable to propagate

because the applied stress is insufficient. Fig. 7c) shows that the crack is unable to propagate, if there is a steep stress gradient ahead of the macroscopic crack [4].

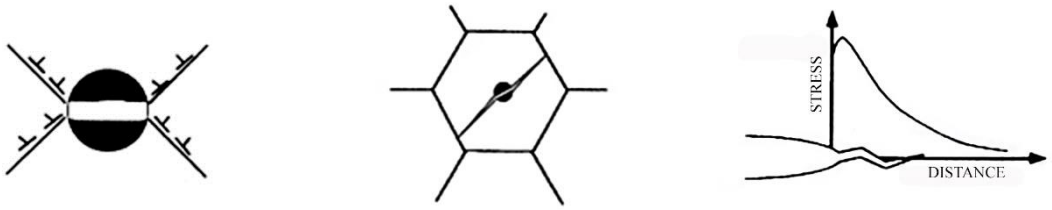

a. arrested at the particle/matrix interface

b. arrested at grain boundary

c. arrested due to a steep stress gradient

Fig. 7 Examples of unsuccessful cleavage fracture event [4].

2.3 The Ductile-Brittle Transition

The fracture toughness of ferritic steels hardly differs over a small temperature interval, see Fig. 8. At low temperatures, steel is brittle and cleavage fracture usually occurs. At high temperatures, steel is ductile and fracture occurs by microvoid coalescence. The temperature dependence of fracture toughness is divided to three main regions [25]. In the lower shelf region the steel is brittle and the fracture mechanism is almost cleavage [26].

In the transition region between ductile and brittle behavior, both micro-mechanisms of fracture, i.e. ductile microvoid coalescence and brittle cleavage fracture take place and can be present at the same fracture surface [24]. In the upper shelf transition region, the crack initiates and propagates by microvoid coalescence, but ultimately failure may occur by cleavage see Fig. 8.

According to the mechanisms preceding the fracture initiation, the following fracture toughness parameters may be used for quantification of the critical conditions. K_{Ic} represents plane-strain fracture toughness according to linear elastic concept, K_{Jc} represents elastic-plastic fracture toughness converted from critical J_c–integral value set for the moment of unstable fracture initiation, K_{Ju} represents fracture toughness converted from the critical J_u–integral value set for the moment of unstable brittle fracture initiation after a certain ductile crack propagation Δa at the root of the original crack prior to fracture cleavage, K_{Jm} represents informative values of fracture toughness at the moment of ductile fracture initiation at the crack tip, converted from critical J_m–integral value [27].

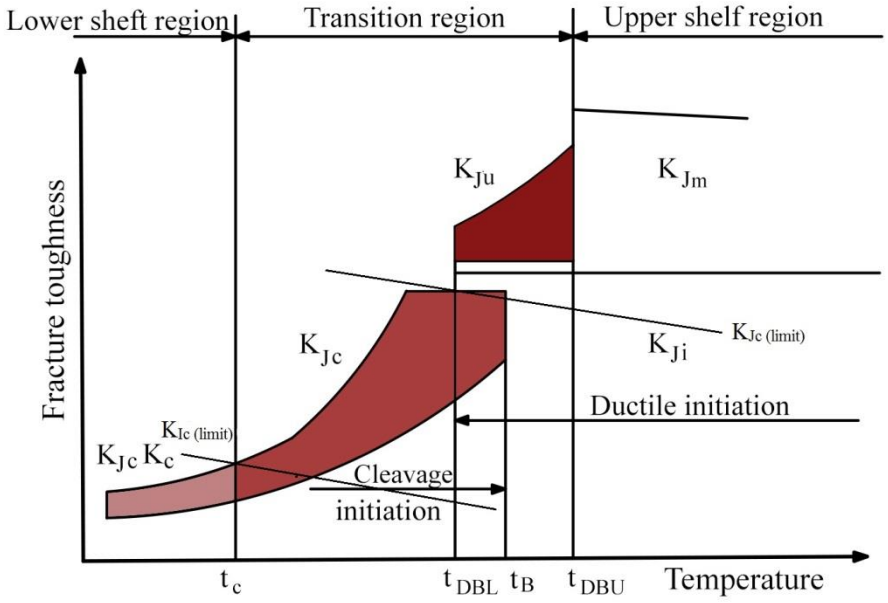

Fig. 8 Temperature dependence of fracture toughness [24].

2.3.1 Master Curve

The fracture toughness is a property which describes the resistance of a material containing a crack to fracture initiation, and is one of the most important properties of any material for structural applications [28-30]. As described in previous chapter steels with ferritic microstructure are possessing transition behaviour. Then a master curve is a statistical model based on the engineering analysis of data and following the quantification of the dependence, where the fracture toughness at a particular temperature in the transition region depends on three parameters Weibull distribution. It is shown by the following equation [31]:

$$P_f = 1 - exp\left[-\left(\frac{K_{Ic} - K_{min}}{K_0 - K_{min}}\right)^4\right], \tag{23}$$

where P_f represents a probability of brittle fracture for the arbitrarily selected specimen, where K_0 is the size-scale parameter, and K_{min} is the minimum fracture toughness, which is assumed to be equal to 20 MPa$\sqrt{\text{m}}$.

For the median value of fracture toughness equalling to 100 MPa$\sqrt{\text{m}}$, the reference temperature T_0 is defined. The relationship between the median fracture toughness and temperature in the ductile-brittle transition temperature region of ferritic steels is given by the fracture toughness master curve [32, 33] in accordance with the following equation:

$$K_{J_{C(med)}} = 30 + 70\ exp[0.019(T - T_0)]. \tag{24}$$

There are two methods to estimate the master curve reference temperature T_0. The first one is called the single temperature method where T_0 is calculated from size adjusted K_0 values by using Eq. 24. And the second one is called the multi-temperature method. This is given in the following equation [33-35].

$$\sum_{i=1}^{N} \delta_i \frac{exp[0.019(T-T_0)]}{11+77\,exp[0.019(T-T_0)]} = \sum_{i=1}^{N} \frac{\left(K_{Jc(i)}-20\right)^4 exp[0.019(T-T_0)]}{[11+77\,exp[0.019(T-T_0)]]^5} \,. \tag{25}$$

At least six valid values of $K_{Jc(i)}$ must be available to establish the T_0 temperature, where the temperature is units of ℃, and K_{Jc} in units of $\mathrm{MPa}\sqrt{\mathrm{m}}$. The ASTM standard E1921[36] includes the determination of a reference temperature T_0 for ferritic steels in the transition region, where the yield strengths are ranging from 275 to 825 MPa. The temperature dependence of fracture toughness is given to conform to a standard shape known as the master curve. The temperature T_0 is obtained from the median (50% fracture probability) corresponding to 100 $\mathrm{MPa}\sqrt{\mathrm{m}}$ of the K_{Jc} distribution from 1T size specimens.

2.3.2 Local Brittle Zones Concept

There are many factors affecting the fracture behavior of the weld joints, for example, weld groove geometry, crack length to width ratio a/W, crack location, thickness of the weld joint, the loading rate, and so on. One of the main factors visible when looking at the fracture behavior of welded joints containing cracks is the heterogeneity of the joint. The weld width influences the fracture toughness of the weld joint, because of the plastic zone which is developed in front of the crack tip. In addition, the geometry of the specimen significantly affects the crack resistance curve. The fracture behavior of weld joint is determined by using the lowest yield strength value, when the structure is subjected to the nominal stress.

Determining the fracture toughness of welded joint by using a small number of specimens and obtaining a suitable statistical distribution function is a problematic issue. Consequently, estimating the fracture toughness value from this statistical distribution is an incorrect thing to do. This problem can be solved by evaluating the probability of fracture according to the Weibull model, based on the weakest link theory. The following relation gives the distribution for a ferritic steel as described in [24]:

$$P\left(K_{Jc}\right) = 1 - exp\left(-\left[\frac{K_c-20}{K_0-20}\right]^4\right), \tag{26}$$

where $P\left(K_{Jc}\right)$ represents the cumulative probability of fracture toughness, K_0 is the scale parameter (the 63^{rd} percentile of the distribution), 20 is the shift parameter in the Weibull

distribution, 4 is the value of the shape parameter in the Weibull distribution for the small scale yielding.

In order to provide an estimate of K_c with a given probability, if the K_0 value is known the last equation can be re-written as follows:

$$K_c = 20 + (K_0 - 20)\left\{-ln\left(1 - P(K_{Jc})\right)\right\}^{0.25}. \quad (27)$$

The fitting distribution procedure is based on the determination of an optimum value of K for a particular set of data. Unfortunately, the results of the test may be diverted when specimens are taken from non-homogeneous materials, such as weld metals and heat affected zones (HAZs) containing local brittle zones (LBZ). The fracture toughness distribution will be diverted to the higher toughness regions, because it is not probable that every specimen in a series of tests will contain local brittle zones (LBZ). In order to overcome this problem, Wallin [37] proposed a maximum likelihood estimation procedure (MML). The Weibull distribution in the SINTAP is used to provide conservative and realistic evaluations of the defects in a component [24, 37].

The MML procedure includes a series of stages. The first stage in the procedure is to check whether all of the data meets the validity criteria of the relevant testing standard. The limit of valid value of fracture toughness $K_{Jc(limit)}$ is determined by the following equation [38]:

$$K_{Jc(limit)} = \left(E' b_0 R_y/30\right)^{0.5}, \quad (28)$$

where b_0 represents the initial ligament below the notch $(W - a_0)$ in the test specimen, R_y is the yield strength of a selected zone of the welded joint, and K_0 is obtained by the following equation [24]:

$$K_0 = 20 + \left[\frac{\sum_{i=1}^{N}(K_{ci} - 20)^4}{\sum_{i=1}^{N}\delta_i}\right], \quad (29)$$

N is the number of results in the data set, and i is the i^{th} result.

The MML procedure involves censoring all data with value greater than the 50th percentile. Censored data is assigned the median value of toughness as follows [37]:

$$\bar{K} = 20 + \left(K_0^{(1)} - 20\right) * 0.91. \quad (30)$$

The final step requires an estimation of K_0 by using the minimum fracture toughness value which is measured in the data set. This is given by:

$$K_{0min} = 20 + (K_{25min} - 20)\left(\frac{n}{ln2}\right)^{0.25}. \quad (31)$$

The MML procedure can be applied to data in the fracture toughness transition regime. The advantage of this method is that the estimation of the scale parameter is confidence, especially when there are a limited number of tests, for instance, in inhomogeneous materials such as welded joint [24, 37].

2.4 Possibilities for Simplification of Fracture Toughness Estimation

These approaches are most needed when the sample size needs to be minimized, and materials under development are available only in a limited amount. A typical example: welded joints are mostly measured by using more simple techniques, such as the uniaxial tensile test, impact testes of Charpy type specimens and the ball indentation test or the small punch test [39].

2.4.1 The Small Punch Test

The Small Punch Test (SPT) is currently used and under further developments to estimate the mechanical properties and fracture characteristics in the transition region of ferritic steels. The specimen for SPT has commonly a disc shape with dimensions about 8 mm (Fig. 9). The specimen is punched by using a ball until the disc is broken. During this process, the force-displacement curve is recorded [40-42]. The typical test record is shown in Fig. 9.

This technique has been developed to characterize the ductile-brittle transition behavior of ferritic steels and obtain information about the toughness value of the materials such as K_{Ic} and J_{Ic} by using critical strain energy density in the small punch specimen as a fracture criterion [43]. However, there is disadvantage: there is biaxial stress state in the specimen during the test, which causes complications in the determination of the correct material properties [44, 45]. It is thus necessary firstly to correlate the results of SPT with data from the standards test procedures and develop databases of mechanical properties which are determined by SPT and/or to develop correlation equation for the particular steel. Because of the biaxial stress in the specimen during loading, an interpretation of the results of the test against the results of the standard fracture specimen is thus not straightforward [40, 46].

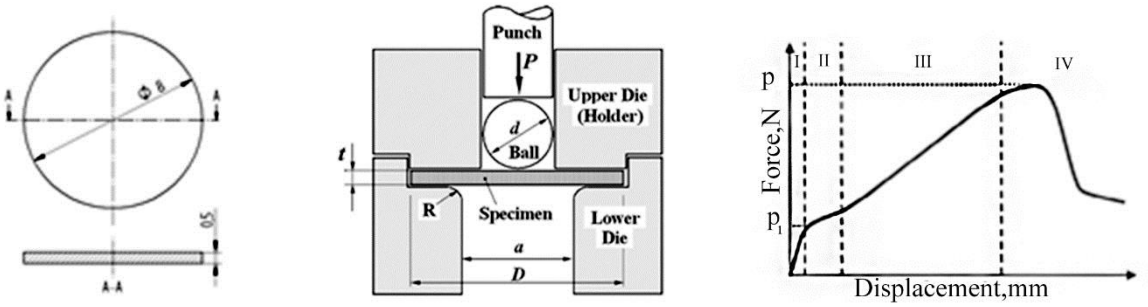

SP specimen | Small punch testing fixture | A typical small punch force-displacement curve

Fig. 9 Schematic setup of small punch test [47].

We can obtain the mechanical properties, such as fracture strain, transition temperature, and the crack initiation point by analysing load-displacement curves in SP tests. The stress-intensity factor and its critical value can be obtained through the analysis of the stress fields at the crack tip for sharp-notched SP specimens [48]. In order to identify the initiation, a supporting technique is needed, e.g. a micro-camera, located at the bottom tensile side of the fixture.

2.4.2 Tensile Test

Uniaxial tensile test is known as a basic and universal engineering test which enables obtaining the material properties such as the ultimate tensile strength, yield strength, maximum elongation and reduction in area, and Young's modulus. These important parameters can be achieved from the tensile test sample and load curve and are not only useful for the selection of engineering materials for any required applications, but also for the interpretation of the fracture behavior [49, 50].

An engineering stress-strain curve can be constructed from load-elongation curve. A typical engineering stress-strain diagram and main parameters are shown in the Fig. 10. In order to estimate the fracture toughness from tensile test data, it is possible to use the critical fracture strain model for ductile fracture prediction given by [51]:

$$K_{Jic} = Constant\left(\in_u \cdot\, l_0^* \cdot E \cdot \sigma_y\right)^{0.5}, \tag{32}$$

K_{Jic} represents the fracture toughness calculated from J_{ic}, $\in_u$ is the uniform strain, value of strain corresponding to maximum load, l_0^* is the characteristic distance ahead of the crack tip, E is the elastic modulus, σ_y is the yield strength. The critical characteristic distance, l_0^* is

a multiple of the planar inclusion spacing (spacing between major voids on a fracture surface) and is obtained empirically.

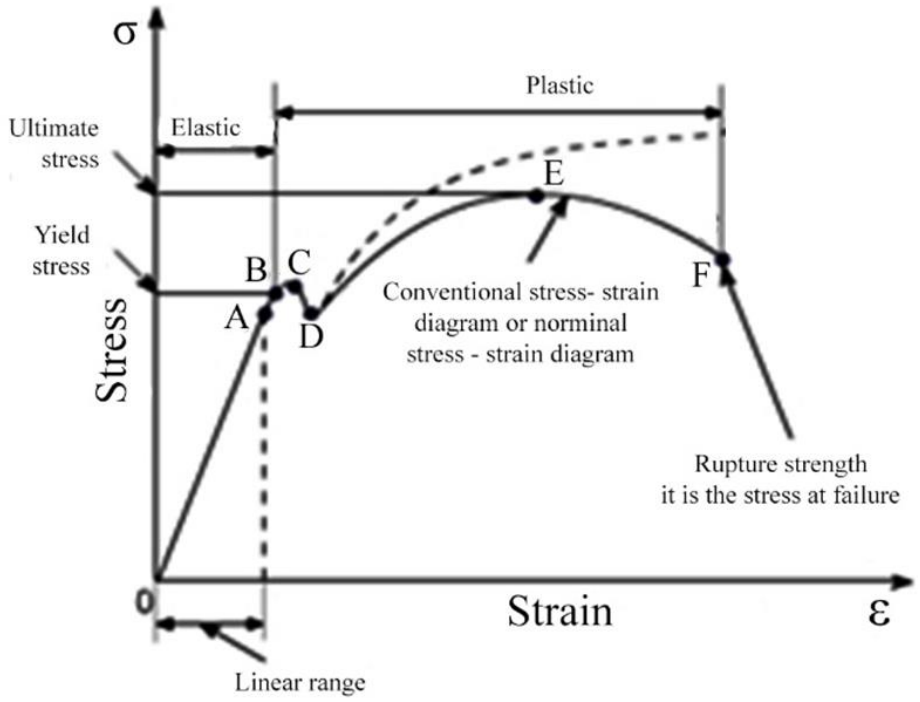

Fig. 10 Schematic engineering and true stress-true strain diagram for tensile test [51].

It is also generally known that true strain corresponding to fracture is necking area of the tensile test. Sample can be taken as characteristics relevant to fracture toughness. For this particular case it was calculated directly from reduction in area at fracture. Direct correlation has not been found however thus it can be used only after obtaining correlation equation for the particular steel.

2.4.3 Instrumented Indentation Test

In order to estimate the mechanical properties of a material, the instrumented indentation test is often taken as a semi non-destructive test. The advantage of this method is that it is simple and fast in its application. This technique uses a very small volume of the material [52]. For estimating the mechanical properties, multiple indentation with a spherical indent or called in this case as ball indentation test, or with Vickers indenter are used in the selected test location on metal surface. Fig. 11 shows the indentation test profile, the indentation depth trace and diameter, and a typical load indentation depth. The relationship between the load and depth is linear. During the multiple indentations, several loading and

unloading cycles are done at the same location on the work piece surface [53] as shows in Fig. 11.

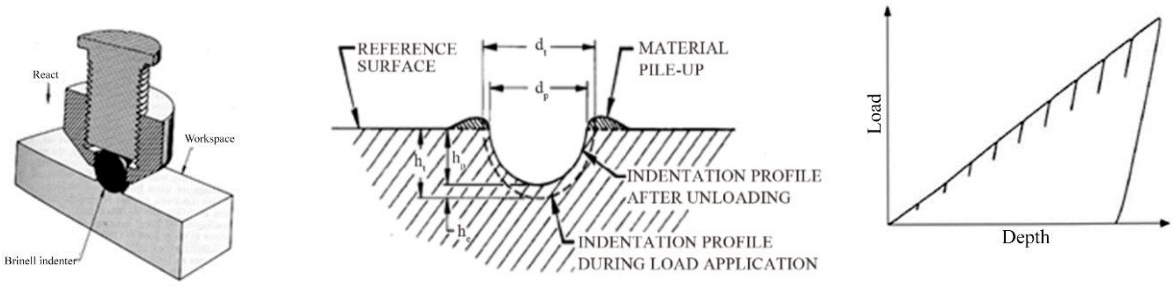

Fig. 11 Schematic setup of Ball Indentation Testing [53].

When the maximum stress underneath the ball indenter equals the critical fracture stress (at a critical indentation depth), the deformation energy represents the temperature dependent part of the fracture toughness of the test material [53]. There are two methods that can be used to estimate the mechanical properties: either by empirical equations or by using the finite elements calculation method. In the first case, the analysis are based on Meyer's equation correlating data from unloading part of the indentation loading and geometry of the indent with empirically determined yield strength and Young's modulus. In the second case indentation curve is computed by means of finite element model into which tensile curve is parametrically implemented. Then based on iterations in accordance between computed and experimentally measured indentation curve is find out and parameters of tensile curve is evaluated.

For brittle materials a method based on the Vickers indentation, can be also used to assess the fracture toughness directly from indent cracks. Lawn modelled the elastic-plastic behavior under indent [54]. Supposing the median/radial crack system is created due to tensile stresses created during unloading, the following expression can be used to assess the fracture toughness by implementing the Vickers indentation [55]:

$$K_C = \alpha \sqrt{\frac{E}{H}\frac{F}{C^{\frac{3}{2}}}}, \tag{33}$$

where F stands for the applied force, H is the hardness, C is the length of the surface trace of the half penny crack which is measured from the centre of the indent, E is Young's modulus.

2.5 Miniaturized Test Specimens for Fracture Toughness Determination

The miniaturized specimens offer a possibility to evaluate the fracture behavior by using a limited amount of test material. The motivation for their applicability can be found in processes of material development, monitoring of degradation of mechanical properties and in characterization of local mechanical properties, e.g. in weld joint. These specimens usually do not meet the size requirements of a valid determination of fracture characteristics. Small loaded volumes at the crack tip under the fracture initiation conditions in these specimens are usually not sufficient to maintain the SSY conditions and the loss of crack tip constraint then occurs [56]. That results in size and geometry dependence of measured fracture characteristics. The stress-strain fields at the crack tip in the miniaturized specimens which is different from small scale yielding (SSY) conditions can even result in the change of fracture micro-mechanisms. Comparison of data sets of standard and miniaturized test specimens results in lower transition temperature, steeper transition curve and larger scatter for miniaturized specimens. The main reason for this reduced correlation is seen in the loss of the crack tip constraint, both in-plane and out-of-plane. The important issue is therefore the interpretation and transferability of fracture characteristics measured on miniaturized specimens [24, 57].

There are several types of miniaturized specimens. In this chapter, miniaturized specimens with geometries parametrically developed from the geometries of standard test specimens (KLST, MCT and DCT specimen) are briefly introduced. Their performance in comparison to standard test specimens is also described.

2.5.1 KLST Specimen

The KLST specimen, from the German Kleinstprobe, or "small specimen", is a rectangular bar for three-point-bend loading. It was introduced in DIN standard [58]. Its dimensions are 3×4×27 mm^3 (thickness×width×length), enabling to manufacture the KLST specimen from the half of Charpy type specimen. Modifications of KLST specimen with V or U notch are used for impact tests [56, 57], whereas pre-cracked modification is used to measure the fracture toughness data. See Fig. 12.

KLST Response in Transition Region

Wallin has carried out a validation study about the applicability of miniaturized bend specimens, among them also KLST specimen in order to determine the reference temperature T_0 according to the master curve concept to ASTM E1921 [36, 59]. This standard introduces “validity window” in order to determine valid test data, which are then

used to estimate T_0. The "validity window" is restricted by temperature range and validity limit for K_{Jc} fracture toughness $K_{Jclimit}$. Due to the low values of $K_{Jclimit}$ for miniaturized specimens, Wallin proposed a narrower "validity window" for these specimens in the range: $-50\,℃ \leq T - T_0 \leq -20\,℃$. That measure involves testing the miniaturized specimens at very low temperatures, where more specimens have to be tested to obtain the same probability contrary to the temperature around T_0. When fracture toughness data keeps all described conditions, no differences can be detectable in estimated values of T_0 between investigated bend geometries. Standard uncertainty of T_0 estimation is ±10 °C. Specimens without side-grooving show by about 40 °C higher estimation of T_0 compared to pre-cracked Charpy type specimens [60]. The difference of T_0 estimation is about -9 °C compared to standard specimens mentioned [61].

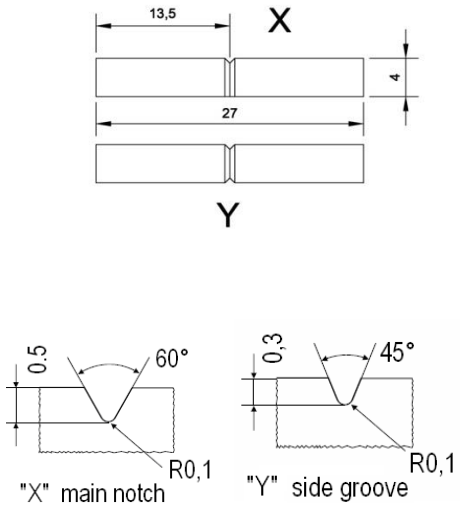

Fig. 12 The geometry of pre-cracked KLST specimen (top), main notch (left) and side groove (right) [62].

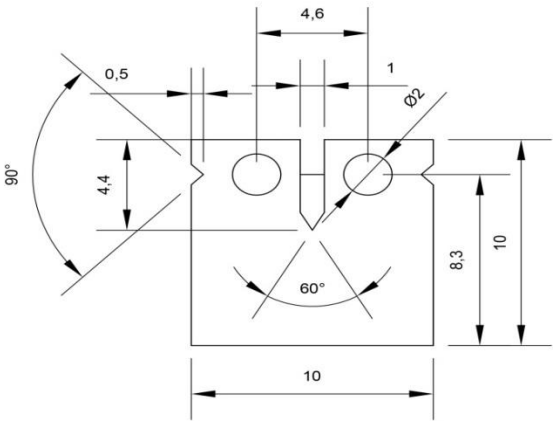

Fig. 13 The geometry and dimensions of MCT specimen used in [63].

Behavior in Upper Shelf Region

In fully ductile behavior, the KLST specimens show a very strong size effect [62]. For example, comparison of the results determined on Eurofer 97 steel indicate that KLST specimens have by about 30% and 60% lower values on J-R curve than 3×6×30 mm^3 and 9×18×92 mm^3 specimen, respectively [64].

2.5.2 Miniaturized Compact Tension Specimen

Miniaturized CT specimen (MCT) was designed to be manufactured from Charpy specimen cross-section 10×10 mm^2. With its thickness of 4.2 mm (0.16T), it is possible to machine out four MCT specimens from the half of Charpy specimen [63]. Due to its dimensions, grooves for clip-gauge are placed on its side, see Fig. 13.

Behavior in Transition Region

MCT specimen seems to be the most suitable test specimen, from the point of view of limited amount of tested material and constraint level at the crack tip, e.g. for application in hot-cells facilities [63]. It shows about 8.5°C lower systematic deviation of T_0 comparing to 1T-CT specimens apparently because of both in-plane and out-of-plane constraint loss.

For practical applications, there is still uncertainty in interpretation of data generated using these samples. Because of crack tip constraint effect, the difference between obtained reference temperature for the miniaturized compact CT and the standard specimen will change for different steels and, thus standardized procedure is not available.

Behavior in Upper Shelf Region

With fully ductile behavior of material, the J-R curves determined on MCT specimens were significantly lower when compared to 1T-CT [65, 66]. The observed difference in the initiation values of J-integral between the above mentioned specimens was approximately 300 kJ/m^2. This means the J_{IC} value is by about 50% lower for mini type of specimens comparing to standard one. This trend was verified in the case of six steels that are used in the application for pressure vessels and pipes [65]. However, tests performed on a material with low toughness (KV at USE = 70 J) had not revealed any observable difference in fracture characteristic between subsized out standard specimens [65]. Described behavior of specimens for different materials is apparently closely connected with the actual level of toughness of the material and with its ability to plastic deformation and to constraint loss respectively. The application of side-grooving is favourable for miniaturized specimens. Its introduction decreases the length of the crack-tip through thickness/dimension, but on the

other hand, it increases the level of stress triaxiality along specimen thickness. Thus, side-grooving helps to maintain out-of-plane constraint.

From the point of view of the applicability of the described miniature specimens, CT specimens are favourable, as they take into consideration the amount of tested materials and the level of crack tip constraint. However, bend geometry of KLST specimen is more suitable for dynamic loading.

2.5.3 Miniaturized Disc Shape Compact Tension Specimen

Another modification of miniaturized CT specimen is the disc shape specimen (DCT) which is developed in Oak Ridge National Laboratory (USA) in order to characterize the fracture behavior of irradiated materials [67]. The specimen was designed to take full advantage of the available space of the testing capsules in nuclear power reactors, which are dimensionally identical to fuel rods (Fig. 14). In literature, only limited information about the behavior of DCT specimens can be found. Most of them are related to individual tests of irradiated materials and their degradation states, usually with no corresponding results from larger type of cracked specimens [68, 69]. Due to the similarity between DCT and MCT specimens, both in dimensions and volume of the tested material, the same size effects on measured values of the fracture toughness can be expected.

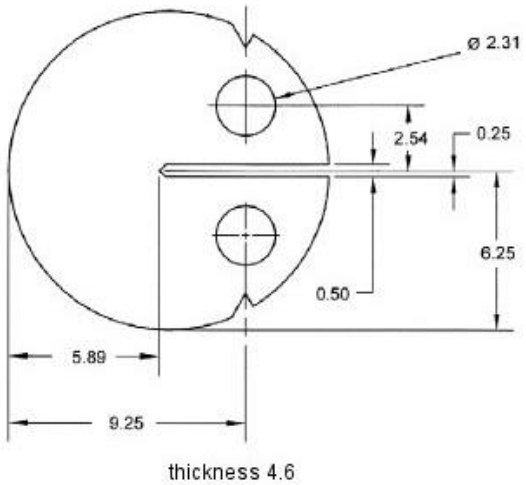

Fig. 14 Geometry and dimensions of DCT specimen (in mm) [68].

2.6 Neural Networks in Material Science

Artificial neural networks (ANNs) are an information processing model that is inspired by the biological nervous systems work, such as the brain, on a computer. The concept was introduced by McCulloch and co-workers beginning in the early 1940s [70]. ANNs have

been intensively used for solving regression and classification problems in many fields. Nowadays, ANNs have been used in the areas that require computational techniques, such as pattern recognition, optical character recognition, predicting outcomes, and problem classification. In materials science and engineering fields, ANN modelling techniques have been used to predict the properties of materials including the toughness. Several researches explored the potential use of artificial neural networks (ANNs) in the field of fracture mechanics [71].

Guan and co-workers applied an artificial neural network (ANN) to predict the fracture toughness of directionally solidified Nb-silicide in in/situ composites. Both microstructural features and composition of the constituent phases were employed as inputs of the ANN model while the output was fracture toughness of the composites [72].

Partheepan and co-worker applied feed-forward neural networks to investigate the fracture toughness value of in-service materials. The ANN trained with comprehensive dataset collected from various sources of literature and also from the load–elongation computed from the finite element (FE) simulation. The input of the ANN was the miniature test load–elongation diagram while the fracture toughness value of the materials was used as output. His study showed that neural network model predicted the fracture toughness value close to the standard test value [73].

Seibi and co-workers applied ANNs to predict the average fracture toughness, $\overline{K_c}$, of 7075- T651 aluminium alloy under uni- as well as biaxial loading at the room and higher temperatures. The fracture toughness prediction follows from the evaluation of critical values of *J*-integral from experimental data. The model was based on the parameters that affect the fracture toughness value. And he showed that ANN is an excellent analytical tool that, if properly used, can reduce cost, time and enhance structure reliability [74].

Çöl and co-workers developed a generalised regression neural network to predict the impact energy as a function of experimental-test conditions. The predicted values of the impact energy using the ANN were found to be in good agreement with the actual values from the experiments [75].

ANN back-propagation model was used [77] to investigate the fracture toughness behaviour and tensile strength as a function of steel microstructure. The primary objective of their model was to validate and extend the application of microalloy steels for various engineering applications. ANN back-propagation training model was found to be in good agreement with the experimental results [76]. Kang and co-workers used a back-propagation neural network to predict the K_{IC} values using tensile test data. His study showed that the

ANN can be a good tool to predict K_{IC} values according to the variation of the temperature and the crack plane orientation using tensile test results [77].

Dunne and co-workers used an artificial neural networks (ANNs) to the predict the Charpy impact toughness of quenched and tempered (QT) steels [78]. In his study he showed that the capacity of ANNs to handle the problems involving large sets of input variables to predict the impact energy of weld metal (WM) produced by flux cored arc welding (FCAW).

Abdulbaky and co-workers developed quantitative models for the prediction of fracture toughness using experimental data collected from the literature, together with an ANN. They proposed model of fracture toughness, based on chemical composition, heat treatment and mechanical properties. The predictions of fracture toughness were generally acceptable but the uncertainties have been found to be high and more input data need to be collected (for super-bainitic steels) to improve the predictions by using this model [79, 80].

Abendroth and co-workers used artificial neural networks to identify the ductile damage and fracture parameters from the small punch test experimental data [81]. MacKay [82] developed a particularly useful treatment of Bayesian framework for back-propagation feed-forward ANNs, which allows calculation of error bars for model predictions and quantifies the significance of each input parameter automatically. This method has advantages in investigating the influence of many input parameters on a specific output. Pak and co-workers used artificial neural network to investigate Charpy toughness of steel welds [83].

Ichikawa et al. [84] applied a classification ANN with a Bayesian framework to predict occurrence of solidification cracking in low alloy steel welds. Cool and co-workers [85] applied a committee of ANN within a Bayesian framework to predict strength of weld joints. This approach was found to improve quality of prediction once the input data are sparse and reliability of prediction is low. Bhadeshia [86] in general has reviewed the applicability of neural networks to materials science problems and has highlighted recommendations on how ANNs theory can be applied.

As already mentioned (in chapter 2.3) thanks to master curve concept the evaluation of differences in transition behavior of steels caused by microstructural changes e.g. (due the operational degradation) is possible based on one parameter - reference temperature T_0 [87, 88]. Only one parameter, i.e. the reference temperature, is thus needed in order to describe the transition region of fracture toughness values quantitatively. Except for standard determination procedures of this parameter there are different approaches under

development how to estimate it indirectly. There is a unique opportunity to employ ANNs to predict this temperature on their output side looking for suitable parameters on their input side [89].

2.6.1 Bayesian Neural Network

Artificial neural network (ANN) is an information processing model derived from the human brain processes information treatment [90]. An ANN consists of interconnected nodes that work together to perform an output function. The connections between nodes have numeric weights that can be adjusted based on experience enabling the network to be adaptive to inputs and capable of learning. Neural networks can be used to model complex relationships between inputs and outputs or to fit a function to a number of points in the data space. Neural networks are powerful non-linear regression methods, especially when the underlying data relationship is poorly understood. ANNs can identify and learn correlated patterns between input data sets and corresponding target values. Neural networks have been studied intensively [91].

In the present work, a Bayesian technique has been used for learning or training ANNs because it offers as few assumptions as possible about the form that fits the data, while trying to simulate its shape [92]. The Bayesian method assumes that the function modelled should be continuous and differentiable. The method has an outstanding treatment of uncertainties. Also, this method can find the significance of each input which refers to the amount of variation in the output that can be caused by a particular input.

Bayes' Theorem

Bayes theorem provides a direct method of calculating the probability of a hypothesis based on its prior probability, the probabilities of observing various data given the hypothesis, and the observed data itself. The Bayes' rule can be used to determine the posterior probability of hypothesis *h* given data *D*:

$$P(h/D) = \frac{P(D/h)P(h)}{P(D)}, \tag{34}$$

in this formula, $P(h/D)$ is the posterior probability of h given data D. $P(h)$ is the prior probability of h before having seen the data D. $P(D)$ is the prior probability of D (probability that D will be observed). $P(D/h)$ is the probability of the data D for given h and is called the likelihood.

Acquiring the weights in the Bayesian neural networks means changing the weights from the prior $P(w)$ to the posterior $P(w/D)$, as a result of observing data [93, 94]. Error

bars can also be placed on the output of the network, by considering the shape of the output distribution, $P(y/D)$, with this method.

It was assumed that the material property of interest in this case was the reference temperature T_0 of a particular steel, and that it can be expressed as a non-linear function f, of a number of experimental variables in the database:

$$T_0 = f(R_m, R_e, \sigma_m, \sigma_u, \dots), \tag{35}$$

where R_m refers to the ultimate tensile stress, R_e represents the yield stress of the steel, σ_m is the true stress at ultimate stress, σ_u is fracture stress, and all the other parameters that might influence the T_0.

2.6.2 Structure of the Neural Network

In the three-layer feed-forward neural network the first layer consists of the inputs to the network, the next layer consists of a number of non-linear operators h_i which form the hidden layer, and the third layer consists of the output function (z), see Fig. 15. Data moves in only from the input nodes, through the hidden nodes and to the output node. There are no loops in the network; every node in a layer is connected with all the nodes in the previous layer, hence called feed-forward ANN. Each connection may have a different weight. The activation function for i^{th} node is given by following equation [95]:

$$h_i = tanh\left(\sum_j w_{ij}^{(1)} x_i + \theta_i^{(1)}\right). \tag{36}$$

The output is given by equation:

$$y = \sum_i w_{ij}^{(2)} h_i + \theta^{(2)}, \tag{37}$$

where x_i are inputs, and w_{ij} are the weights which define the network. The superscripts $^{(1)}$ and $^{(2)}$ denote weights and biases in the hidden layer and in the output layer. The optimum value for w is obtained through training a network. The parameters θ are known as biases.

The complexity of any ANN increases by increasing the number of hidden units. During the training phase the inputs are known, the output is known, and the weight can be examined. In order to find the interactions between inputs and output a model makes predictions and visualises the behaviour which emerges from various combinations of inputs [95].

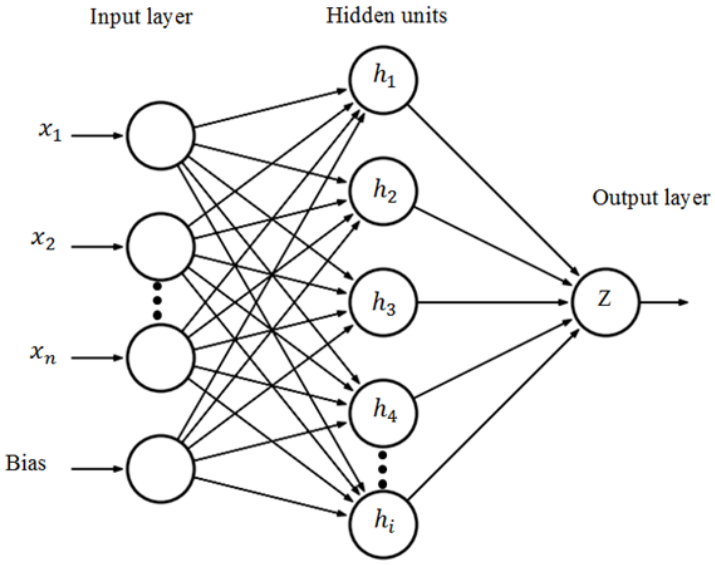

Fig. 15 A typical three-layer feed-forward artificial neural network architecture.

One of the problems that can occur during neural network training is called overfitting, which leads to an unjustified level of accuracy and thus, a high level of complexity. If a model is too complex it may give poor generalization (overfitting). Overfitting occurs when a network has memorized the training set but has not learned to generalize to new inputs. Overfitting produces a relatively small error on the training set but a much larger error when new data is presented to the network. Training a network includes finding a set of weights and biases which balances between complexity and accuracy as illustrated in the following equation [95, 96]:

$$M(w) = \alpha E_w + \beta E_D, \tag{38}$$

where E_w is an organizer of the complexity. It forces the network to use small weights and limited number of hidden units:

$$E_w = \frac{1}{2}\sum_{ij} w_{ij}^2, \tag{39}$$

E_D is the overall error between target output values and network output values:

$$E_D = \frac{1}{2}\sum_{k} (t^k - y^k)^2, \tag{40}$$

where t^k represents the set of targets for the set of inputs x^k, and y^k represents the set of corresponding network outputs. α and β represent control parameters which define the balance between complexity and accuracy of the model. The training algorithm updates the

weights and biases to minimise a combination of squared errors and weights and then determines the correct combination so as to produce a network that generalizes well.

3 THE AIM OF THE THESES

Due to cost considerations and small amounts of available material, it can be important to identify the properties of materials using simplified methods. Similar need is evident when characterising local fracture behaviour in (heterogeneous) weld joints. Artificial neural networks (ANNs) can be used to model the complex relationship between inputs and outputs, and fit a function to a number of points in the data space. For quantification of the fracture toughness transition behaviour this is unique opportunity because only one value (on the output side) is enough. Artificial neural networks are powerful non-linear regression methods, especially when the underlying data relationship is poorly understood. ANNs can identify and learn correlated patterns between input data sets and the corresponding target values.

Following the recent stage of the art the purpose of study is twofold: (i) experimental evaluation of fracture toughness transition evaluation of the dissimilar weld joints and (ii) artificial neural network development for reference temperature and transition behaviour prediction.

The aim of the study is to verify the validity of the master curve concept for evaluation of the dissimilar weld joints and/or thermally aged weld joints. In order to solve the problem the following subtasks have been formulated:

- Verification of the applicability of the master curve concept for the weld material evaluation, in particular when dissimilar steels are used.
- Determination of the reference temperature for purpose of the fracture toughness transition evaluation and its prediction.

In addition, the thesis is focused on development of quantitative models for the prediction of reference temperature characterising position of the fracture toughness transition on the temperature axis using experimental data collected from tensile tests, together with a powerful computational technique known as artificial neural network. In order to solve this problem the following subtasks must be addressed:

- Collection and completion if needed of data sets for suitable steels for ANN training. Note that for purposes of ANN training the data generated by different tests must be evidently from the same steel batch.
- Selection of the corresponding neural network, computing tools and settings for development of ANN enabling T_0 prediction.

4 MATERIALS, TEST SPECIMENS AND METHODS

4.1 Investigated Materials

4.1.1 Weld Joints

The experimental material used was low carbon steel from dissimilar weld joints of low carbon ferritic steel and austenitic steel. Two locations were selected for experimental: basic material (C20) and the same material very near to fusion line (see Fig. 16). The original material was cut from a dissimilar weld joint of a steam generator. The chemical analysis was done by Leco, Spectrumat GDS 750 spectrometer. For investigated materials, i.e. low carbon steel C20, the chemical analysis is presented in Table 1. For the other materials of the weld joint only nominal compositions are supplied. The chemical composition of type W7 austenitic heat resistance steel is presented in Table 2. The weld joint was further made by overlay material using electrode of the type EA395/9, the chemical composition is shown in Table 3. The weld material itself was formed by electrode FOX SAS2, chemical composition is shown in Table 4.

Table 1 The chemical composition of low carbon steel C20 in [$wt\%$]

Material	C	Mn	Si	Cu	Ni	Cr	P	S
C20	0.21	0.60	0.34	0.20	0.23	0.25	0.015	0.012

Table 2 The chemical composition of type W7 austenitic heat resistance steel in [$wt\%$]

Material	C	Mn	Si	Cr	Ni	Ti
W7	max 0.10	max 2.00	max 1.00	17.0-19.0	9.00-12	0.80

Table 3 The chemical composition of the overlay formed by EA395/9 [$wt\%$]

Material	C	Mn	Si	Ni	Cr	Mo	Co
EA395/9	0.10	1.86	0.51	24.5	16.2	5.80	0.05

Table 4 The chemical composition of the weld metal FOX SAS2 [$wt\%$]

Material	C	Mn	Si	Cu	Ni	Cr
FOX SAS2	0.21	0.60	0.34	0.20	0.23	0.25

The basic material C20 and weld joint was tested in as received conditions. In addition, thermal ageing was applied at 450 °C for 500, 700 and 1000 hours respectively in

order to simulate long term operational degradation of the material. Samples for metallographic observations and mechanical testing have been cut from the pieces after heat treatment.

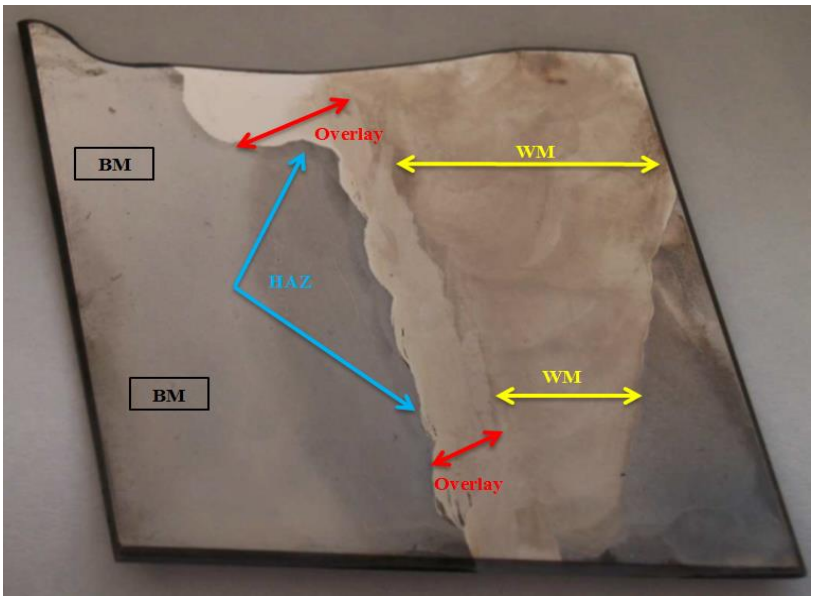

Fig. 16 Macrograph showing different location of the weld joint.

The microstructure of the base material, low carbon steel C20, consisted of basic ferritic microstructure with pearlitic island in fraction corresponding to carbon content. The ferritic grain size was lower than 19 μm (Fig. 17). The location very near to fusion line is formed by ferritic microstructure containing transformed mixture of bainitic, ferritic Widmanstatten and martensitic microstructure (Fig. 18)

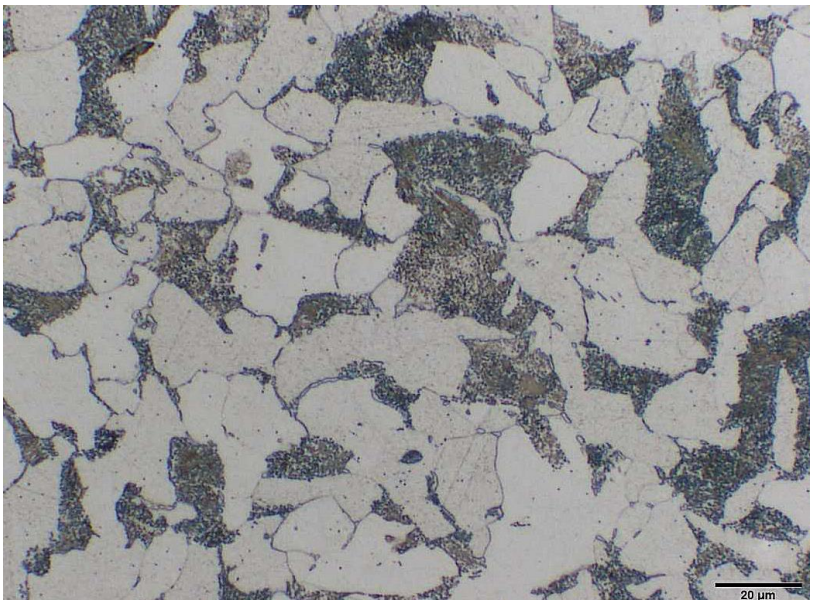

Fig. 17 Microstructure of the base material – low carbon ferritic steel C20 (Nital etching).

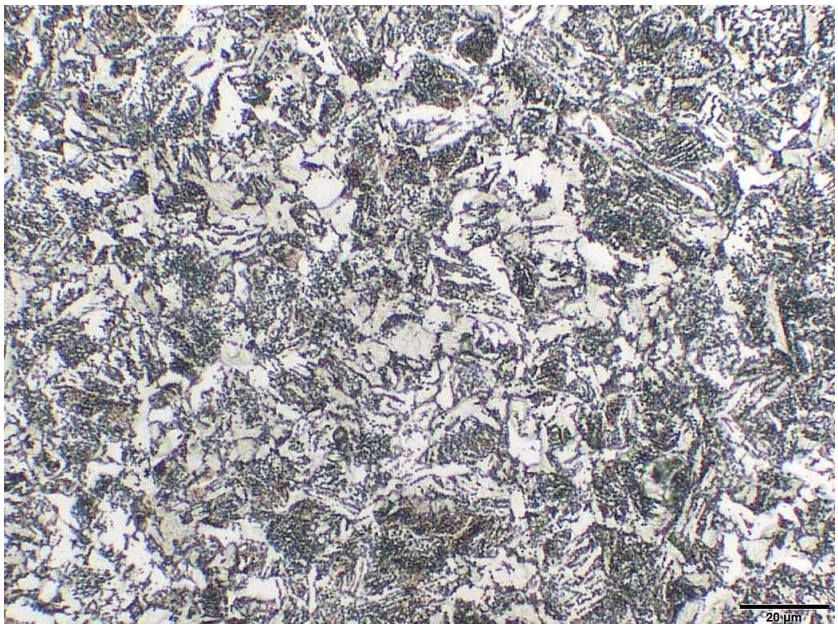

Fig. 18 Microstructure of the low carbon ferritic steel C20 very near in location about 100 µm from fusion line (Nital etching).

In order to characterise state of the steel across the weld joint, as well as across the thickness of the plate, hardness HV1 was tested. Fig. 19 shows locations in which the hardness was obtained.

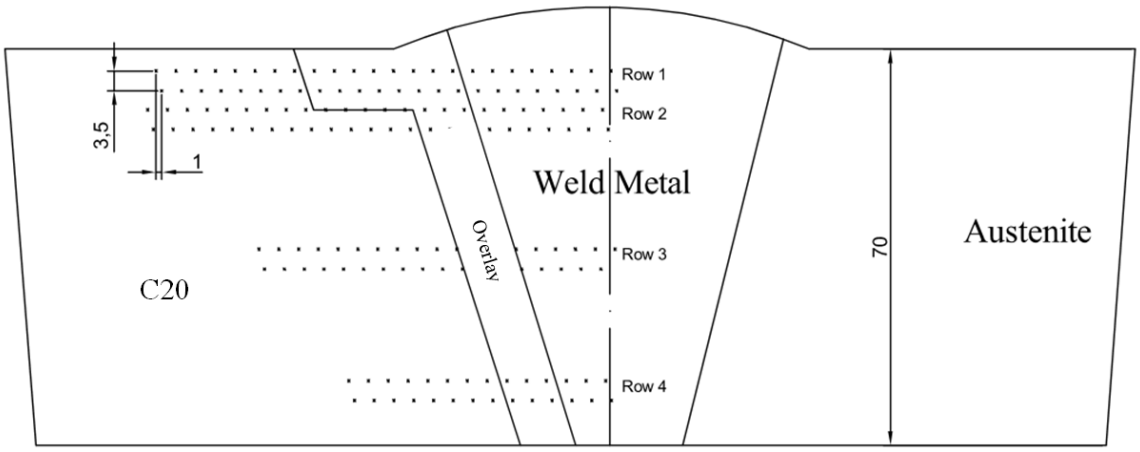

Fig. 19 Positioning of the indentations lines.

Fig. 20 to 23 show the dependences of hardness HV1 on the position of the hardness tester indenter. The first red line represents about the fusion line i.e. the boundary between the base material (C20) and its heat affected zone on the left side and overlay material. The second red line represents the boundary between the overlay and weld metal. In the row 1 (Fig. 20), the average value of hardness for the base material is 177 HV1, in the area of overlay is 234 HV1, and average value of hardness for the weld metal is 238 HV1.

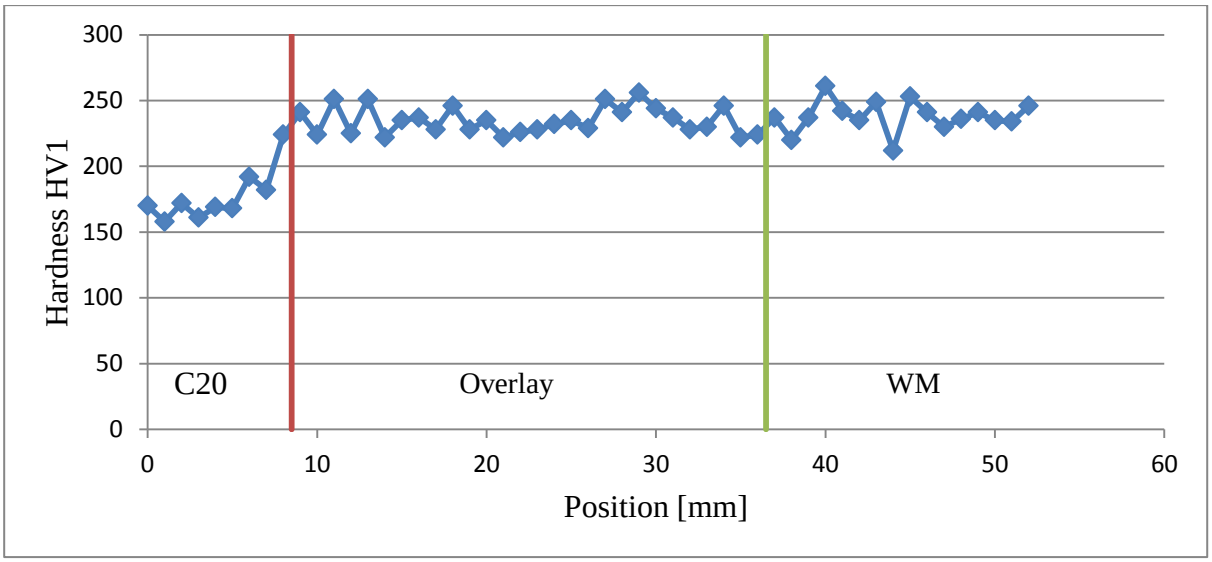

Fig. 20 The dependence of hardness HV1 on the position of the hardness tester indentor (Row 1).

In the row 2 (Fig. 21), the average value of hardness for the base material is 176 HV1, in the area of overly is 243 HV1, and average value of hardness for the weld joint is 241 HV1.

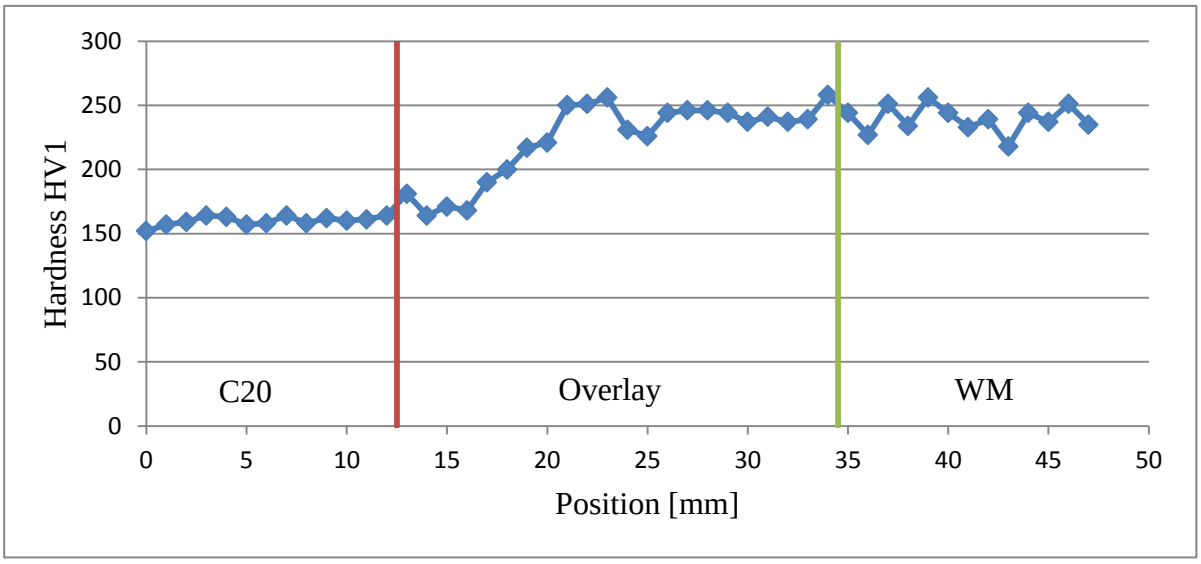

Fig. 21 The dependence of hardness HV1 on the position of the hardness tester indentor (Row 2).

In the row 3 (Fig. 22), the average value of hardness for the base material is 164 HV1, in the area of overlay is 243 HV1, and average value of hardness for the weld joint is 248 HV1.

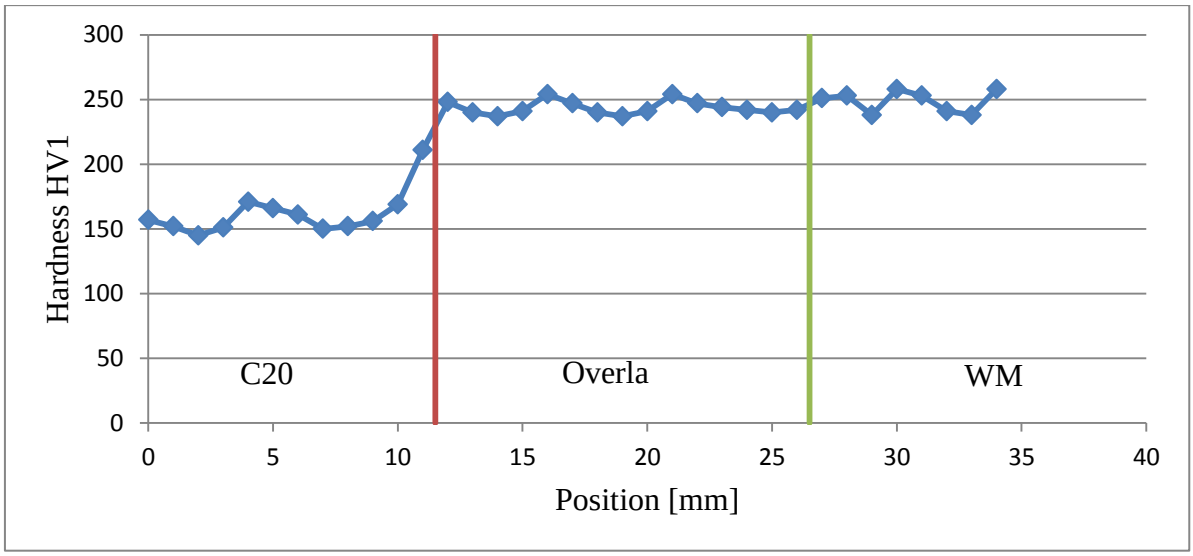

Fig. 22 The dependence of hardness HV1 on the position of the hardness tester indentor (Row 3).

In the row 4 (Fig. 23), the average value of hardness for the base material is 167 HV1, in the area of overlay is 240 HV1, and average value of hardness for the weld joint is 243 HV1.

Schematics in Fig. 24 shows location of hardness measurements on piece that was subject to simulation of thermal degradation at 475 °C.

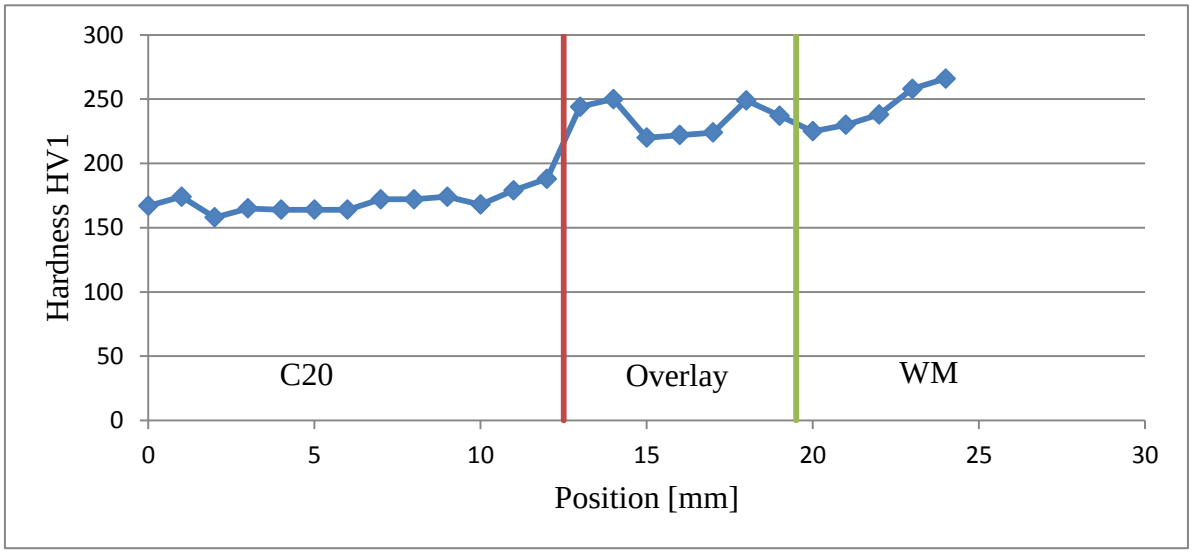

Fig. 23 The dependence of hardness HV1 on the position of the hardness tester indentor (Row 4).

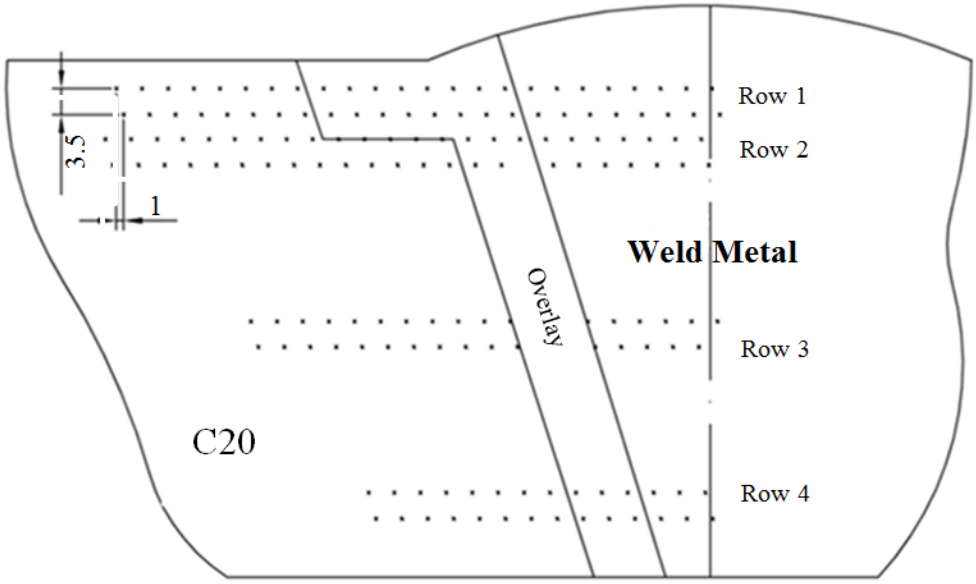

Fig. 24 Position of the indentations lines.

Fig. 25 to 28 show the dependence of hardness HV1 on the position of the hardness tester indenter. The first red line represents about the fusion line, i.e the boundary between the base material (C20) and its heat affected zone on the left side and overlay. The second red line represents the boundary between the fusion line and weld joint. In the row 1 (Fig. 25), the average value of hardness for the base material is 166 HV1, in the area of overlay is 247 HV1, and average value of hardness for the weld joint is 250 HV1.

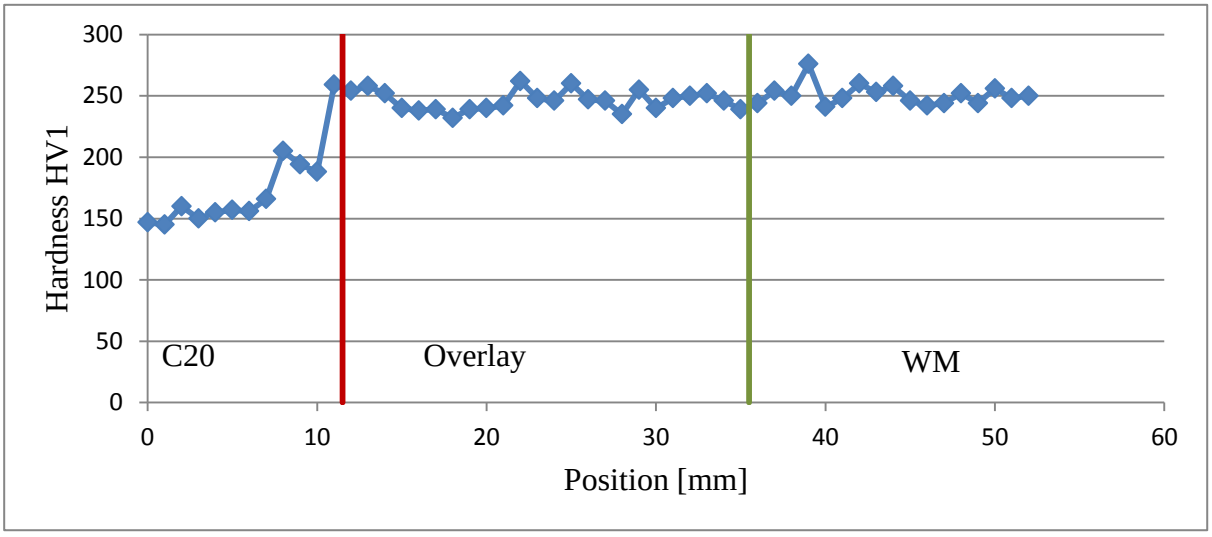

Fig. 25 The dependence of hardness HV1 on the position of the hardness tester indentor (Row 1).

In the row 2 (Fig. 26), the average value of hardness for the base material is 169 HV1, in the area of overlay is 255 HV1, and average value of hardness for the weld joint is 251 HV1.

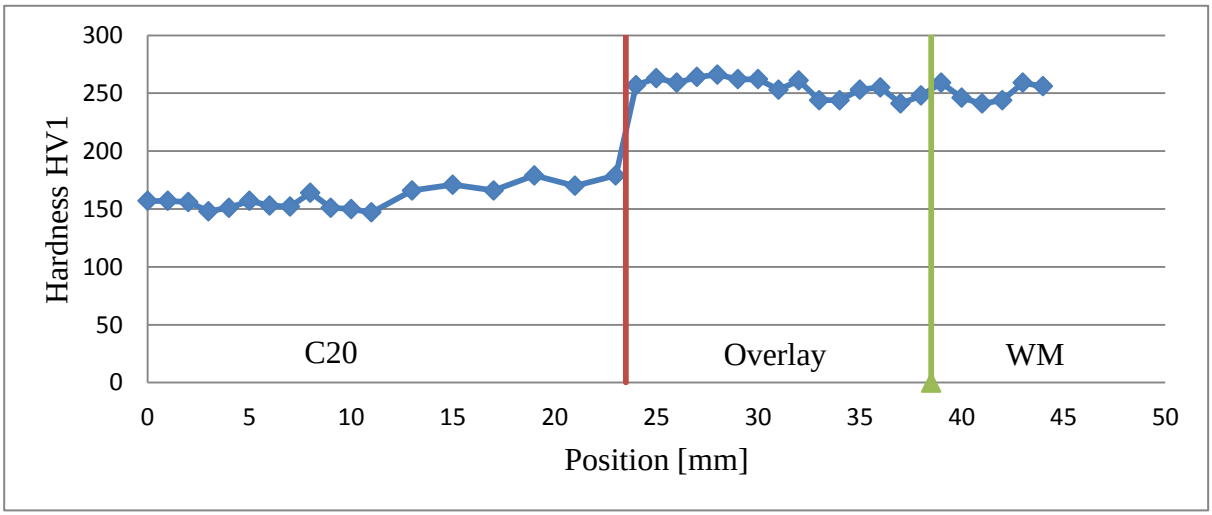

Fig. 26 The dependence of hardness HV1 on the position of the hardness tester indentor (Row 2).

In the row 3 (Fig. 27), the average value of hardness for the base material is 173 HV1, in the area of overlay is 260 HV1, and average value of hardness for the weld joint is 256 HV1.

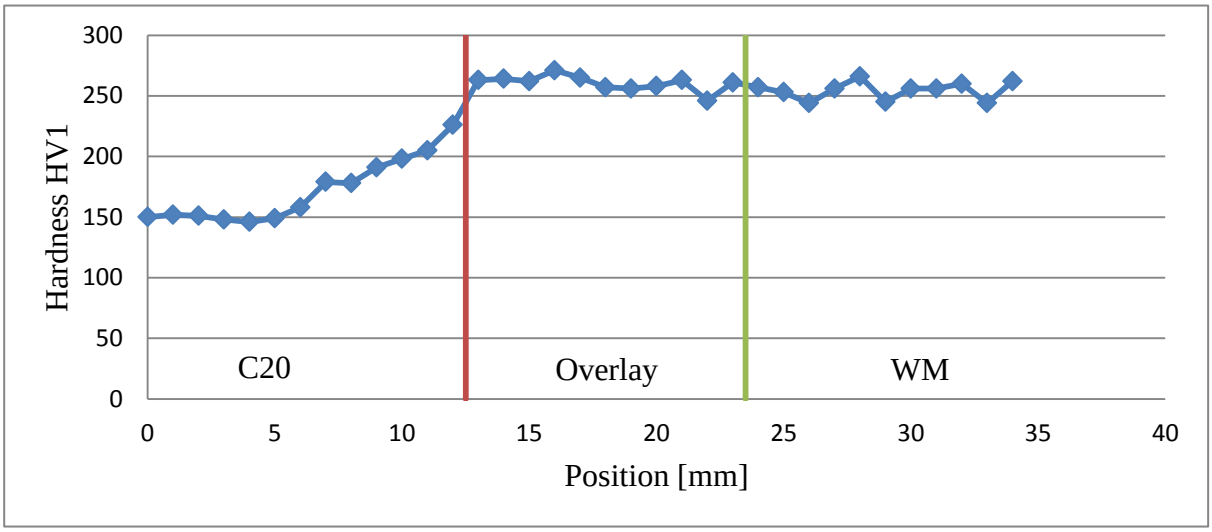

Fig. 27 The dependence of hardness HV1 on the position of the hardness tester indentor (Row 3).

For the row 4 (Fig. 28), the average value of hardness for the base material is 167 HV1, in the area of overlay is 258 HV1, and average value of hardness for the weld joint is 253 HV1.

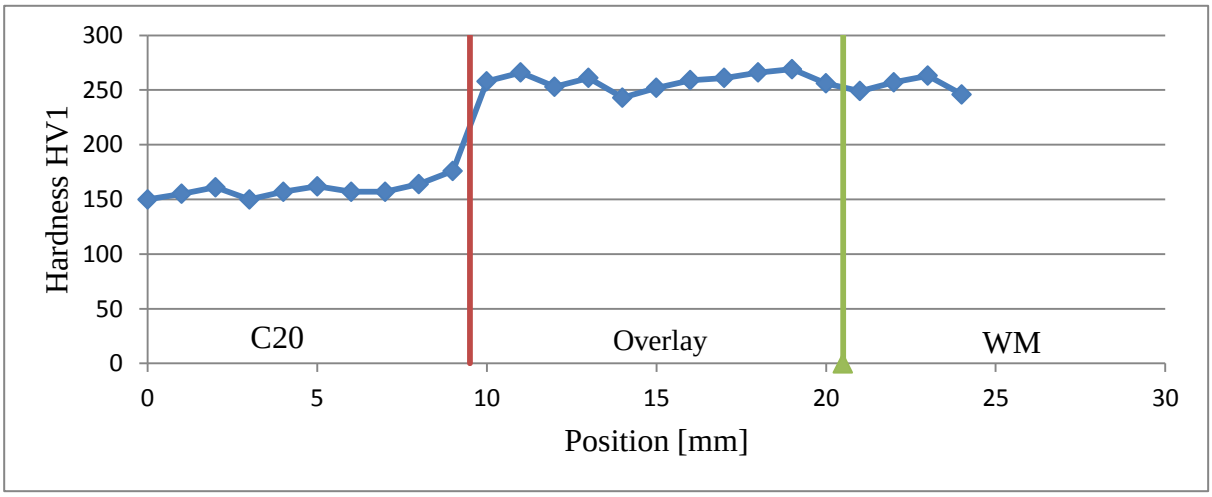

Fig. 28 The dependence of hardness HV1 on the position of the hardness tester indentor (Row 4).

4.1.2 Materials for Data Sets of ANN Development

A set of 29 steels containing material from various origins was also completed if when needed additional tests were carried out. The steels were predetermined for the development of ANN, involving the strict application of the following rules [89]: (i) the steels are used primarily in power engineering, (ii) the origin of the material has been well guaranteed, where possible by a certificate of history or manufacturing and a known geometry of the semi-finished product from which the specimens are made, and (iii) the properties of steel cover the range of the most common microstructures and yield strengths. For the purposes of this project, a total of 29 steels and states of steel of the following types (see Table 5) were collected and generated:

- Arema steel (α-iron) and ferritic cast steels (further labelled as A, S, C, E);
- low-carbon low-alloy steels commonly used e.g. for rotors of steam power generation, in microstructural experimental state and in states following operational exposure (c, d, F, G);
- low-allow (Cr)NiMo(V) steel in their original state and following operational exposure (s, t, M, V, D);
- advanced steels under-development for thick-walled forgings (K, L);
- ferritic weldable sheet steels (N, O, p);

- nuclear reactor pressure vessel steels for VVER-440 and VVER-1000 power station in basic state and model states (J; X; Y; Z);
- boiler and pipe steels with increased yield strength (T, I, H, a);
- pearlitic and bainitic steels applied in railway components (P, B, R) to cover the high yield strength end of the steels scale.

Table 5 Set of 29 tested steels containing material of various origins.

Indication	Metallurgical mark	Description / origin	Microstructue
A	Fe	arema	ferrite
N	FeMn	sheet material-as received	ferrite-pearlite
O	FeMn	sheet material-as received	ferrite-pearlite
P	FeMn	sheet material-as received	ferrite-pearlite
S	FeMn	cast steel for thick walled container	ferrite
C	FeMn	cast steel for thick walled container	ferrite
E	FeMn	cast steel for thick walled container	ferrite
S	CrV	cold end of rotor-Steti	pearlite-ferrite
L	42CrMo4	thick walled forging-axial part	pearlite-ferrite
R	45Mn	railway wheelset steel R7T	pearlite
H	CrMoV	pipes from P91	temp. mart.-bainite
t	NiWV	hot end from rotor-Steti	temp. bainite
a		steel TRIP-as received state	temp. bainite
d	CrMoV	cold end of rotor-Porici	temp. bainite
c	CrMoV	hot end of rotor-Porici	temp. bainite
G	CrMoV	carbide triggered cleavage	temp. bainite
F	CrMoV	dislocation triggered cleavage	temp. bainite
J	10Ch2MFA	RPV steel VVER 440	temp. bainit e-martensite
T	CrNi	boiler steel	temp. bainite
I	CrNi	boiler steel aged	temp. bainite

X	15Ch2NMFAA	RPV steel VVER 1000	temp. bainite-martensite
Y	15Ch2NMFAA	RPV steel VVER 1000 - model	temp. bainite-martensite
Z	15Ch2NMFAA	RPV steel VVER 1000 - model	temp. bainite-martensite
V	20 CrNiMoV	rotor steel 500 MW – axial part	temp. bainite-martensite
M	20 CrNiMoV	rotor steel 500 MW - surface	temp. bainite-martensite
B	Lo8CrNiMo	cast bainitic steel	bainite
K	42CrMo4	thick walled forging - surface	bainite
P	Lo17CrNiMo	cast bainitic steel	bainite
D	CrMoV	rotor steel	bainite-martensite

4.2 Mechanical and Fracture Mechanical Testing

For mechanical testing the tensile test samples were cut according to schematics shown in Fig. 29. There were two locations from which the material has been selected: the base material, steel C20, having homogeneous ferritic microstructure and location very near to fusion line, about 100 μm from the fusion line (Fig. 29). This location has been selected as the most brittle part of the weld joint.

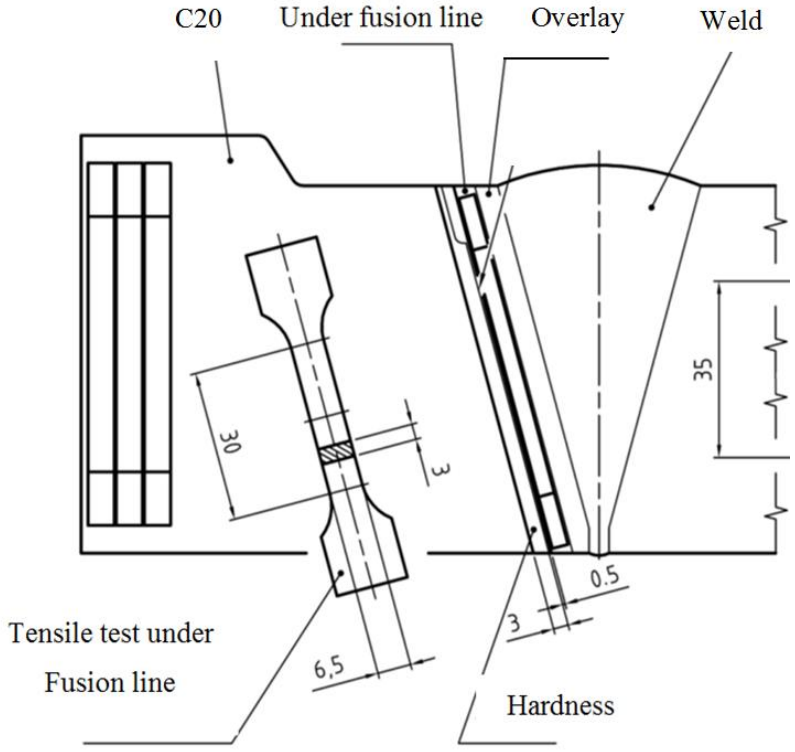

Fig. 29 Cutting plans, samples preparation.

The compact tension and bend samples have been oriented in order to get through thickness crack propagation. For base material this orientation was kept exactly, for the location near the fusion line the crack propagation in distance from 30 to 100 μm was expected and the crack propagation plane was slightly declined as it follows for tensile test samples from Fig. 29.

4.2.1 Experimental Determination of the Fracture Toughness K_{IC} and K_{JC} using CT specimen

For compact tension samples taken from the vicinity of the fusion line the initial crack was located into distance 50 to 80 μm from the fusion line seen on the specimen surface. This localisation followed from hardness measurements showing that there is highest hardness and thus predisposition to brittle fracture behaviour has been expected. Before final machining of the compact tension sample the semifinished piece was slightly etched by Nital agent to show the fusion line between steel C20 and overlay alloy, then the axial plane of the initiating chevron notch was located into the particular piece and sample was then finished to its final dimensions. During fatigue pre-cracking it was good chance to get the crack tip into expected distance from the fusion line, the example of real crack tip configuration is evident from Fig. 30. Note however that the fusion line is not straight and it was very often observed that the crack was propagating partly also through the locations corresponding to overlay material.

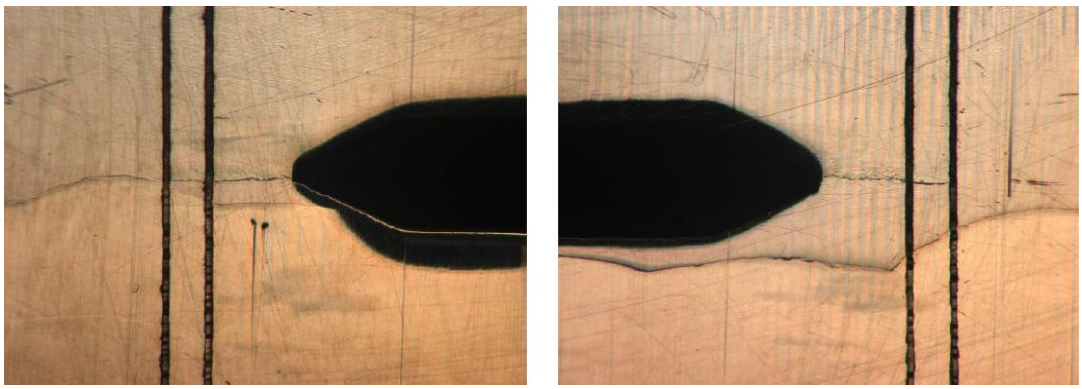

Fig. 30 Example of the fatigue crack tip localisation near the fusion line (overlay below the fusion line, steel C20 above the fusion line.

In order to determine the fracture toughness, standard testing conditions and test specimens were used in accordance with the ASTM E 399 [15]. The test was completed at the laboratory of the Institute of Physics of Materials at the Academy of Sciences of the Czech Republic. The compact tension (CT) specimen used had dimensions of

25×62.5×60 mm^3 and its geometry is shown in Fig. 31. Cyclic loading was applied to achieve the pre-cracked condition with a ratio of the crack length to specimen width of approximately $a/w \approx 0.5$. The specimens were tested on mechanical screw driven machine Zwick 1380, with a maximum loading capacity of 200 kN. The fracture toughness tests were performed at different temperatures, where the specimens were cooled down to a stable temperature in a cryogenic chamber using liquid nitrogen and the temperature was controlled by thermometers couple spot welded to the sample. The crack opening was measured by an external displacement-measuring clip on gage at the load line. An optical microscope was used on the fracture surfaces of broken samples to measure the initial crack lengths a_0 of the tested specimens. The value of fracture load F_Q was obtained from a plot of load vs. load displacement curves according to [16]. The stress intensity factor for the fracture conditions was obtained by the following equation:

$$K_Q = \left[\frac{F}{B.W^{1/2}}\right].g\left(\frac{a_0}{W}\right), \tag{41}$$

where B and W are the thickness and the width of specimens respectively, a_0 is the initial crack length, and function $g\left(\frac{a_0}{W}\right)$ represents the geometrical function given by the following equation:

$$g\left(\frac{a_0}{W}\right) = \frac{\left(2+\frac{a_0}{W}\right)\left[0.886 + 4.64\frac{a_0}{W} - 13.32\left(\frac{a_0}{W}\right)^2 + 14.72\left(\frac{a_0}{W}\right)^3 - 5.6\left(\frac{a_0}{W}\right)^4\right]}{\left(1-\frac{a_0}{W}\right)^{1.5}}. \tag{42}$$

In order to validate the values of K_Q as K_{IC} the following requirements have been checked according the standard ASTM E399 [15]:

$$B, a \geq 2.5\left(\frac{K_Q}{\sigma_{YS}}\right)^2, \tag{43}$$

$$0.45 \leq \frac{a}{W} \leq 0.55\,, \tag{44}$$

$$F_{max} \leq 1.10F_Q, \tag{45}$$

where σ_{YS} is the yield stress.

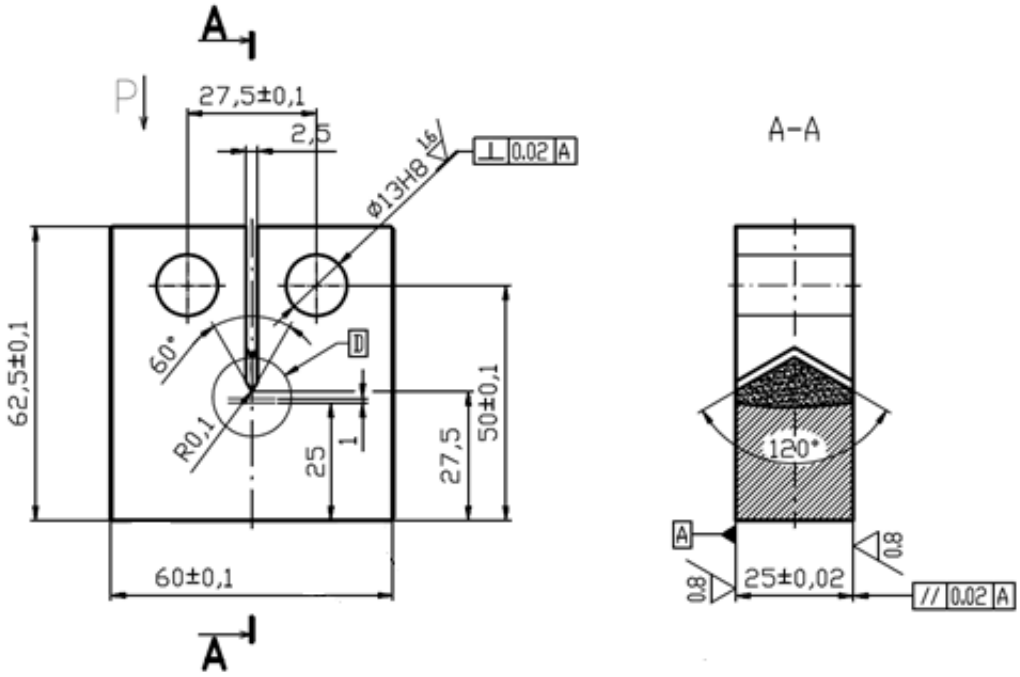

Fig. 31 The compact tension CT specimen.

For tests that did not reached the above conditions, i.e. the crack tip plasticity was too extensive, the *J*-integral concept was used to evaluate the fracture behaviour according to ISO 12135 [16]. The *J*-integral value was obtained by the following equation:

$$J = J_e + J_P. \tag{46}$$

The elastic component was calculated using the following equation:

$$J_e = \frac{K_Q^2(1-v^2)}{E} \tag{47}$$

The plastic component was obtained from plastic deformation energy U_p as follows:

$$J_P = \frac{\eta_p U_p}{(B_N . b_0)}. \tag{48}$$

After checking the validity condition for J_Q-integral the value of K_{Jc} was then calculated for each individual specimen depending on the corresponding J_c value as follows:

$$K_{Jc} = \sqrt{\frac{J_C E}{(1-v^2)}} = \sqrt{J_c E'}. \tag{49}$$

4.2.2 Experimental Determination of the Fracture Toughness Using Three-Point Bend Specimens

Test specimens measuring 25×50×240 mm (Fig. 32), produced from a single sheet, were also used to determine the fracture toughness. The specimens crack planes were oriented in direction corresponding about to realistic loading conditions.

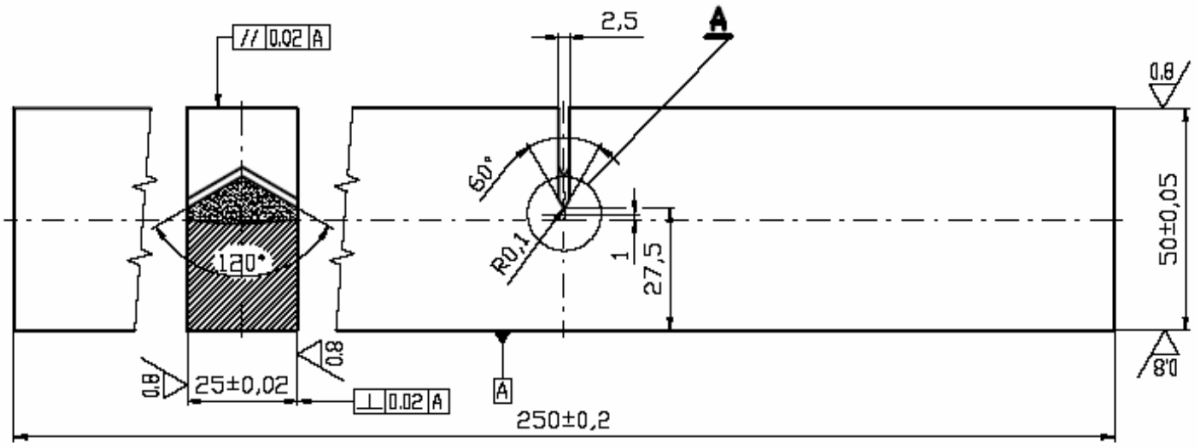

Fig. 32 The geometry of the test specimen used for determination of fracture toughness.

After checking the specimens dimensions, surface quality etc., the test specimens were finished by standard procedures, and after polishing the surface, sharp crack was introduced by cyclic loading in accordance with the standard [16]. Based on published data to particular steel the position of the transition region was estimated and the tests were conducted at selected three different test temperatures on a Zwick 1382 testing machine in the cryogenic chamber, and also on the Instron 8862 machine in a temperature chamber, in both cases at a loading rate of 1 mm/min. The temperature was measured by a thermocouple spot welded on the surface of specimens for all tests. Before the test, all specimens were tempered for 15 min at the test temperature. The air was circulated in the temperature chamber in the case of heating. Results were recorded during the tests for later evaluation by standard procedures (e.g. in accordance with ISO 12135 [16]) using LDC home-made software or Instron BlueHill commercial software. This approach allowed the same evaluation procedures for all steels and facilitated the presentation of results, including qualification and control of the validity of calculation values of fracture toughness. The calculated values of fracture toughness were obtained using the equation:

$$K_Q = \left[\left(\frac{S}{W}\right)\frac{F_Q}{(B^2.W)^{1/2}}\right].g_1\left(\frac{a_0}{W}\right). \quad (50)$$

$$g_1\left(\frac{a_0}{W}\right) = \frac{3\left(\frac{a_0}{W}\right)^{1/2}\left[1.99 - \left(\frac{a_0}{W}\right)\left(1 - \frac{a_0}{W}\right)\left(2.15 - \frac{3.93.a_0}{W} + \frac{2.7.{a_0}^2}{W}\right)\right]}{2\left(1 + \frac{2.a_0}{W}\right)\left(1 - \frac{a_0}{W}\right)^{1.5}}, \quad (51)$$

where B, W are the dimensions of the test specimen, S is the distance of loading rollers (standard flexure specimens 200 mm), a_0 is the initial length of crack measured on 9 locations at a cross of specimen thickness. F_Q is the calculation force representing either load defined by 5% deviation of the tangent slope of the linear part of the record, or the fracture force.

If the data fulfilled the following validity conditions:

$$F_{max} \leq 1.10F_Q, \quad (52)$$

$$a_0, B, (W - a_0) \geq 2.5\left(\frac{K_Q}{\sigma_{YS}}\right)^2, \quad (53)$$

the calculated value of the fracture toughness was qualified as K_{Ic}. In the case that any of these conditions were not fulfilled, it was necessary to proceed to the evaluation of elastic-plastic fracture toughness K_{Jc}.

In this case, firstly the evaluated value of the *J*-integral was obtained, in accordance with the following relation in which U_P is a plastic work to fracture:

$$J_C = \left[\frac{F_C.S}{B.W^{1/2}}.g_1\left(\frac{a_0}{W}\right)\right]^2\left[\frac{1 - V^2}{E}\right] + \frac{2.U_P}{B(W - a_0)}. \quad (54)$$

Assuming the validity of the relation

$$\Delta a < 0.2 + \frac{J_C}{3.75.R_m}, \quad (55)$$

the *J*-integral values were converted into the values of elastic-plastic fracture toughness K_{Jc}, in accordance with the relation:

$$K_{Jc} = \sqrt{\frac{E.J}{1 - V^2}}. \quad (56)$$

The data that do not fulfil the conditions

$$K_{Jc(limit)} = \sqrt{\frac{E.b_0.R_{P0.2}}{30.(1 - V^2)}}, \quad (57)$$

where eliminated from further evaluation because they depends on the crack tip constraint. Uncorrected, these values do not represent the real behaviour of the material.

To determine the reference temperature T_0, it was necessary to determine at least 7 significant values of fracture toughness K_{Ic} or K_{Jc}. In most cases, the reference temperature was determined by the multi temperature method, according to the following basic equation:

$$\sum_{i=1}^{N} \frac{exp[0{,}019(T-T_0)]}{11+77\,exp[0{,}019(T-T_0)]} - \sum_{i=1}^{N} \frac{\left(K_{Jc(i)}-20\right)^4 exp[0{,}019(T-T_0)]}{(11+77\,exp[0{,}019(T-T_0)])^5} = 0. \tag{58}$$

In adequate cases, the reference temperature T_0 was determined by the single temperature method (ASTM E 1921 [36]), defined by the equation:

$$T_0 = T - \frac{1}{0.019} ln\left[\frac{K_{Jc(med)}-30}{70}\right]. \tag{59}$$

Despite the relatively small number of measurements, the reference temperature was determined with very high reliability.

4.3 Tensile Tests

4.3.1 Tensile Test of Smooth Bars

Bars were used for the purpose of the standard tensile test, the geometry of which is shown in Fig. 33. The bars were produced by the institutional workshops. Bars for the tensile test were cut from the fracture halves of the bending specimens. Bars with a smaller cross-section ($5mm$) and shorter lengths were produced.

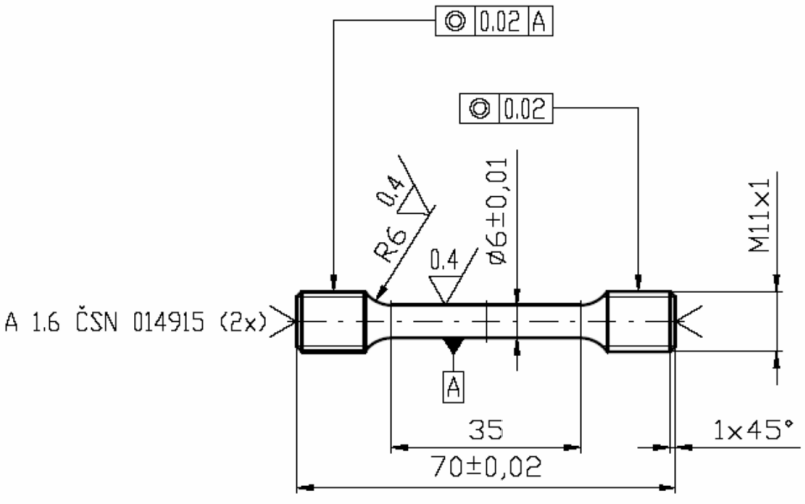

Fig. 33 The geometry of the test bar used for tensile test.

The bars were measured before the test and assigned to a surface length L_0 (30, and/or 25 mm). The tests were conducted at a loading rate of 2 mm/min using a extensometer. Room temperature tests were performed on a Zwick Z050 testing machine using a

macrosensor and TestXpert evaluation software. The lower temperature tests were performed in a cryogenic chamber on a Zwick 1382 test machine using the extensometer MTS with home-made measurement program (running in LabView environment). The higher temperature tests were performed in the appropriate temperature chamber on the Instron machine using the same sensor and BlueHill measurement program. The sensor was not used in tests where there was a risk of damage as a result of impact from the bar.

The primary data from the test machines and measurements of the test bars on the Mitutoyo microscope were inserted into the pre-programmed spreadsheets in MS Excel; these were a load of yielding of strength of $F_{\mathrm{e}}, F_{\mathrm{eL}}, F_{\mathrm{P0.2}}$ respectively, maximum load F_{m} and fracture load F_{u}. Furthermore, dimensions of the test bars were measured; the diameter outside of neck D_{r}, the diameter in the narrowest part of the neck D_{u}, the distance of the marks L_{u}, etc. According to the standard, following engineering characteristics were evaluated from the primary data:

$$R_e = \frac{F_e}{S_0}, \tag{60}$$

$$R_m = \frac{F_{max}}{S_0}. \tag{61}$$

The total elongation A_5 was determined as follows:

$$A_5 = \frac{L_u - L_0}{L_o}.100, \tag{62}$$

Reduction in area was calculated by using equation:

$$Z_r = \frac{S_0 - S_r}{S_0}.100. \tag{63}$$

They were also evaluated following physical parameters characterizing the dependence of the true stress vs true strain curve:

True stress on the plastic instability limit at σ_m was obtained from equation:

$$\sigma_m = R_m.\frac{S_0}{S_r}. \tag{64}$$

True deformation on the limit of elasticity $\bar{\varepsilon}_{\mathrm{pn}}$

$$\bar{\varepsilon}_{pn} = ln\left[\frac{S_0}{S_r}\right], \tag{65}$$

And similar characteristics were evaluated for fracture condition, i.e. true stress at fracture as

$$\sigma_u = \frac{F_u}{S_u}. \tag{66}$$

And true strain at fracture as

$$\bar{\varepsilon_u} = 2.ln\left[\frac{d_0}{d_u}\right] = ln\left[\frac{S_0}{S_u}\right]. \tag{67}$$

Then the true stress at fracture was corrected for the stress triaxiality effect by means of Bridgman correction.

$$\sigma_{uB=}\sigma_u.\left(0.83 - 0.1786\, log\, \bar{\varepsilon_f}\right). \tag{68}$$

The slope of a line characterizing the tensile diagram beyond the plastic instability limit was suggested as one of new parameters and calculated using the equation:

$$tg\ \alpha = \frac{\sigma_u - \sigma_m}{\bar{\varepsilon_u} - \bar{\varepsilon_m}}. \tag{69}$$

Temperature dependences were compiled and the scattering of data at room temperature and at the critical brittleness temperature of embrittlement were evaluated for parameters selected for neural analysis. The test was repeated in the case of anomalous scattering or values deviating significantly from the hypothetical level projected by temperature dependence.

4.3.2 Tensile Test of Notched Bars

The geometry of the used test bars with a circumferential notch is shown in Fig. 34. The geometry of notch was chosen so that embrittlement occurred even for the toughest materials at temperatures higher than the temperature of liquid nitrogen. These two steels of the class 16 were excluded from further experiments because of the high plasticity at the temperature of liquid nitrogen.

The longitudinal axis of the notched bars was chosen to be coincident with the longitudinal axis of the smooth bars. Based on the FEM calculations, a relatively homogeneous distribution of tensile stress was found in the cross-section of notched bars, maintaining the reproducible conditions of this non-standardised test.

The aim of the test was to determine the general yield temperature t_{gy} for the used geometry of the test specimen and loading conditions. This temperature is defined as the temperature at which fracture occurs at the moment achieving macroplastic deformation (plasticization of the whole cross-section under the notch), i.e. as the temperature at which the force on the limit of macroplastic deformations coincides with the fracture strength. The

critical brittleness temperature except of material behavior, is dependent on the geometry of the test bar. To estimate the force (stress) corresponding to this limit of macroplastic deformations, it would be necessary to perform calculations by the finite element method for each test bar.

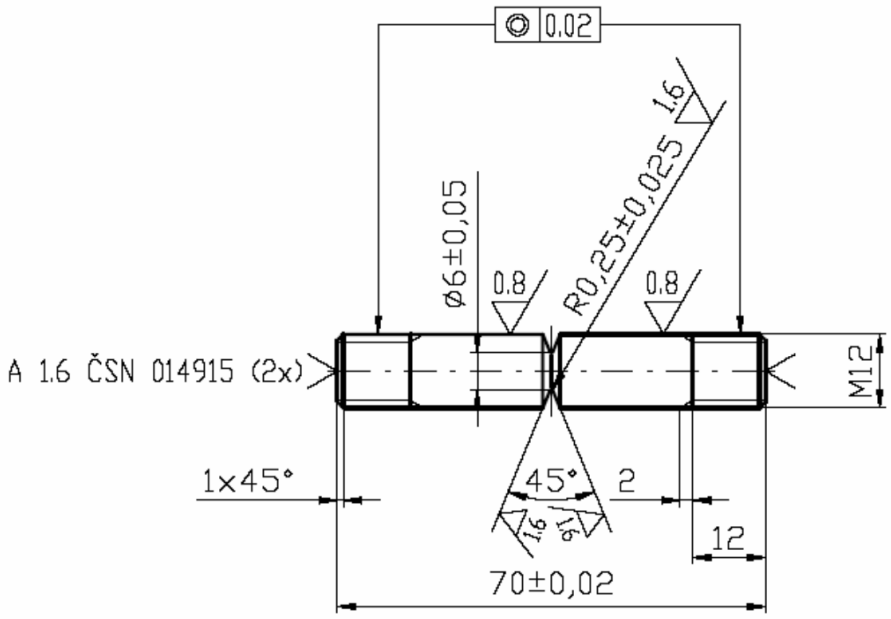

Fig. 34 The geometry of test specimen used for the tensile test of notched bars.

The initial diameter D_0 at the narrowest location of the notch was measured before the test. Tests were conducted at a loading rate of 2 mm/min in a cryogenic chamber on the test machine Zwick 1382. The temperature was measured by a thermocouple fixed to the surface of the test bar. The diameter in the neck d_u and the distance of the lines L_u were measured after the test. This type of testing is not standardized; nevertheless, the general guidelines specified by standards for tests on smooth bars were followed. Additionally, the nominal fracture stress R_u was determined from a load at fracture F_u and corresponding cross sectional area S_u in the narrowest location of the bar.

$$R_u = \frac{F_u}{S_u}. \tag{70}$$

The total elongation A^* was determined for the unstable fracture of the notched bar:

$$A^* = \frac{L_u - L_0}{L_o}.100, \tag{71}$$

where L_0 and L_u are specimen gauge lengths, the initial one and at fracture, respectively.

Additionally, the total reduction of area at the narrowest location (necking area) on the bar Z^* was obtained by using equation:

$$Z^* = \frac{S_0 - S_u}{S_0}.100. \tag{72}$$

4.4 Neural Network Application

The purpose of the research has been to develop quantitative model for the prediction of reference temperature using experimental data collected from the tensile test, together with a powerful computational technique known as neural network. Creating a truly general model required a combination of available data and metallurgical knowledge.

General tool/software developed for adequate purposes by [82] was used for the ANN development, i.e. for the data set evaluation, ANN training step and verification stage. The software has a set of separate functions that are controlled through model manager so different alternatives and parameters are available for the ANN settings.

Model Manager provides a graphical interface to David MacKays [82] big back program, used extensively in the Phase Transformations and Complex Properties group at the University of Cambridge. Model Manager implements a system following the work of MacKay, who applied neural networks models in a Bayesian framework. Model Manager also incorporates further practical methods which further contribute to the successful completion of modelling. The database is randomly divided into training and testing sets, to ensure that both the half used for training and testing contains similar information.

Model Manager enables to form final model. This final model is built from a committee of multiple submodels. The optimum number of submodels to form the committee is determined depending on the combined test error of all the members of the committee. These methods are further attempts to find the appropriate level of complexity from the data, and to ensure a robust solution is found. The used approach has been applied previously in solutions of materials science problems [79, 80, 86].

The applied three layer feed-forward neural network has been characterised in chapter 2.6.2. In the ANN the data moves in only from the input nodes, through the hidden nodes and to the output node. Numerical inputs from smooth tensile test specimen and notched tensile test specimen and hardness measurement have been available from 29 data sets of different steels according to Table 6. The upper layer contained the output neuron, whose activity represents the output quantity - the reference temperature T_0 of the fracture toughness temperature dependence.

There were tested four models differing by the selection of parameters on the input side:

- The first model used the hardness value as an input variable, but did not include the temperature value as an input variable; all parameters of the tensile test and hardness value were used as input variables.
- The second model used all parameters of tensile test that were measured only at room temperature. This model also included hardness values and temperature as input variables.
- The third model used all parameters at both temperature (purely general yield temperature and purely ductile fracture temperature) excluding hardness values and temperature.
- The fourth model used all parameters of the tensile test at both temperatures as input variables. In this model, temperature was added as an input variable but hardness was in excluded.

Table 6 shows one example of the data set available for one steel (α iron - steel A). Similar data tables have been available for all 29 steels tested containing material of various origins see the Table 5 in chapter 4.1.2 [89]. Four or five tensile specimens were tested for each steel. For example for steel A, three specimens were tested at room temperature and two specimens were tested at general yield temperature. So the averaged values of the tensile test have been used for the ANN development.

For completing training without overfitting, the reference temperature model prepares the database before training as follows:

- The database is randomly divided into training and testing sets to ensure that data used for training and testing contains similar information.
- The minimum and maximum of each variable and the target are searched.
- The inputs are normalized within a range of ± 0.5 as follows:

$$x_i = \frac{x - x_{min}}{x_{max} - x_{min}} - 0.5, \tag{73}$$

where x is the unnormalised input, x_{min} and x_{max} are the minimum and maximum values in the database for a particular input, and x_i is the normalized value. The aim of normalizing is to compare the sensitivity of the prediction results for different inputs without biasing the comparison because of the different magnitudes of the set of inputs [96].

Table 6 The average values of tensile test for steel A (Fe).

The input variables		Units	Room temperature	General yield temperature
Temperature	T	$[K]$	295	173
Hardness	HV10	$[HV]$	90.3	-
Yield strength	R_e	$[MPa]$	194	401
Ultimate stress	R_m	$[MPa]$	309	440
Elongation	A_5	[%]	40.8	42.8
True stress at plastic instability	σ_m	$[MPa]$	386	563
True strain at plastic instability	ε_{pn}	$[-]$	0.221	0.222
Fracture stress uncorrected	σ_u	$[MPa]$	889	1004
Fracture deformation	ε_u	$[-]$	1.577	1.428
Fracture stress corrected	σ_{uB}	$[MPa]$	707	806
Slope	$\tan\alpha$	$[-]$	370	374

The weight estimates are made of the uncertainty of the submodel fit. The fitting method infers a probability distribution for the weights from the data presented instead of identifying one best set of weights. The performance of different submodels is the best evaluated using the log predictive error (LPE) instead of the test error [97]. The LPE is calculated as follows:

$$LPE = \frac{1}{2}\sum_{k}\left[\frac{(t^k - y^k)^2}{\left(\sigma_y^k\right)^2} + log\left(2\pi\left(\sigma_y^k\right)^2\right)\right], \tag{74}$$

where σ_y^k is related to the uncertainty of fitting for the set of inputs x^k. This error penalizes unexpected predictions to a lesser extent when they have large error bars (uncertainties). The test error does not have this advantage.

5 RESULTS

Eight sets of specimens cut from the dissimilar weld joint were tested in the transition region in order to determine the fracture toughness. As a result, the reference temperature was obtained.

5.1 Fracture Toughness of Weld Joints (as Received and Aged)

The specimens of base material C20 without thermal ageing showed a very high scatter of fracture toughness behaviour in the transition region (see Fig. 35). The master curve concept describes well the large database of RPV steel, where the master curve methodology has been developed for low alloy steels. It includes data from 72 $\mathrm{MPam}^{1/2}$, at -30 ℃ up to 213 $\mathrm{MPam}^{1/2}$ for 0 ℃. These data show that both the upper bound and lower bound of fracture toughness scatter band increases with increasing the test temperature, as a result of the transition behaviour. Relating to master curve concept the 5 and 95% probability scatter band represents well experimental data. Note the reference temperature is showed by blue dashed line in Fig. 35.

Table 7 Base material C20 in as received conditions

Specimen	t [℃]	a_0 [mm]	F_Q [kN]	F_c [kN]	F_c/F_Q [-]	U_{pl} [J]	U_{el} [J]	K_{Ic} , K_e [MPa. $\mathrm{m}^{0.5}$]	K_{JC} [MPa. $\mathrm{m}^{0.5}$]
C20-108	0	26.30	32.88	42.11	1.28	44.9	34.51	79.0	213.6
C20-405	-30	26.44	33.33	38.42	1.15	5.11	12.63	72.8	99.0
C20-214	-30	26.45	31.82	38.26	1.20	6.61	12.95	72.5	105.3
C20-101	-20	26.43	33.29	39.85	1.20	15.93	19.06	75.5	140.5
C20-115	-40	26.30	37.63	37.63	1	0	11.77	70.8	-
C20-401	-40	26.49	36.51	36.51	1	0	10.56	69.4	-
C20-105	-30	26.46	31.53	39.49	1.25	7.62	14.33	74.9	111.1

Table 7 shows that only two specimens (of the base material without thermal ageing) have linear elastic behaviour, because the ratio F_c/F_Q is less than 1.1, according to the condition given in Eq. 45. The critical stress intensity factor is calculated directly as K_Q in

accordance with Eq. 41. The rest of the specimens displayed elastic-plastic behaviour, where the values of *J*-integral at cleavage instability J_c, were converted to their equivalents in terms of stress intensity factor K_{Jc} as given in Eq. 49.

Similar observations was recognised for the base material after thermal ageing, see the Fig. 36 to 38. In addition, these figures illustrate fracture behaviour of the base material C20 for different delays at thermal ageing temperature of 450 °C (from 500 to 1000 hrs). Note also, that all experimental data obtained are lying within 5 and 95% probability scatter band calculated for the obtained reference temperature. This shows good susceptibility of the master curve concept for transition behaviour prediction for this particular steel. Almost all fracture toughness values represent elastic-plastic behaviour (K_{Jc}). This behaviour reflects well the resistance of the steel C20 against embrittlement caused by thermal ageing. It is also evident that for the fracture toughness data shown in Figs. 35 to 38 nearly the same reference temperature has been reached independently of thermal ageing time.

Figs 39 to 42 shows temperature dependences of fracture toughness for the region very near to fusion line in as received condition and after ageing at 450 °C. Comparing to base material we can observe that the transition is occurring at lower temperatures and, in addition it appears very steep. This behaviour is caused by very large scatter of the data observable at one temperature as it is evident mainly for states after thermal ageing (Figs. 40, 41 and 42 respectively). The scatter of data is caused by very different fracture behaviour, in the upper part corresponding to elastic-plastic performance of the material, in the lower part, corresponding more to very brittle behaviour and fracture without any preceding plastic deformation, see the data at -30°C in Fig. 40 for material after thermal ageing for 500 hrs. The same material fracture performance is observable also for longer ageing times, as it is seen for data at -30°C in Fig. 41 and data at -40 °C in Fig. 42.

Figs. 40 to 42 also illustrate the temperature dependences of the transition fracture toughness data in transition region relative to their master curves including 5 and 95% tolerance bounds. While 5 and 95% tolerance bounds provide a reasonable description of the transition fracture toughness data, there were some outliers in each data set. All corresponds to linear elastic fracture toughness, i.e they were calculated directly in order to obtain the stress intensity factor K_Q using Eq. 41. The other J_C values were converted to their stress-intensity factor equivalent using Eq. 49 (elastic-plastic fracture toughness data K_{JC}).

As example, Table 8 shows that five specimens have linear elastic behaviour, because the ratio F_c/F_Q is less than 1.1. In addition, plastic deformation U_{Pl} is equal to zero for these

samples. The other specimens behaved in an elastic-plastic manner, where the values of the *J*-integral at cleavage instability, J_C, were converted to their equivalent values in terms of stress intensity factor K_{Jc}.

Table 8 Steel C20 from fusion line region near weld joint after ageing at 450 ℃ for 700 hours

Specimen	t [℃]	a_0 [mm]	F_Q [kN]	F_c [kN]	F_c/F_Q [-]	U_{pl} [J]	U_{el} [J]	K_{Ic} , K_e [MPa. $m^{0.5}$]	K_{JC} [MPa. $m^{0.5}$]
W7-111	-30	26.91	38.78	42.36	1.09	0	15.28	82.79	-
W7-305	-30	26.07	44.41	66.41	1.5	91.57	76.97	122.88	307.69
W7-207	-30	26.15	26.09	26.09	1	0	4.57	48.51	-
W7-212	-40	25.75	33.9	33.9	1	0	7.72	61.56	-
W7-307	-30	25.95	37.8	37.8	1	0	10.55	69.5	-
W7-303	-20	25.93	35.29	35.29	1	0	10.21	64.8	-
W7-105	-30	26.6	44.49	53.34	1.2	19.05	33.13	102.35	165.61
W7-115	-20	26.09	38.99	52.24	1.34	13.52	27.2	96.95	145.53

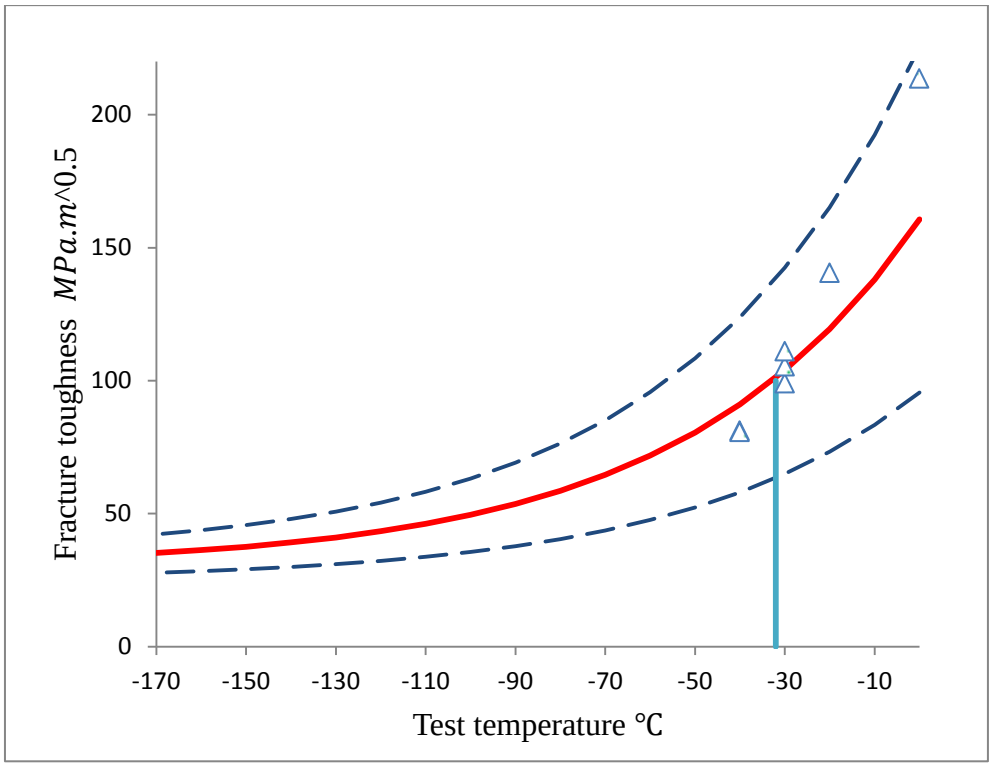

Fig. 35 Experimental data, master curve and 90% probability scatter band obtained using base material C20 without thermal ageing.

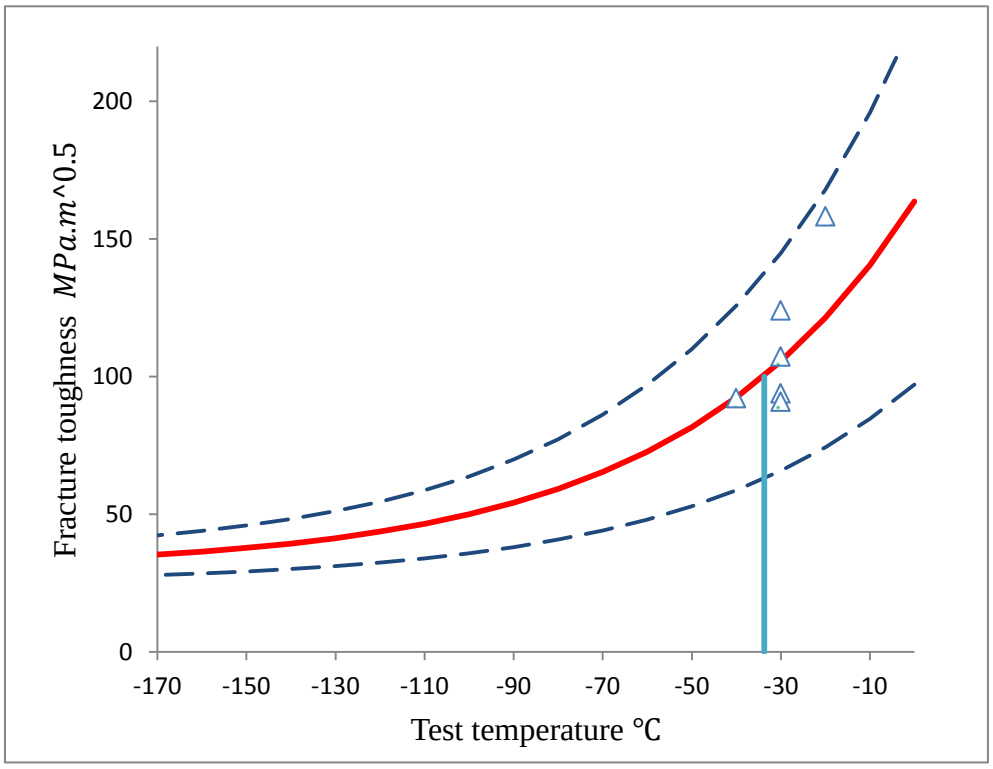

Fig. 36 Experimental data, master curve and 90% probability scatter band obtained using base material C20 after thermal ageing at 450 ℃ for 500 hours.

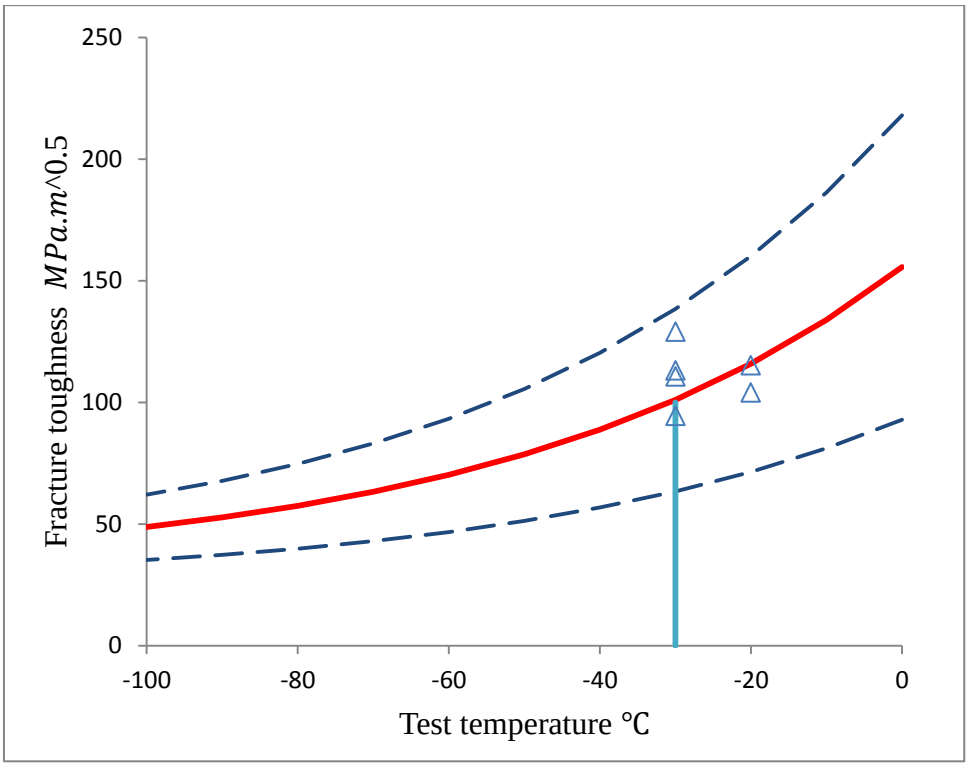

Fig. 37 Experimental data, master curve and 90% probability scatter band obtained using base material C20 after thermal ageing at 450 ℃ for 700 hours.

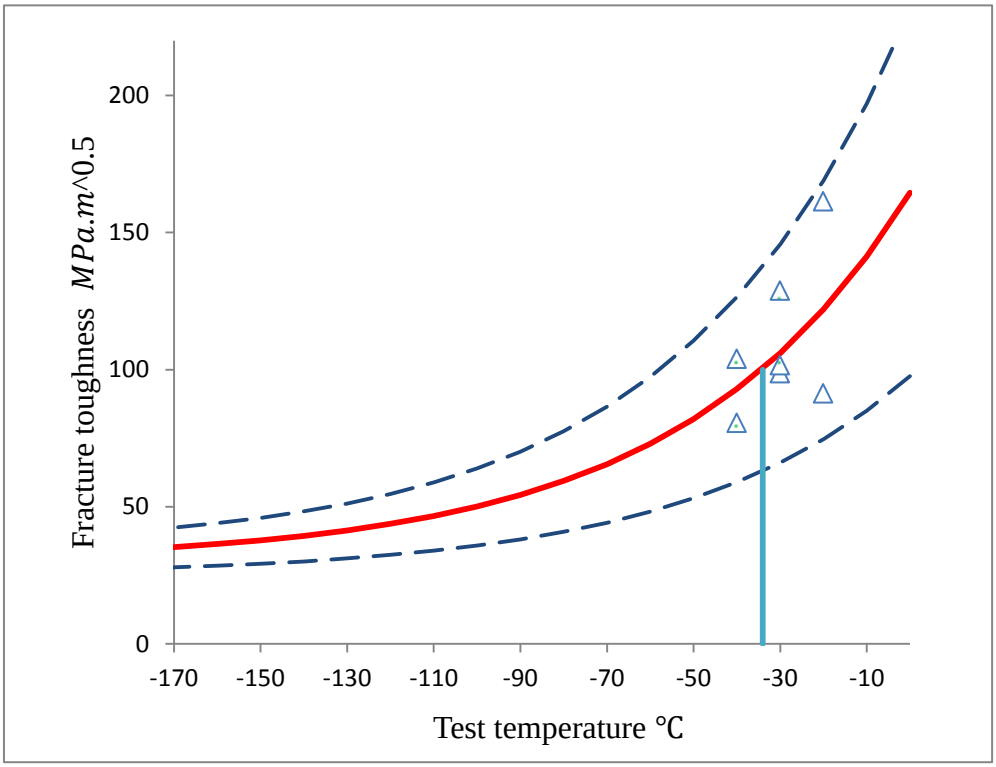

Fig. 38 Experimental data, master curve and 90% probability scatter band obtained using base material C20 after thermal ageing at 450 ℃ for 1000 hours.

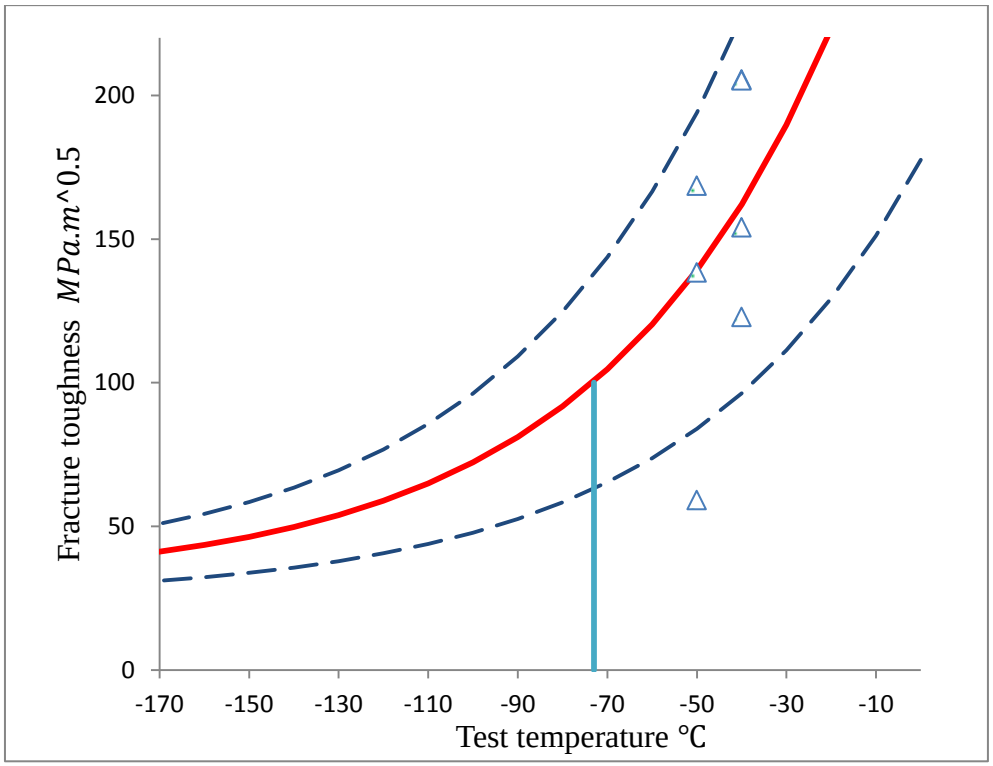

Fig. 39 Experimental data, master curve and 90% probability scatter band obtained for transition region W7 without thermal ageing.

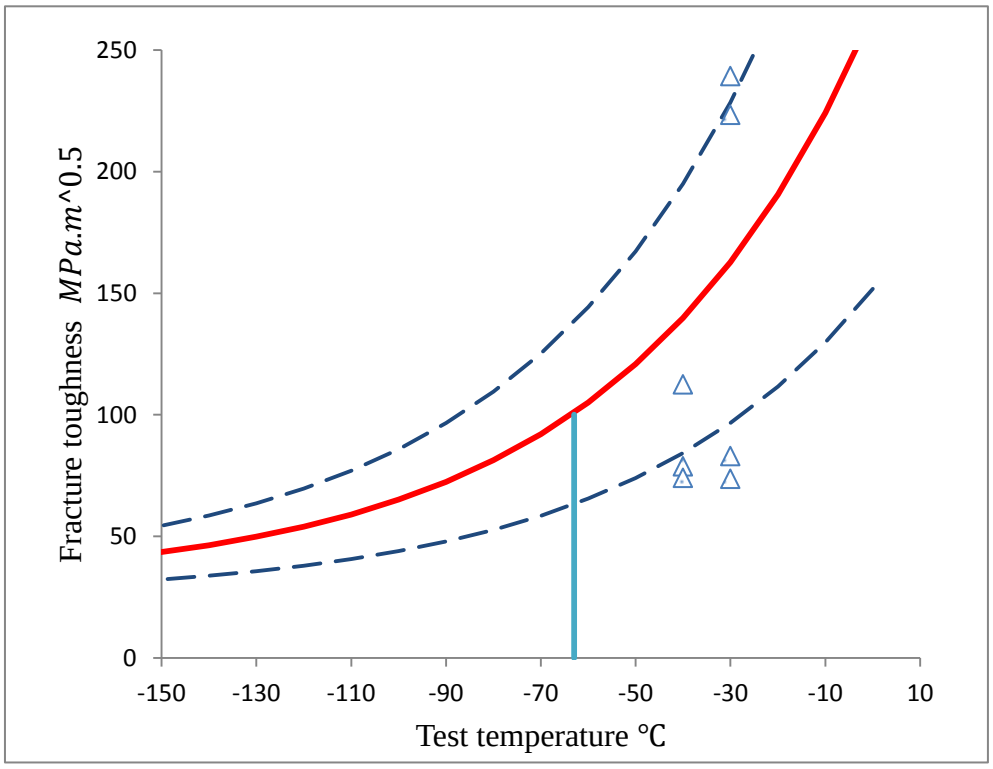

Fig. 40 Experimental data, master curve and 90% probability scatter band obtained for transition region W7 after thermal ageing at 450 ℃ for 500 hours.

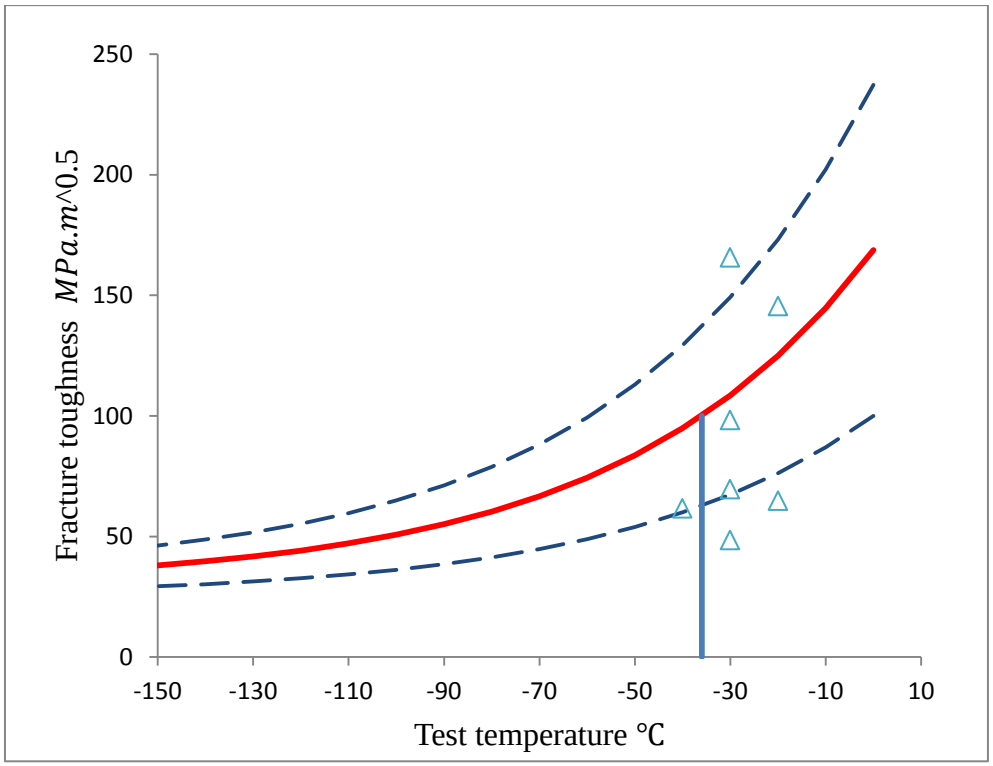

Fig. 41 Experimental data, master curve and 90% probability scatter band obtained for transition region W7 after thermal ageing at 450 ℃ for 700 hours.

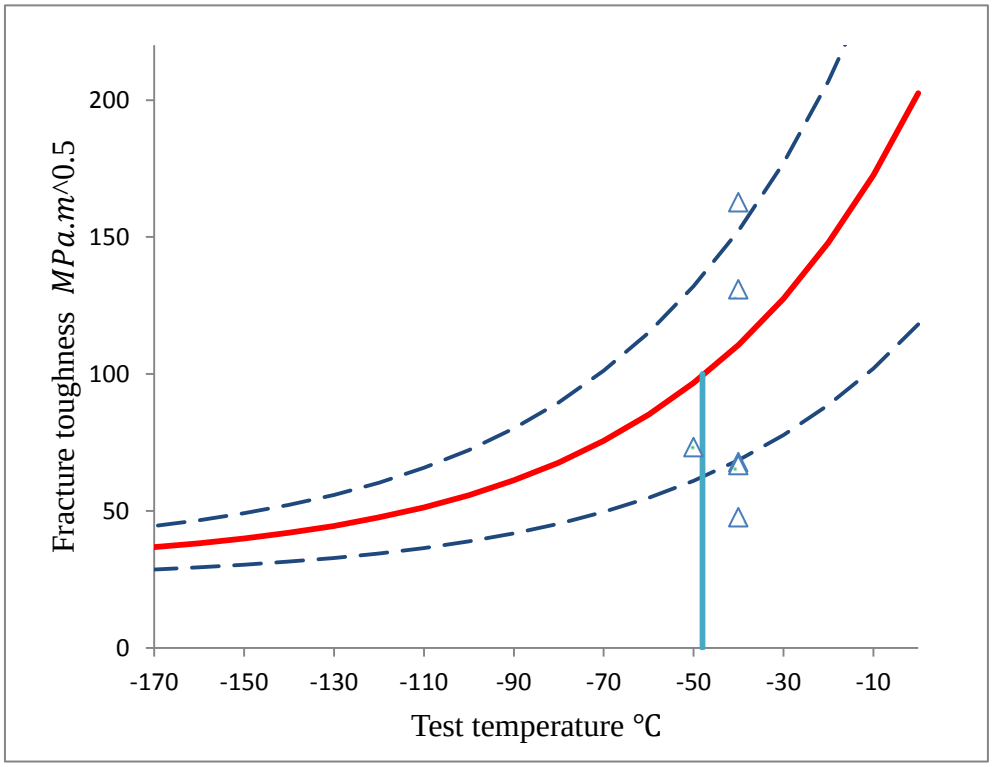

Fig. 42 Experimental data, master curve and 90% probability scatter band obtained for transition region W7 after thermal ageing at 450 ℃ for 1000 hours.

The reference temperatures T_0 for the base steel C20 and location very near to fusion line with overlay, both in as received condition and after thermal ageing, are summarised in Table 9.

Table 9 Summary of reference temperatures T_0 obtained experimentally for the investigated materials

	as received state	**450°C/500 hrs**	**450°C/700 hrs**	**450°C/1000 hrs**
steel C20	-32.9	-34	-30.8	-34.4
near fusion line	-73.5	-63.7	-36	-47.5

Fig. 43 shows comparison of reference temperatures obtained for as received materials and materials obtained by thermal ageing at 450°C for 500, 750 and 1000 hrs respectively, namely for the base steel C20 and material very near to fusion line. There are evident differences in the materials performance for these two locations.

The base material, steel C20, shows no changes with the thermal ageing, the reference temperature is lying very near to -30°C. This means very good evaluation for this material showing very stable microstructure as well as resistance to carbide precipitation reactions and good metallurgical quality. In addition, all fracture toughness data lying in 5 and 95% probability scatter band reflect the same fracture mechanism in all samples independently they revealed the fracture in elastic-plastic or linear elastic regime.

The material very near to fusion line is affected by diffusional processes running during fusion welding and later during thermal ageing. As a consequence even if it is initially the same steel (C20) after these changes it is becoming into another composition and microstructural state. Due to these changes the experimentally determined reference temperature for this location is lower (less than -70 °C) comparing to the base material and it is still keeping this low value for the thermal ageing for 500 hrs, but for longer ageing times T_0 is rapidly increasing. These changes reflect very well material embrittlement due to long term diffusion processes of carbon and alloying elements leading to carbide coarsening.

Fig. 44 and 45 show comparison of all experimentally determined fracture toughness values in dependence on difference between test temperature and reference temperature for both materials locations. This diagram is commonly taken as evidence of validity of the master curve concept for the given fracture toughness set. For the base material, see the

Fig. 44, all fracture toughness data are lying in the 5 and 95% probability scatter band showing good relevance of the master curve concept for evaluation and prediction of fracture toughness in transition region.

But this is not the case for the location near the fusion line, see the Fig. 45. There are systematically outlying fracture toughness data below the lower bond corresponding to 95 % fracture probability. Relating to master curve concept applicability, this finding does appear no serious problem, mainly because of experimental error associated with the low number of experimental data (the estimated experimental error of T_0 determination from 7 valid samples is about ±10 °C [24]). Almost all these data have been obtained after linear elastic history of loading, some of them are showing very low fracture toughness level being around and bellow 50 MPam$^{1/2}$. This may be associated with the change of the fracture mechanism disqualifying the data for the master curve concept, e.g. due to change of the weakest link behaviour to accumulation of damage sites fracture performance.

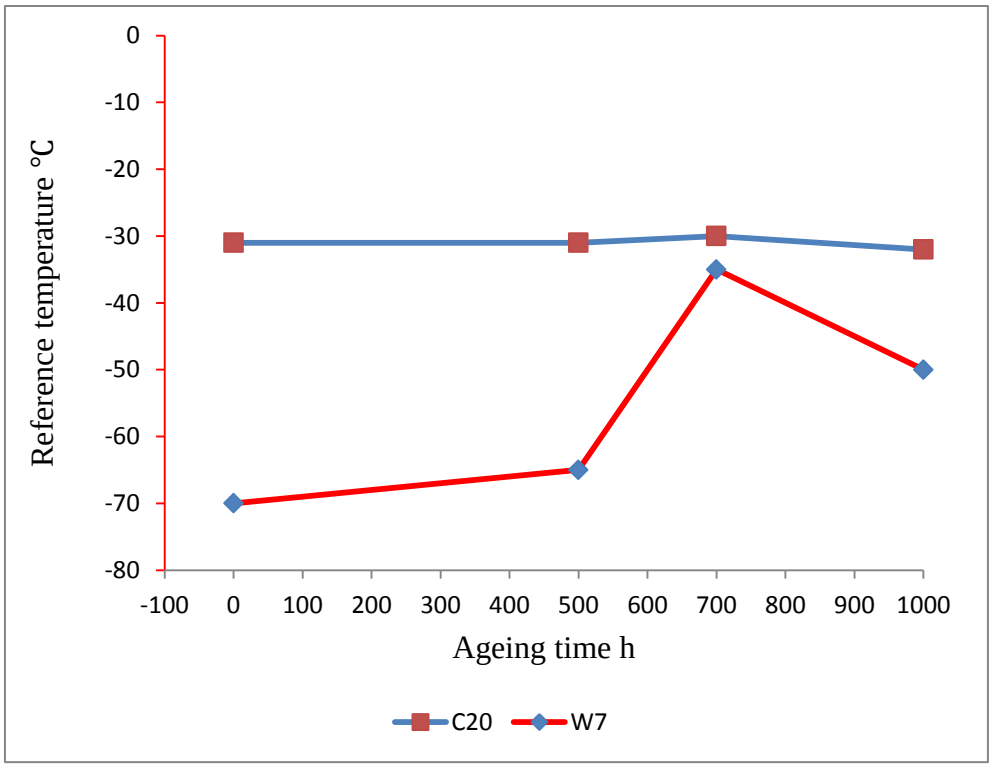

Fig. 43 Changes of reference temperature with simulated ageing.

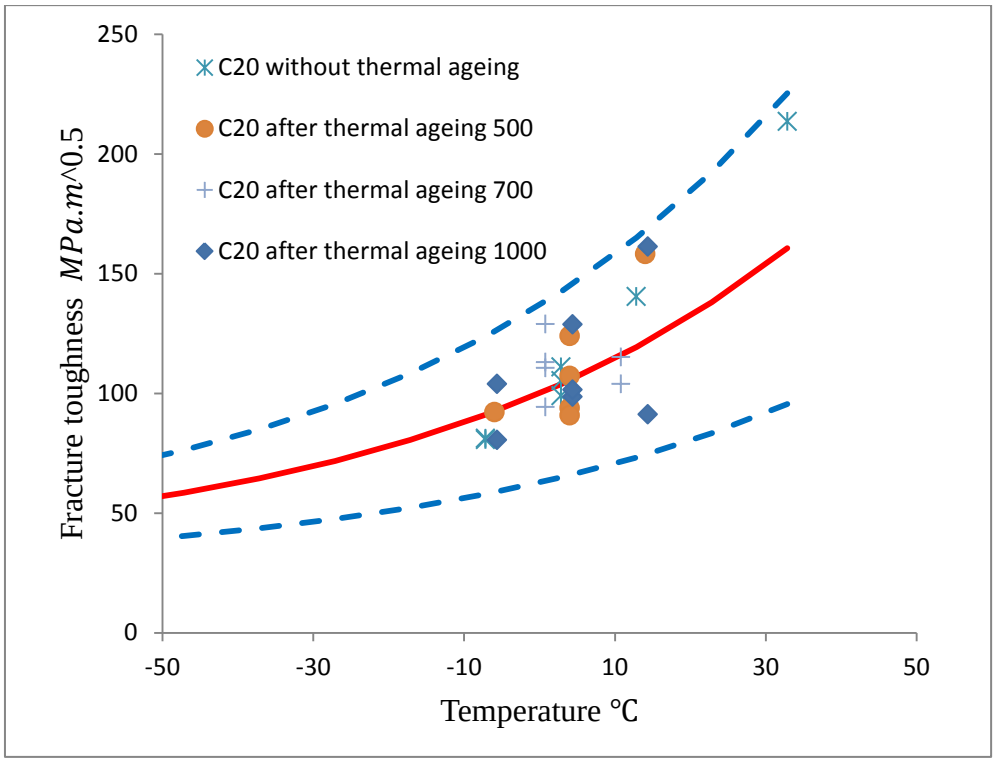

Fig. 44 Experimental data, master curve and 90% probability scatter band in dependence on difference between test temperature and reference temperature.

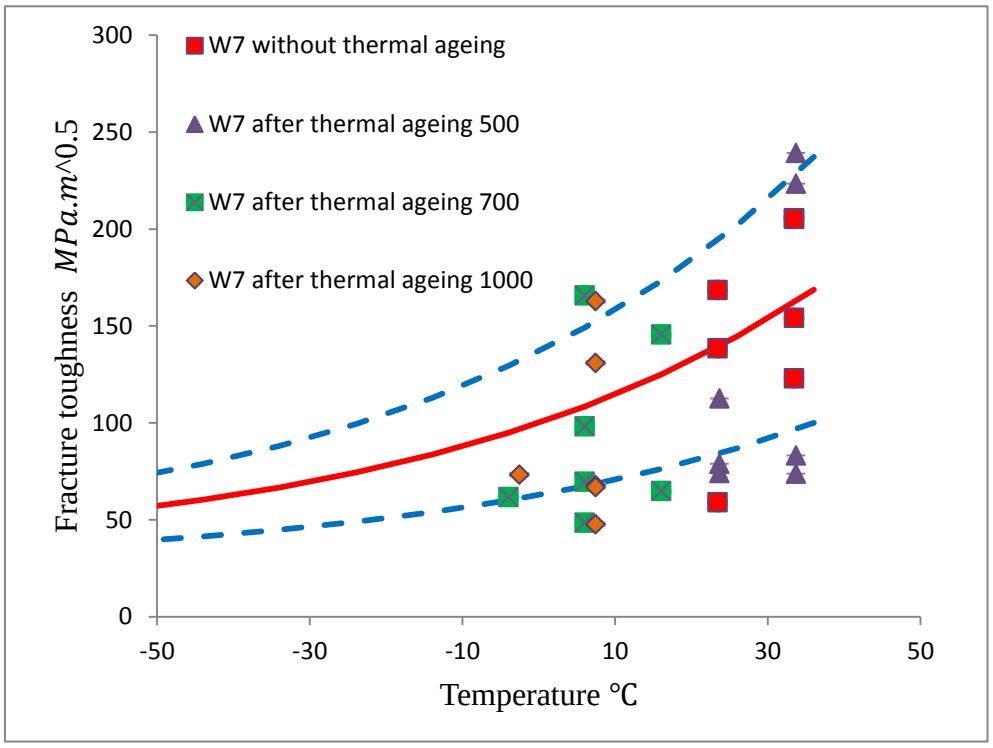

Fig. 45 Experimental data, master curve and 90% probability scatter band in dependence on difference between test temperature and reference temperature for fusion line region.

5.2 The Neural Network Results

Different sets of mechanical parameters have been tested on the input side of ANN. Each test set consisted of training stage including the data analysis (as shown for the first model) followed by prediction of reference temperature. As mentioned 29 data sets from low alloy steels were applied in the experimental tests to validate the models of reference temperature prediction. For purpose of the theses, four models of the reference temperature with different parameters of input are characterised in this section. These four ANN models have been developed for parameters combinations shown in Table 10.

Table 10 The models of the reference temperature with different parameters on input.

	Tensile data at r.t.	Tensile data at T_{gy}	Hardness HV10	Value of Room temperature [K]
First model	**x**		**x**	
Second model	**x**		**x**	**x**
Third model	**x**	**x**		
Fourth model	**x**		**x**	

5.2.1 The First Model

The first model used the hardness HV10 value as an input variable, but did not included the temperature value as an input variable. In addition all parameters of the tensile test at room temperature were used as input variables. The minimum and maximum of each variable and the target data are shown in Table 11.

Parameters applied and results obtained are characterized for the first model in more detail. When the data are uniformly distributed, it minimizes the uncertainties for interpolation and extrapolation, thus such data are providing a better model. Table 12 shows the input parameters used to develop the reference temperature model. Most of the parameters thought to affect the reference temperature are included: temperature, hardness, yield strength, ultimate stress, elongation, true stress at ultimate tensile stress, true strain at ultimate tensile stress, fracture stress uncorrected, fracture deformation, fracture stress corrected, slope. Fig. 46 illustrates the data distribution for different input variables that are used to develop the model. It is intended only to show the distribution of the data without correlation between the different variables. All variables are not clustered, they are

homogeneously distributed. Nonetheless, the Bayesian framework of the ANN recognizes this by associating large modelling uncertainties with sparse or noisy domains.

The Bayesian method can find the significance of each input, thus there is no need to exclude any variable prior to the analysis. The variables which have little effect in explaining the output will be linked to small weights.

After analysing and preparing the database, many submodels have been developed. Each submodel contained a set of parameters which defined the function that best fits the data with which the submodel has been developed. The neural network captured interactions between the parameters. Each submodel had a given number of hidden units, thus different results were obtained by the particular submodel. Nevertheless, such submodels sometimes had domains in which they displayed good prediction, and others in which they did not. It is important to mention that a set of submodels with a given numbers of hidden units and different seed is called a model or a committee of multiple submodels. Their predictions are combined to give the best overall result possible. Seeds are the initial weights which have been used as guesses. In the training phase, one hundred networks were trained with hidden units ranging from one to twenty and five seeds in each case. Each submodel made a prediction differently and these submodels were sorted according to the log predictive error (LPE), the submodel with the highest log predictive error is the best one (Fig. 47).

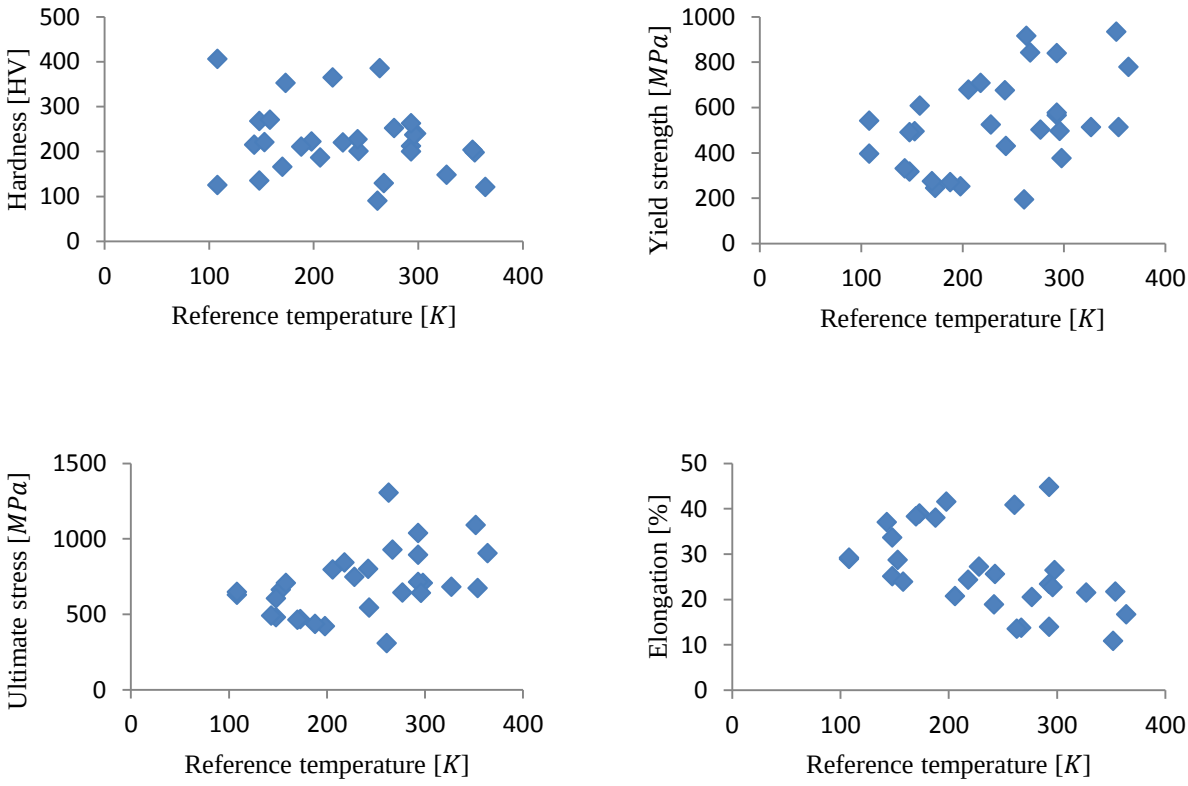

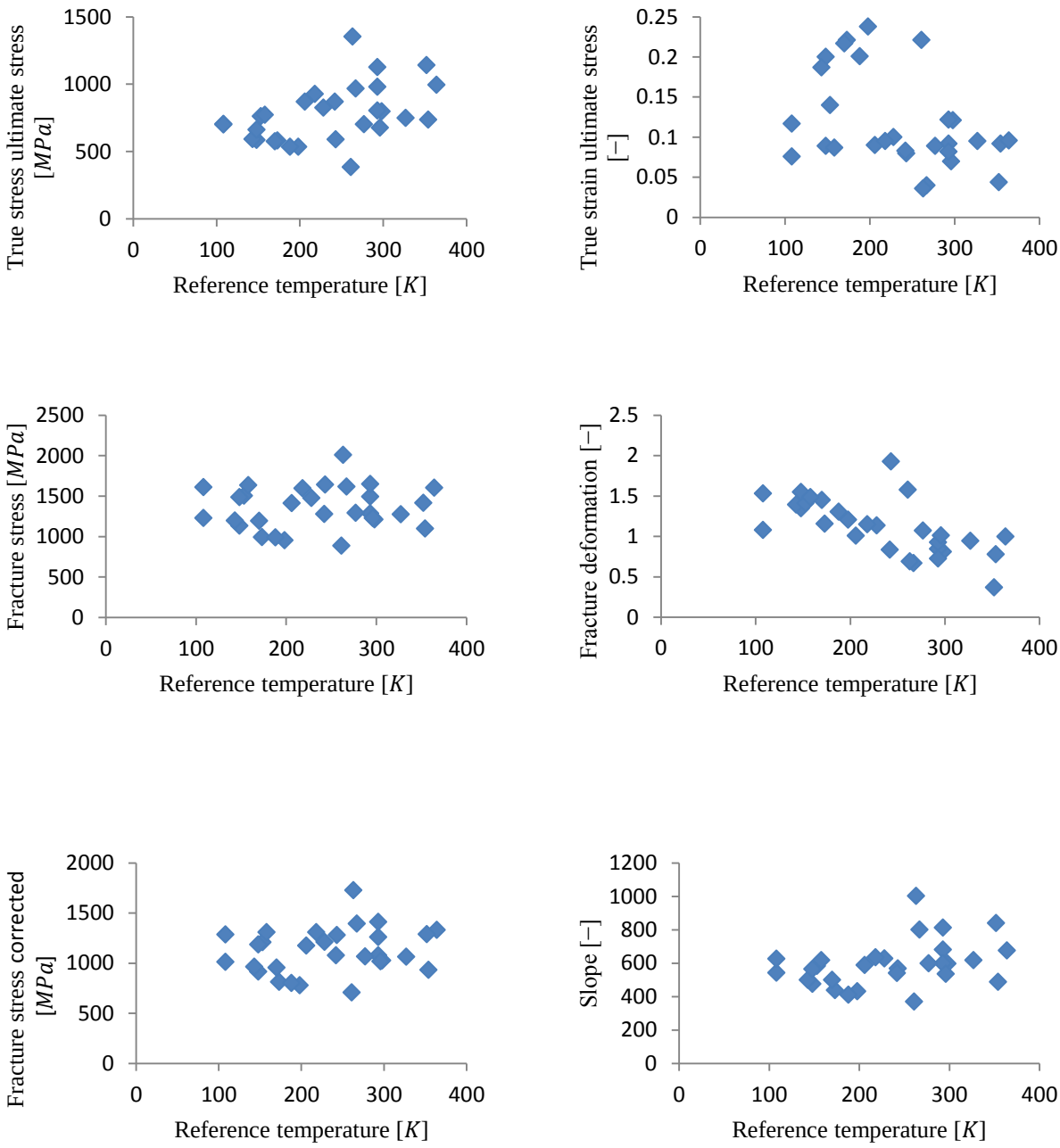

Fig. 46 Visual illustration of the distribution of data used to create the model.

The time required to train a submodel grows exponentially with the number of hidden units (typically, training a submodel with one hidden unit took a few seconds, while many hours were required for 20 hidden units).

Fig. 47 shows the changing of LPE with the number of hidden units. The LPE has an optimum value at about one hidden unit (the red point in Fig. 47), as the test error has a minimum value at about one hidden unit (the red point in Fig. 48)

The submodel with a given number of hidden units and different seed made predictions differently (see the annex Table 18). The best submodel according to the LPE was then selected and tested on the output side for accordance with experimentally determined reference temperature.

Table 11 The minimum and maximum values for the first database

Inputs	Min	Max	MinNo	MaxNo	Average	StDev
Hardness	90.2	406	1	20	223	78.0691
Yield strength	194	934	1	24	527	206.6631
Ultimate tensile stress	309	1306	1	29	699	220.271
Elongation	10.81	44.8	24	11	26.6	9.2857
True stress at ultimate stress	386	1353	1	29	776.4	211.3358
True strain at ultimate stress	0.036	0.238	29	3	0.118	0.0589
Fracture stress	889	2011	1	29	1359.103	260.4535
Fracture deformation	0.369	1.929	24	14	1.118	0.3433
Fracture stress corrected	707	1727	1	29	1122.9	225.226
Slope	370	1002	1	29	595.2	136.8604
Reference temperature	108	364	20	18	233.4	74.7298

The database was randomly divided into training and testing sets to ensure that the data used for training and testing contains similar information. The Model Manager makes predictions using the whole database, comparing them with the actual target values. It divides the results into a training set and testing set as illustrated in Fig. 49 here in normalized variables, the result of the testing set is worse because it is unseen data. These procedures have been done during the training phase.

The final ANN model has been built from a committee of multiple submodels. The optimum number of submodels to form the committee is determined depending on the combined test error of all the members of the committee. These methods were further attempts to find the appropriate level of complexity from the data, and to ensure a robust solution is found.

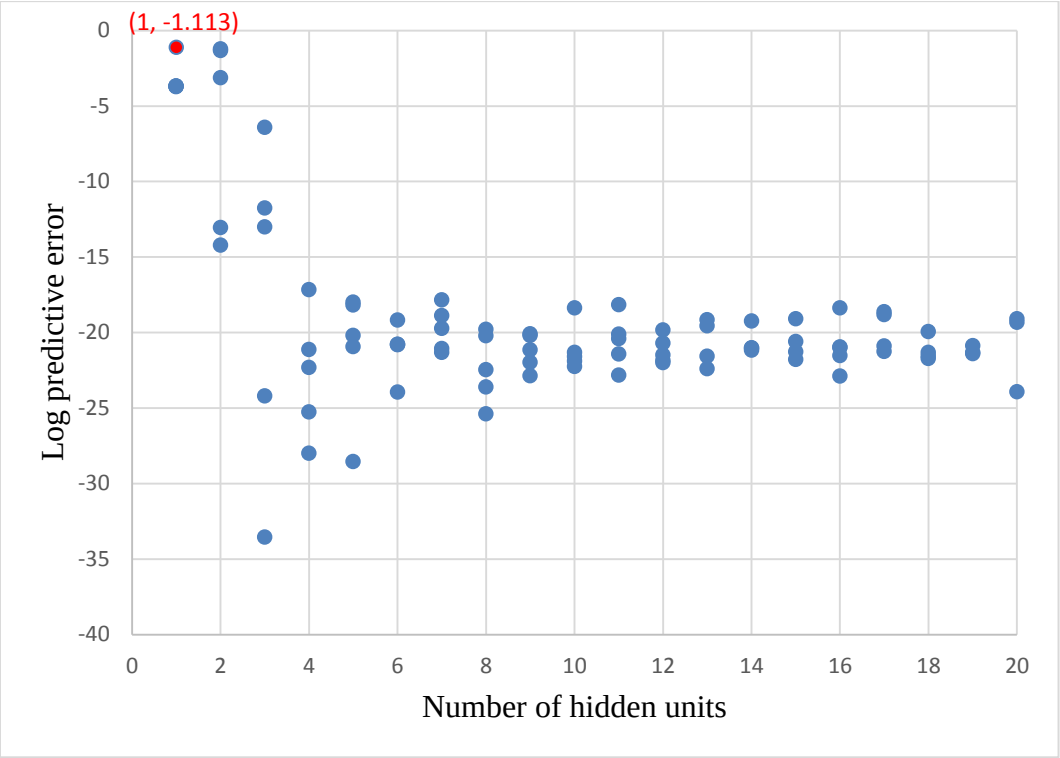

Fig. 47 The log predictive error during the training phase in dependence on the number of hidden units.

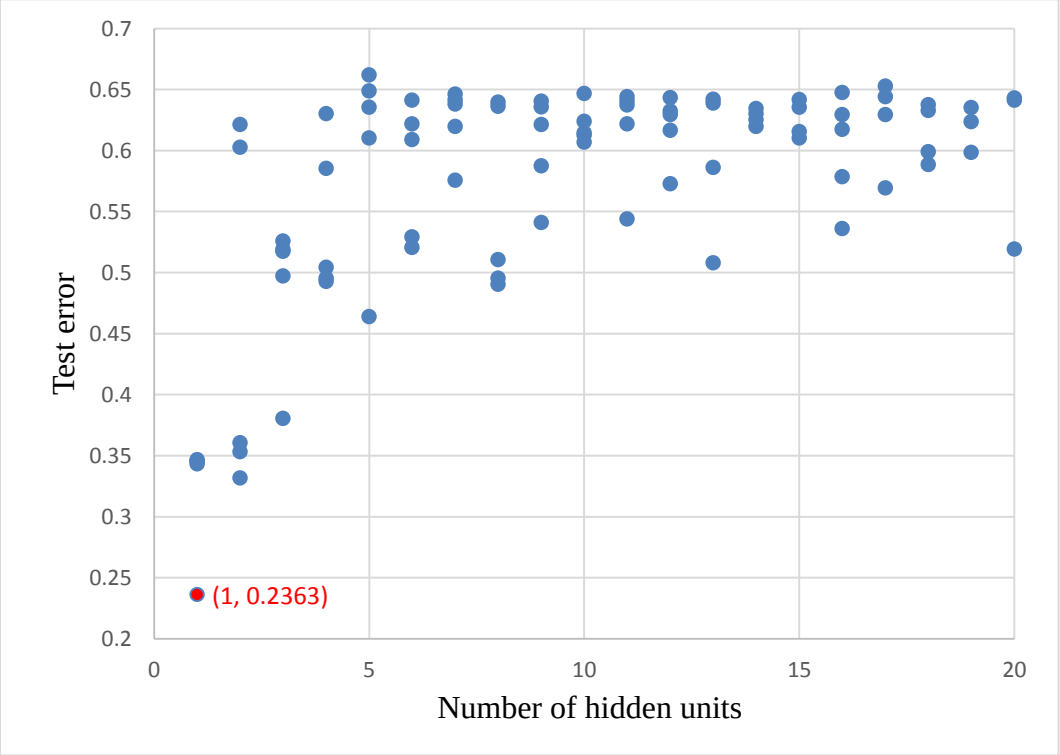

Fig. 48 The test error during the training phase in dependence on the number of hidden units.

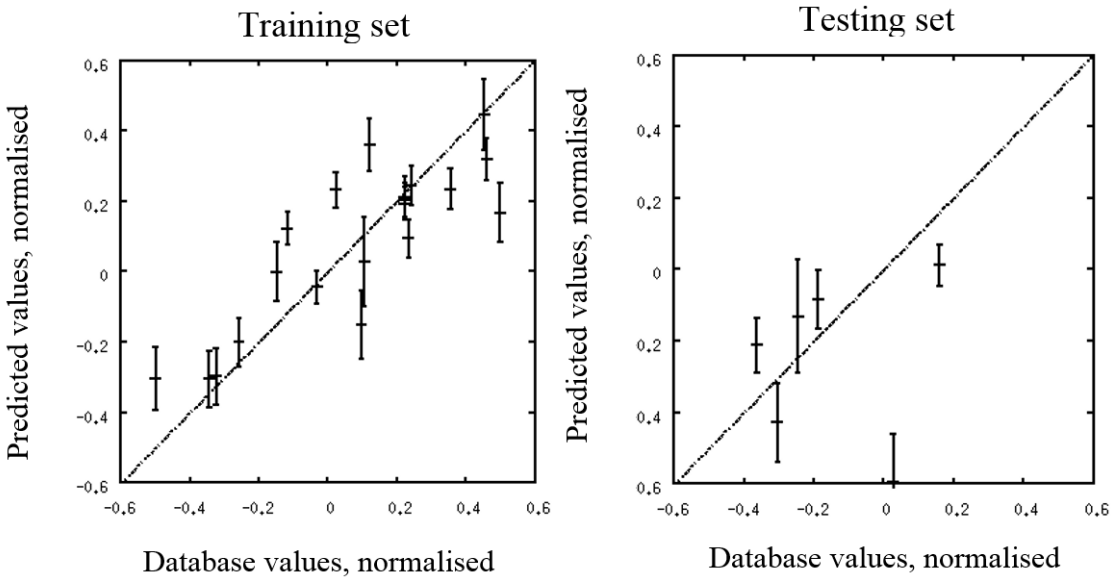

Fig. 49 Predictions by the submodel corresponding to three hidden units: a) Training set, b) Testing set.

The prediction or the output of a committee of submodels is the mean prediction of its members. For the committee, the uncertainty is given by equation:

$$\sigma^2 = \frac{1}{A}\sum_l \left(\sigma_y^l\right)^2 + \frac{1}{L}\sum_l (y^l - \bar{y})^2, \tag{75}$$

where $\bar{y}$ represents the mean prediction of submodels which form a committee, A is the number of submodels in the committee and the exponent l refers to the submodel used to give the corresponding prediction y^l. In the training phase, it is usual to compare the performance of an increasingly large committee on the testing set.

Usually, the error is minimized by using more than one submodel in the committee. However in our case, the optimum number of submodels to form the committee was found to be one as shown in Fig. 50 (the red point). Therefore the test error for the best submodel is 0.2363, and the combined test error of the committee is 0.2393; this is test error estimated just for committee containing only one submodel. It is important to note that the test error for the best submodel and the combined test error of the committee are the same.

To build a reliable model with an ANN structure, a few important points need to be followed. First of all, it is necessary to collect a data set containing variables which have a relevant effect on the output. For the data set used this aspect also means, that all the mechanical tests have been carried out with the same steel batch in the same state etc. Anything missing in the input variables means that there is additional noise in the model.

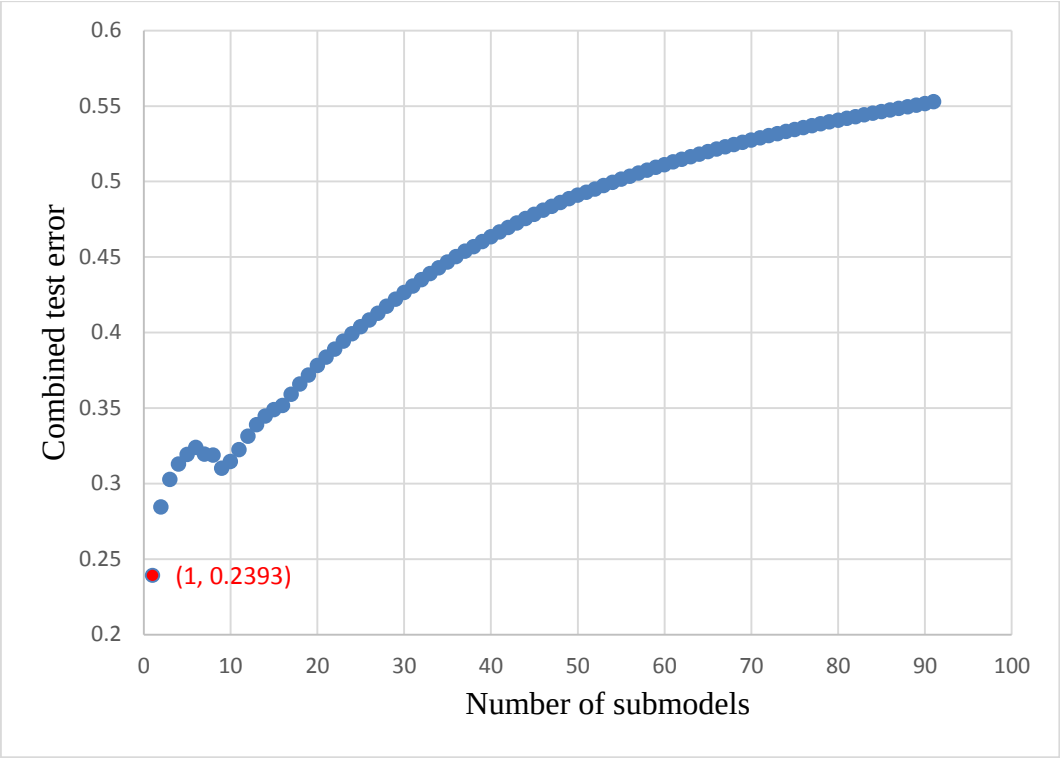

Fig. 50 The combined test error for the committees of different sizes.

When a neural network is used, it is important to distinguish between the two types of error. Noise means little changes in the results when the experiment is repeated a number of times due to uncontrolled variables. The noise is constant, so it does not contribute to the evaluation of the behaviour of the model. The second type of error is uncertainty, which refers to doubtfulness in the mathematical functions capable of representing the same data. Once more data are observed, the uncertainty can decrease, allowing the predictions made by the network to become more accurate. Modelled uncertainties are presented as error bars. The average of the error bars is calculated as follows:

$$E_{bar} = \frac{1}{N}\sum_{i=1}^{N} E_i \,, \tag{76}$$

where N represents the total number of predictions and E_i the error accompanying each prediction. The root mean square residual (RMS) was used to evaluate the final model and it was calculated as follows:

$$R_{test} = \sqrt{\frac{1}{N}\sum_{i=1}^{N}(t_i - y_i)^2} \,, \tag{77}$$

where t_i and y_i are the target value and network output respectively.

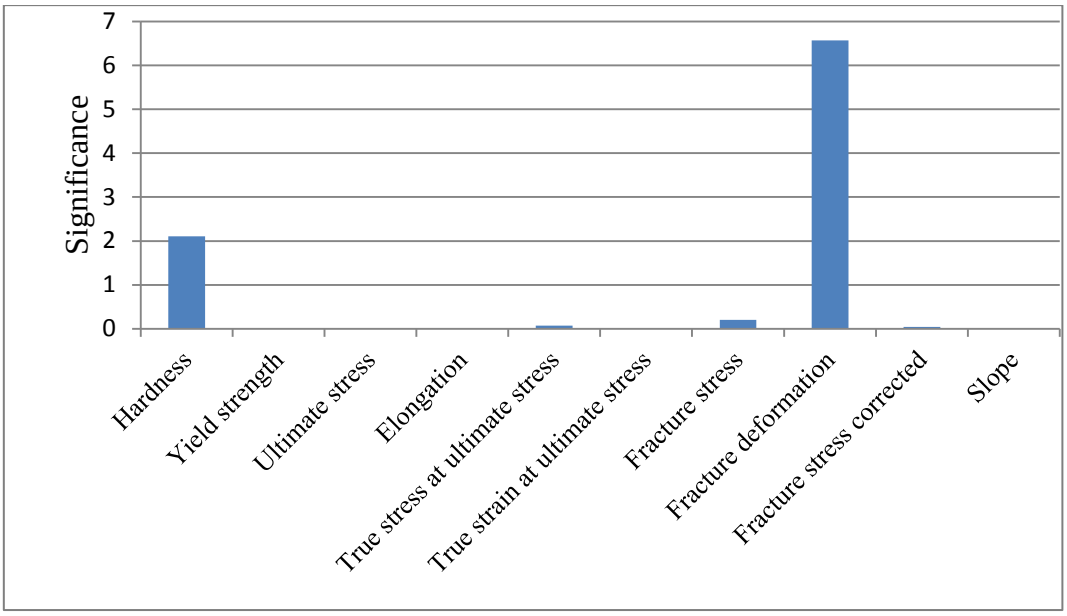

Fig. 51 Model perceived significance for the committee of submodels.

Table 12 The average values of inputs

Hardness	29.2828	[–]	True strain at ultimate stress	0.119	[–]
Yield strength	649.155	[MPa]	Fracture stress	1423.759	[MPa]
Ultimate stress	810.466	[MPa]	Fracture deformation	18.401	[–]
Elongation	25.313	[%]	Fracture stress	1197.724	[MPa]
True stress at ultimate stress	904	[MPa]	Slope	658.483	[–]

As mentioned previously, the Bayesian method can find the significance of each input, see Fig. 51. A high value of significance means that the input parameter concerned explains a relatively large amount of the variation in the output and it is not an indication of the sensitivity. To determine the significance of individual input parameters relating to the model, prediction processes must be made by changing one parameter only while keeping all the others constant. The network structure allows the assessment of input parameters to be included in the training data, and those parameters which have little effect on the output will have much lower significance than those with a greater effect. In this study, hardness and fracture deformation had the most significant effect, while other inputs were of low significance. In order to study the effect of each input on the behaviour of the model, each specific input was varied while all others were kept constant. The constant value for each input is shown in Table 12.

The reference temperature changes when the hardness varies while all other inputs are constant. Fig. 52 shows that the reference temperature decreases with an increase in the hardness from approximately 100 to 400. The error bars look almost constant, i.e. they come from noise from uncontrolled variables.

Fig. 53 shows the effect of yield strength on the reference temperature. The yield strength may not influence the reference temperature as the error bars look almost constant. Fig. 54 shows that the ultimate stress may also not affect the reference temperature. The reference temperature looks constant with an increase in the ultimate stress and the error bars look almost constant. In Fig. 55, the reference temperature is also constant as the elongation increases and the error bars are approximately constant. Fig. 56 illustrates that there is no change in error bars when the reference temperature slowly decreases while the true stress at ultimate tensile stress (plastic instability point) increases from 386 [MPa] to 1353 [MPa].

The reference temperature is constant (239.7494 [K]) as the true strain at ultimate stress increases from 0.036 to 0.238 (see Fig. 57), whereas the reference temperature decreases from 241.369 [K] to 237.498 [K] as the fracture stress increases from 889 [MPa] to 2011 [MPa] (see Fig. 58). The error bars start with a high error bar at about 889 [MPa] of fracture stress and then slowly decreasing to a minimum at about 1289 [MPa] of fracture stress and then increasing again up to 2011 [MPa] of fracture stress. In Fig. 59, the error bars change when the fracture deformation increases, with the minimum value of error bars at 0.769 of true fracture strain. The reference temperature decreases as the true fracture strain increases.

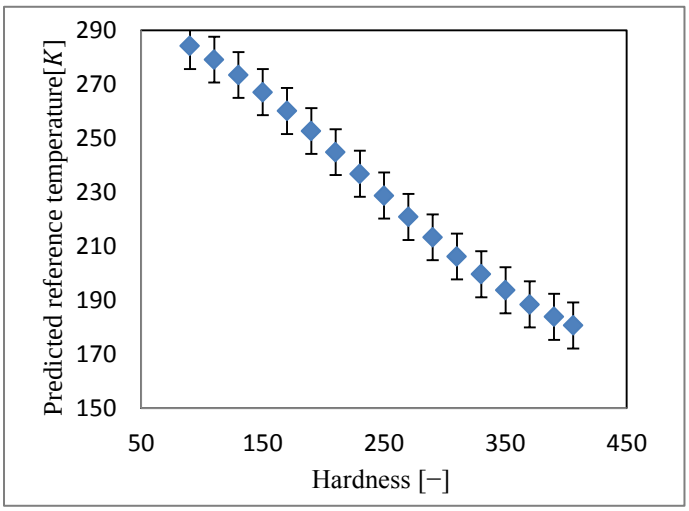

Fig. 52 Prediction of reference temperature in [K] against hardness HV10 [−] with error bars.

The reference temperature slowly decreases as the corrected fracture stress increases (see Fig. 60). The error bars are approximately constant. Fig. 61 illustrates that the error bars look almost constant. The reference temperature has constant value (239.749 [K]), as the slope increases from 370 to 1002.

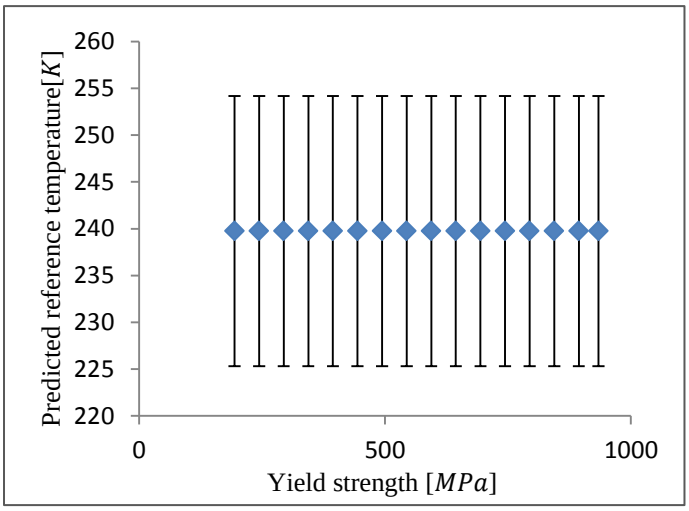

Fig. 53 Prediction of reference temperature in [K] against yield strength in [MPa] with error bars.

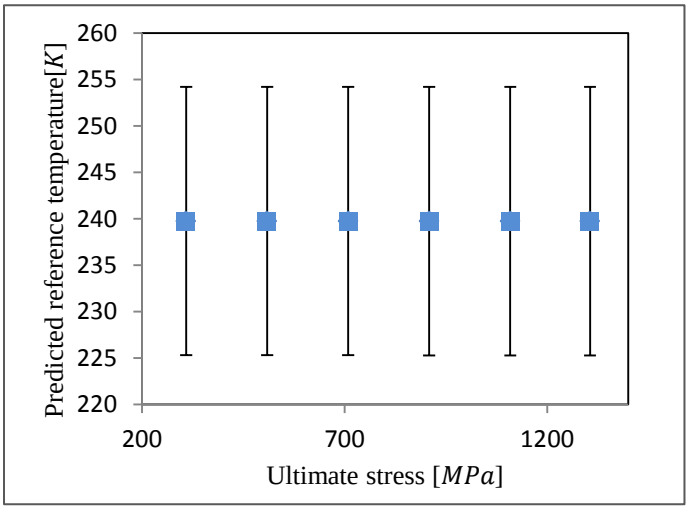

Fig. 54 Prediction of reference temperature in [K] against ultimate stress in [MPa] with error bars.

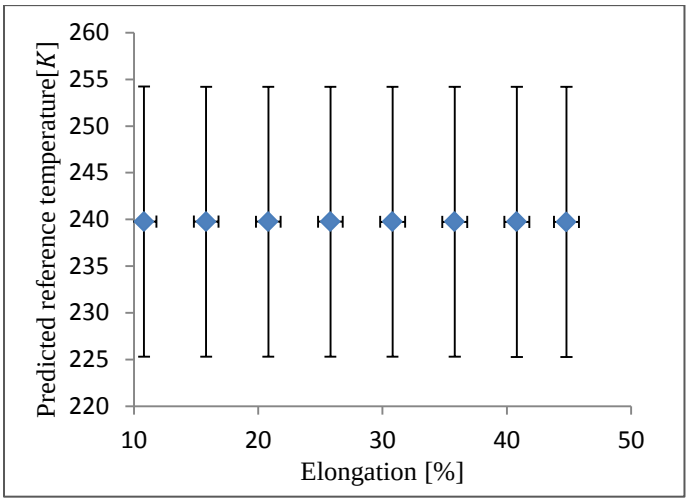

Fig. 55 Prediction of reference temperature in [K] against elongation [%] with error bars.

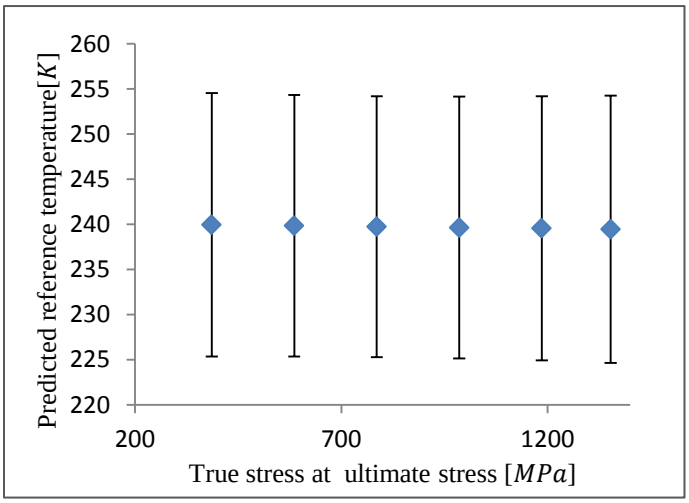

Fig. 56 Prediction of reference temperature in [K] against true stress at ultimate tensile stress [MPa] with error bars.

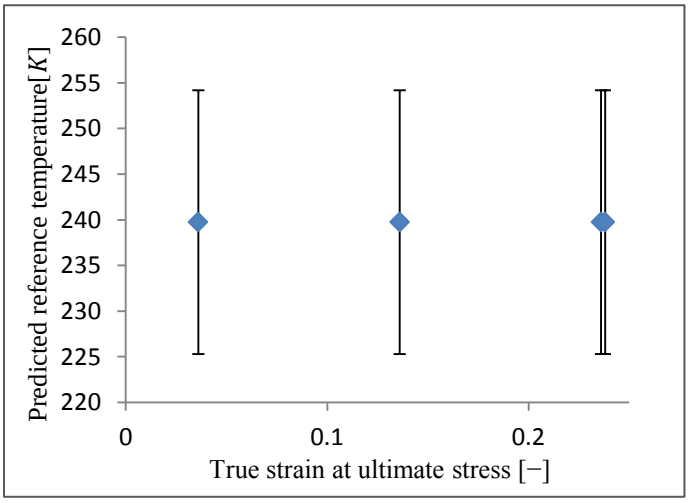

Fig. 57 Prediction of reference temperature in [K] against true strain at ultimate tensile stress [−] with error bars.

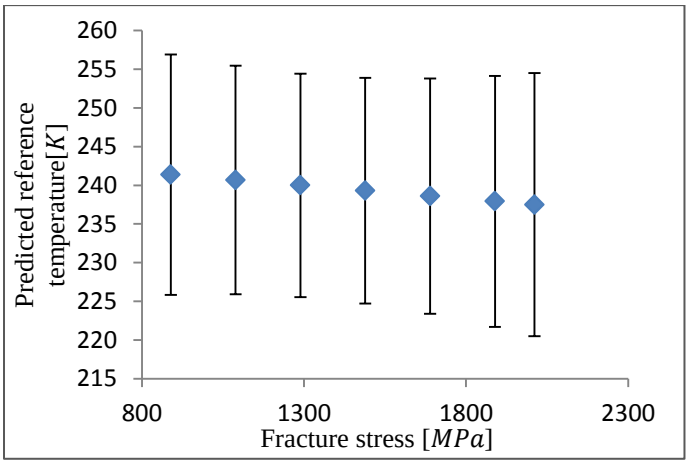

Fig. 58 Prediction of reference temperature in [K] against true fracture stress [MPa] with error bars.

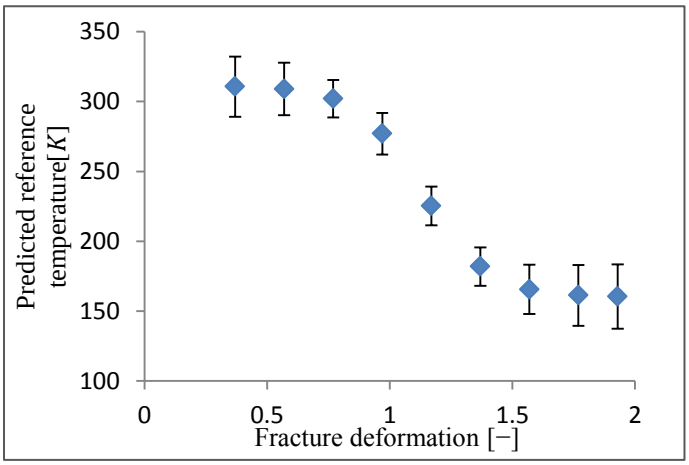

Fig. 59 Prediction of reference temperature in [K] against true fracture strain [−] with error bars.

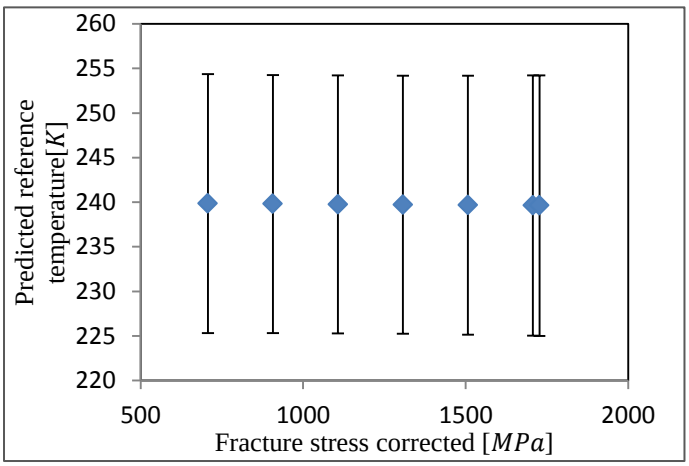

Fig. 60 Prediction of reference temperature in [K] against corrected fracture stress [MPa] with error bars.

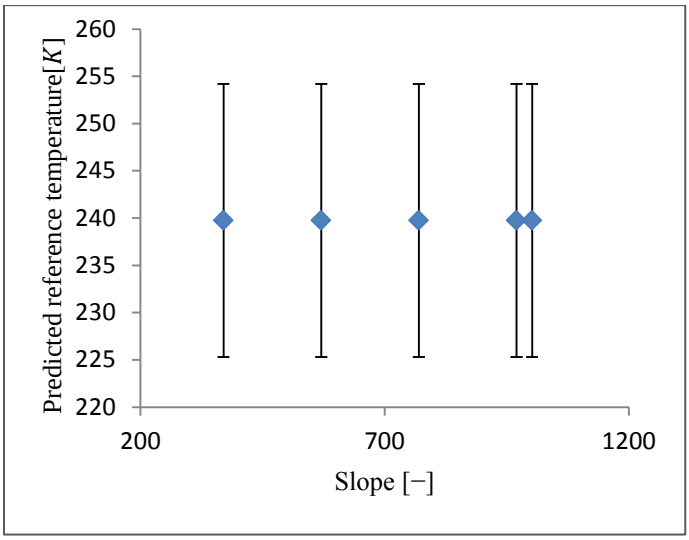

Fig. 61 Prediction of reference temperature in [K] against slope [−], a) with error bars, b) general trend.

The best way to evaluate the committee of submodels is by making predictions and comparing predictions with experimental data. Fig. 62 shows a plot of measured versus the predicted output using the selected committee; predictions are made by using all variables measured at both temperatures without including the temperature as an input variable.

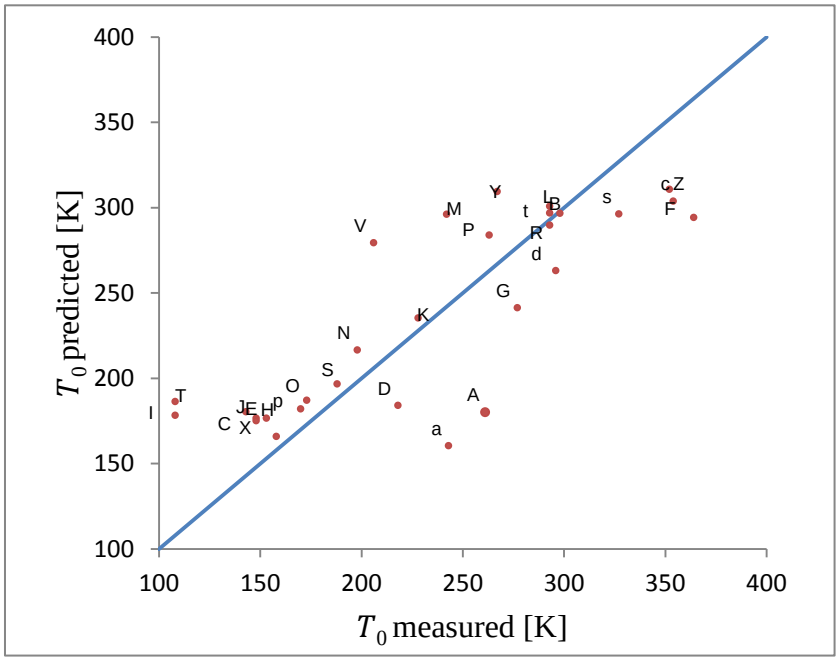

Fig. 62 Prediction of reference temperature in [K] against the measured reference temperature in [K]for the model of tensile properties and hardness on the input and reference temperature on the output side of ANN developed.

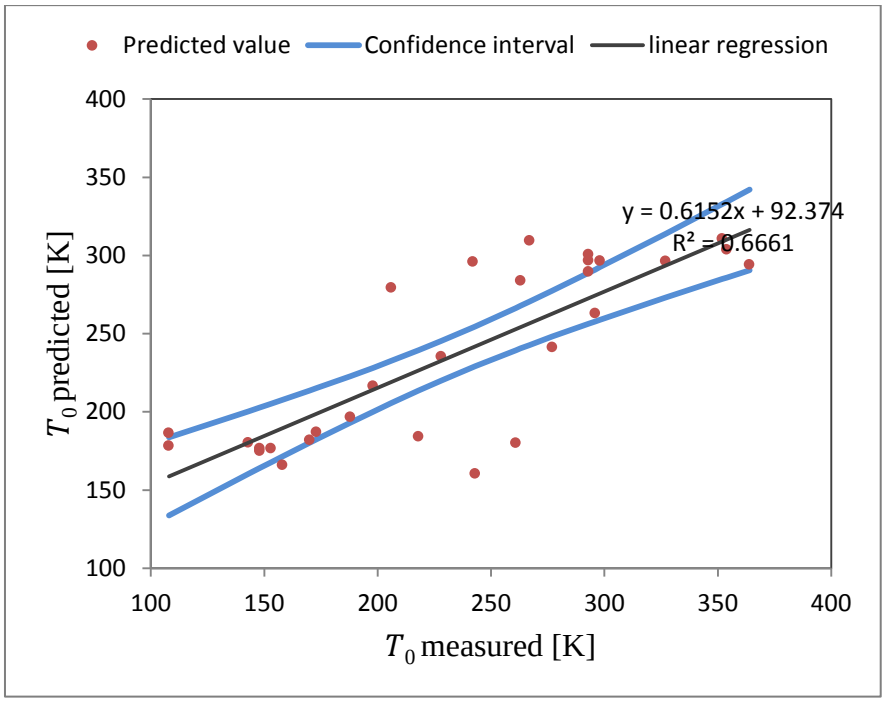

Fig. 63 The confidence band of linear regression at confidence level 95%.

In Fig. 63, we used confidence intervals to characterize the results. It was performed the linear regression of data (T_0 measured and T_0 predicted). The linear regression line has an equation of the form:

$$y = 0.6152x + 92.374, R^2 = 0.666, \tag{78}$$

where y refers to T_0 predicted, x refers to T_0 measured and R is the correlation coefficient which measures the goodness of fit of the data to the regression equation.

The confidence level used is 95% around the average. This means that there is a 95% probability that the true linear regression line of the population will lie within the confidence interval of the regression line calculated from data. The confidence interval of the prediction presents a range for the mean rather than the distribution of individual data points. It does not tell the likely range of all values, just how much the average value is likely to fluctuate.

5.2.2 The Second Model

The other submodels were trained using all parameters at room temperature including hardness values and temperature value as input variables. The minimum and maximum of each variable and the target are shown in Table 13.

After preparing the database, the submodels were trained differently and sorted according to the log predictive error. Fig. 64 shows the LPE with the number of hidden

units. The LPE has an optimum value at about two hidden units. In Fig. 65, the test error has the minimum value at one hidden unit.

The best submodel was selected according to the LPE and tested. The Model Manager makes predictions using the whole database, comparing them with the actual target values before forming a committee of submodels.

Table 13 The minimum and maximum values for the second database

Inputs	Min	Max	Average	St Dev
Hardness	90.2	406	223	78.0691
Temperature	295	295	295	0
Yield strength	194	934	527	206.6631
Ultimate stress	309	1306	699.3	220.271
Elongation	10.81	44.8	26.5	9.2857
True stress at ultimate stress	386	1353	776.4	211.3358
True strain at ultimate stress	0.036	0.238	0.118	0.0589
Fracture stress	889	2011	1359.1	260.4535
Fracture deformation	0.369	1.929	1.118	0.3433
Fracture stress	707	1727	1122.9	225.226
Slope	370	1002	595.2	136.8604
Reference temperature	108	364	233.4	74.7298

As mentioned previously, the optimum number of submodels to form the committee is determined depending on the combined test error of all the members of the committee. In this case, it was found to be 13 as shown in Fig. 66. This reduces the error and is the reason why the committee of submodels is used instead of the best submodel. The test error for the best submodel is 0.1335, while the combined test error of the committee is 0.1142. The selected committee makes predictions on the whole database.

Fig. 67 shows a plot of measured versus the predicted output. It is clear that this committee has less outliers than the previous committee which was formed for all parameters at room temperature, including hardness values without temperature value as an input variable.

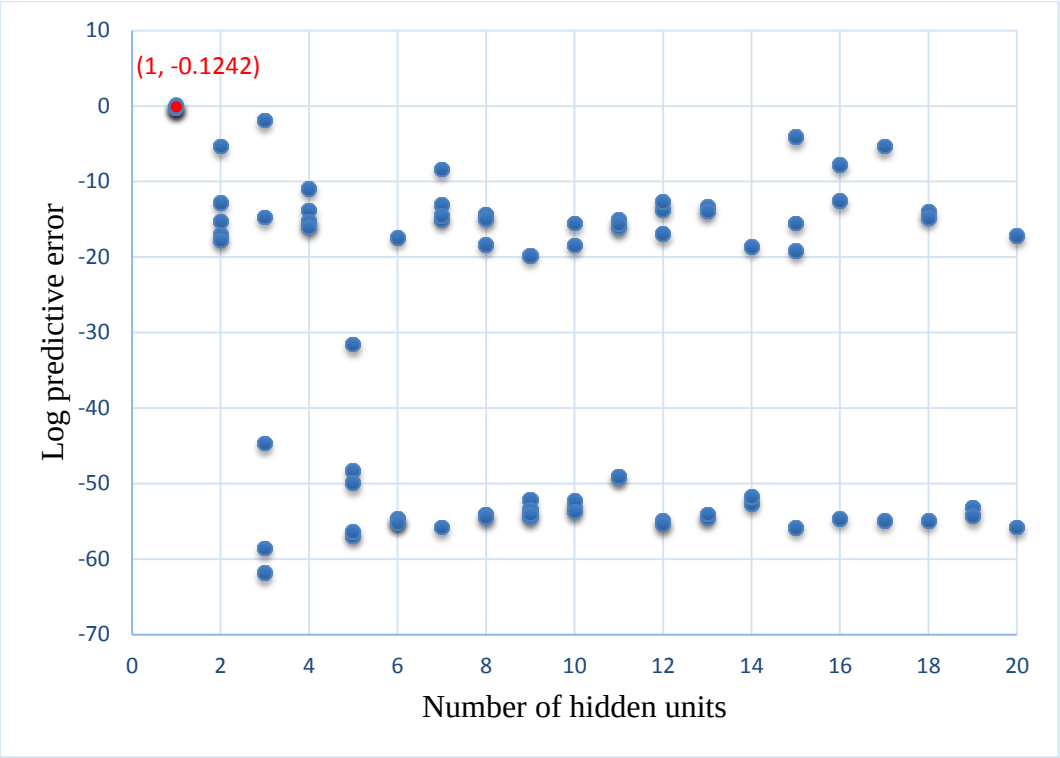

Fig. 64 The log predictive error during the training phase (second model).

Fig. 65 The test error during the training phase (second model).

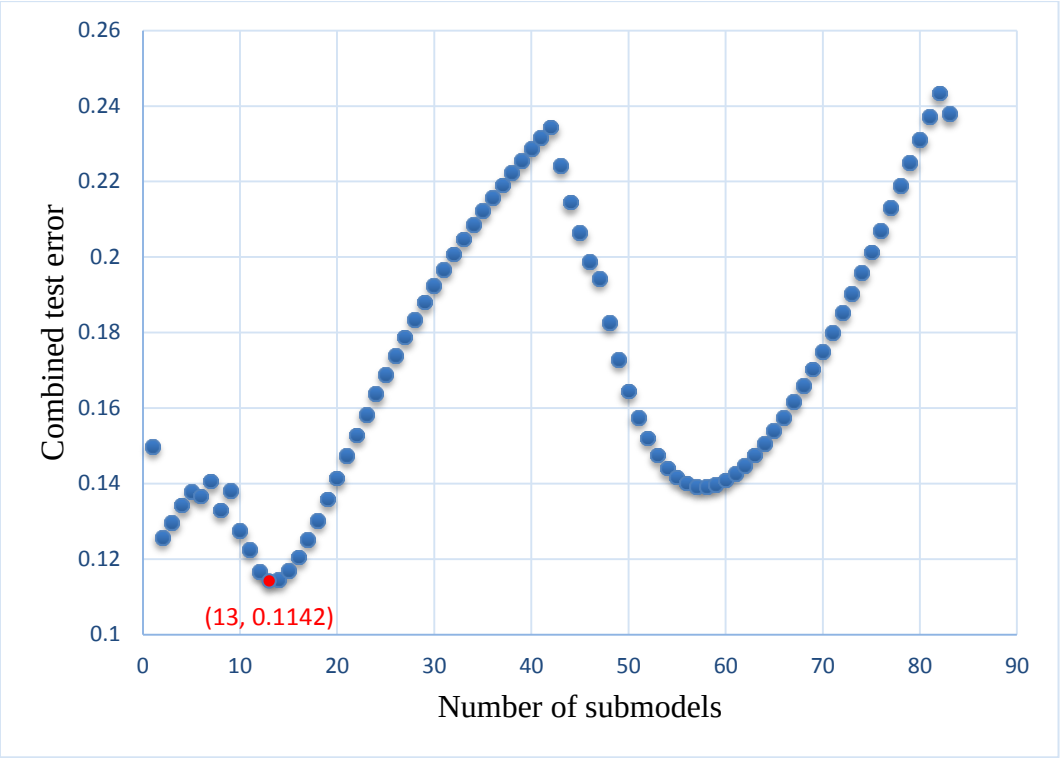

Fig. 66 The combined test error for committees of different sizes (second model).

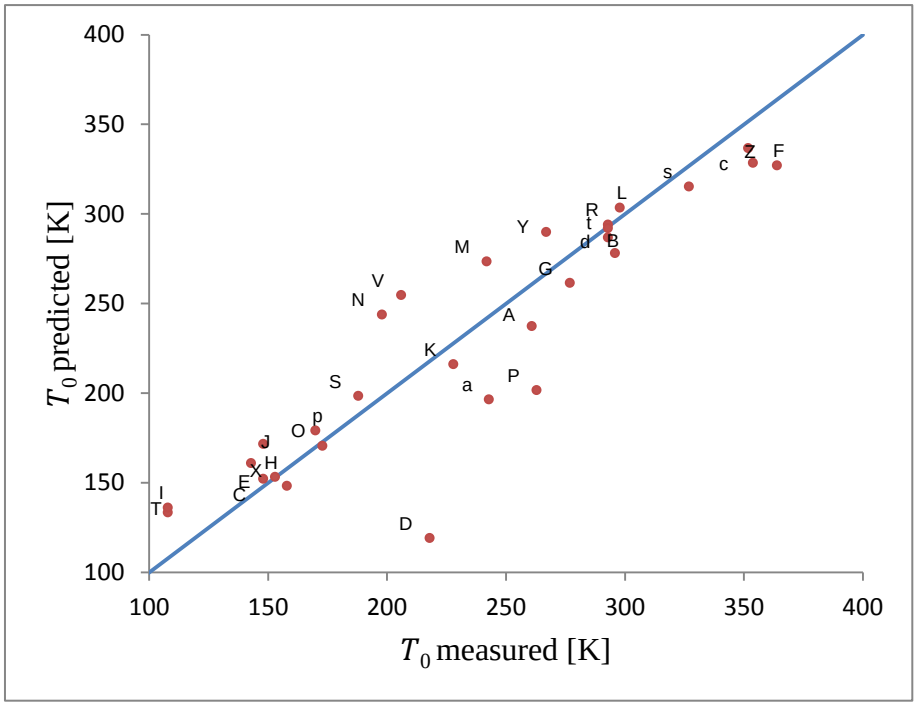

Fig. 67 Prediction of reference temperature in [K] against the measured reference temperature in [K] for the model of room temperature tensile properties, hardness, and test temperature (second model).

Fig. 68 shows the confidence band of linear regression of data (T_0 measured and T_0 predicted) at confidence level 95%. The linear regression line has an equation of the following form:

$$y = 0.8286x + 36.127, R^2 = 0.8234, \tag{79}$$

where y refers to T_0 predicted, x refers to T_0 measured and R is the correlation coefficient.

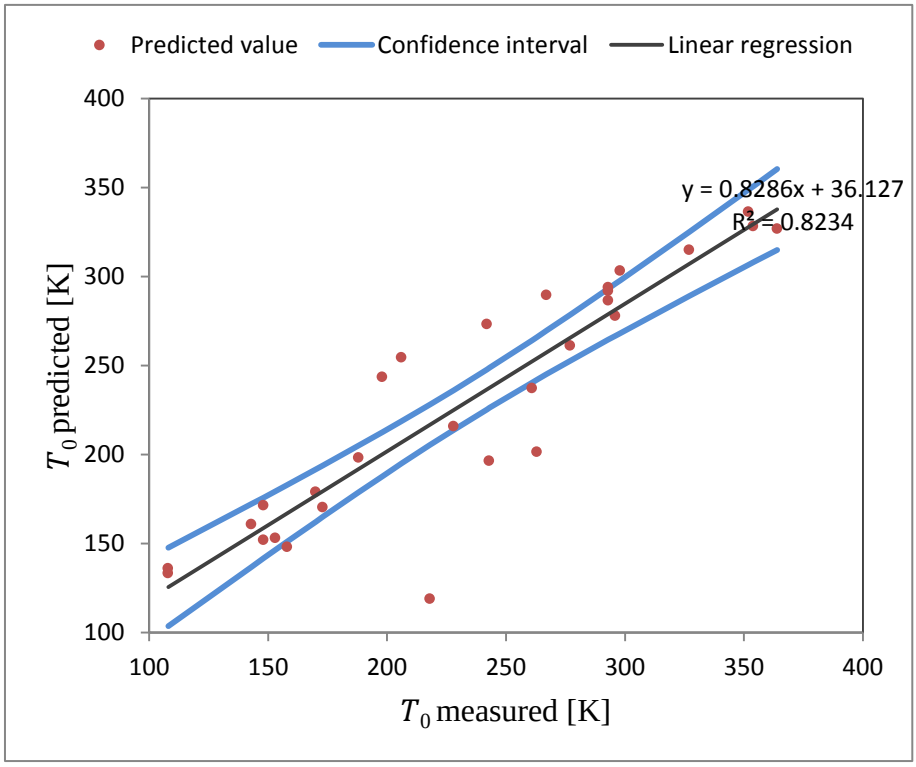

Fig. 68 The confidence band of linear regression at confidence level 95%.

5.2.3 The Third Model

In the third model, all measured parameters were used except the hardness values and temperature value. The input variables are shown in Table 14. The database was prepared and many submodels were trained and sorted according to the log predictive error. Fig. 69 shows the LPE with the number of hidden units. The LPE has an optimum value at one hidden unit. The test error has the minimum value (0.575) also at one hidden unit, as illustrated in Fig. 70. Fig. 71 shows the combined test error of committees. The best committee contains seven submodels.

Fig. 72 shows a plot of measured versus the predicted output. It is clear that this committee has more outliers than the previous models.

Table 14 The minimum and maximum values for the third database

Inputs	Min	Max	Average	St Dev
Yield strength	194	1018	649.2	227.3949
Ultimate stress	309	1469	810.5	242.5946
Elongation	10.81	44.8	25.3	8.5697
True stress at ultimate stress	386	1581	904	246.2912
True strain at ultimate stress	0.036	0.238	0.1192	0.052
Fracture stress	720	2011	1423.8	288.3218
Fracture deformation	0.0919	1014	18.4	133.0226
Fracture stress	707	1727	1197.7	249.3268
Slope	370	1062	658.4	156.6532
Reference temperature	108	364	232.9	73.9672

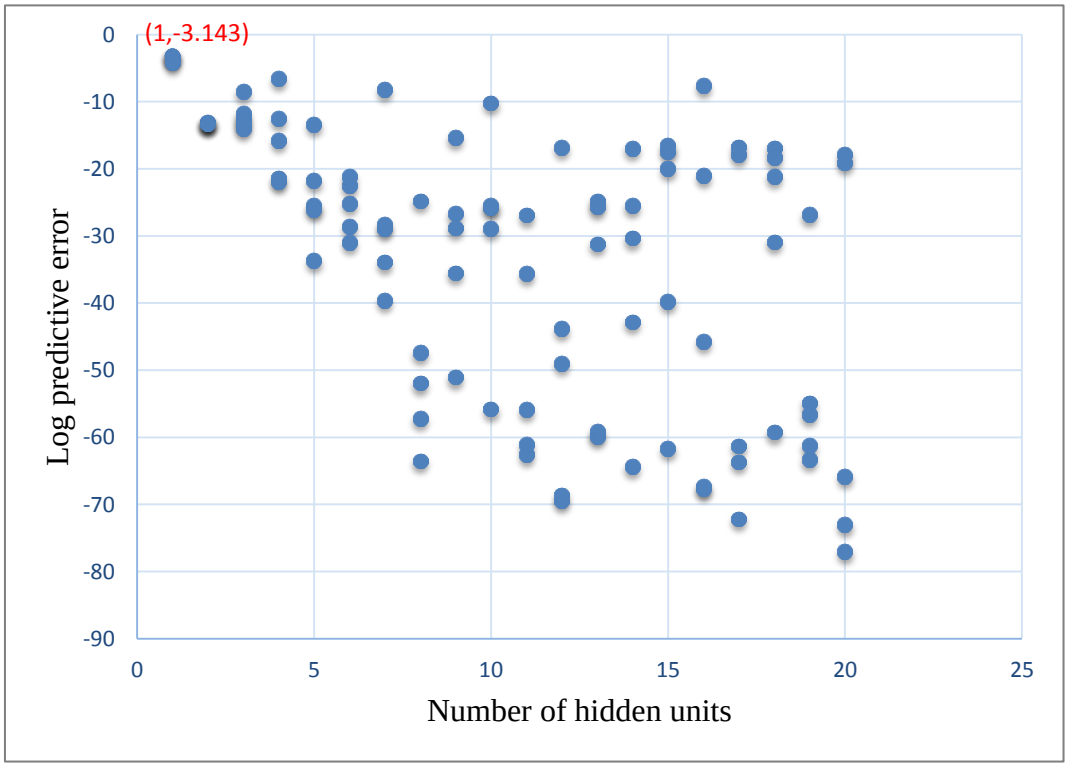

Fig. 69 The log predictive error during the training phase (third model).

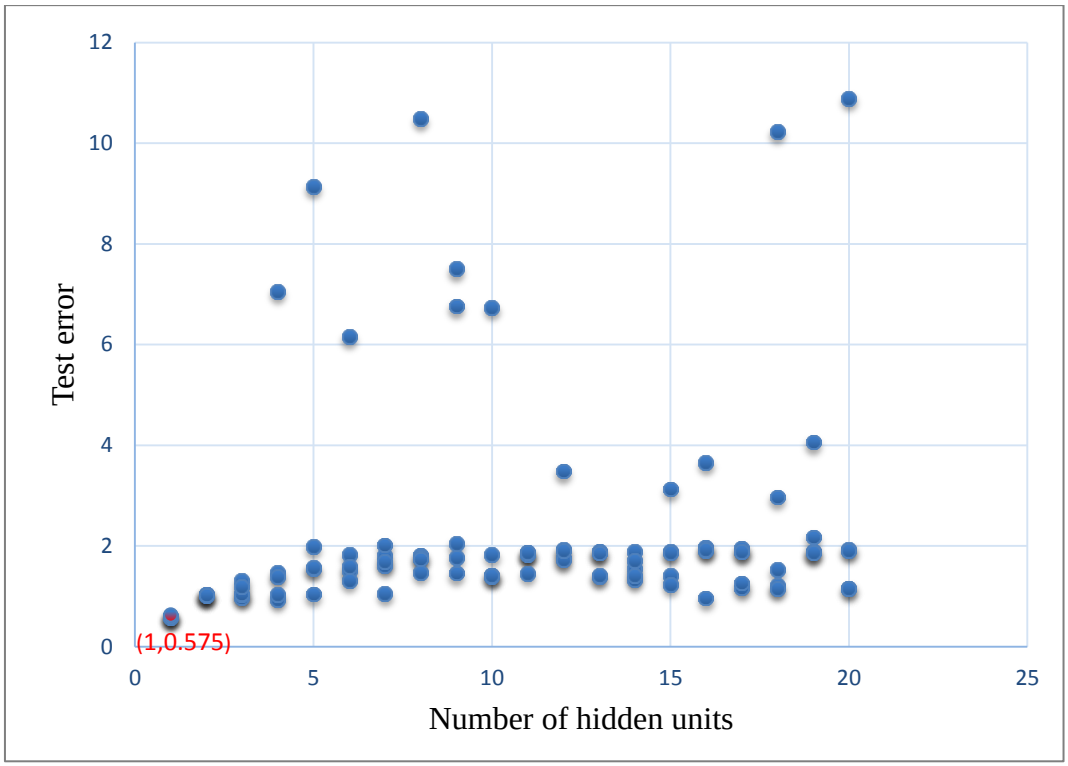

Fig. 70 The test error during the training phase (third model).

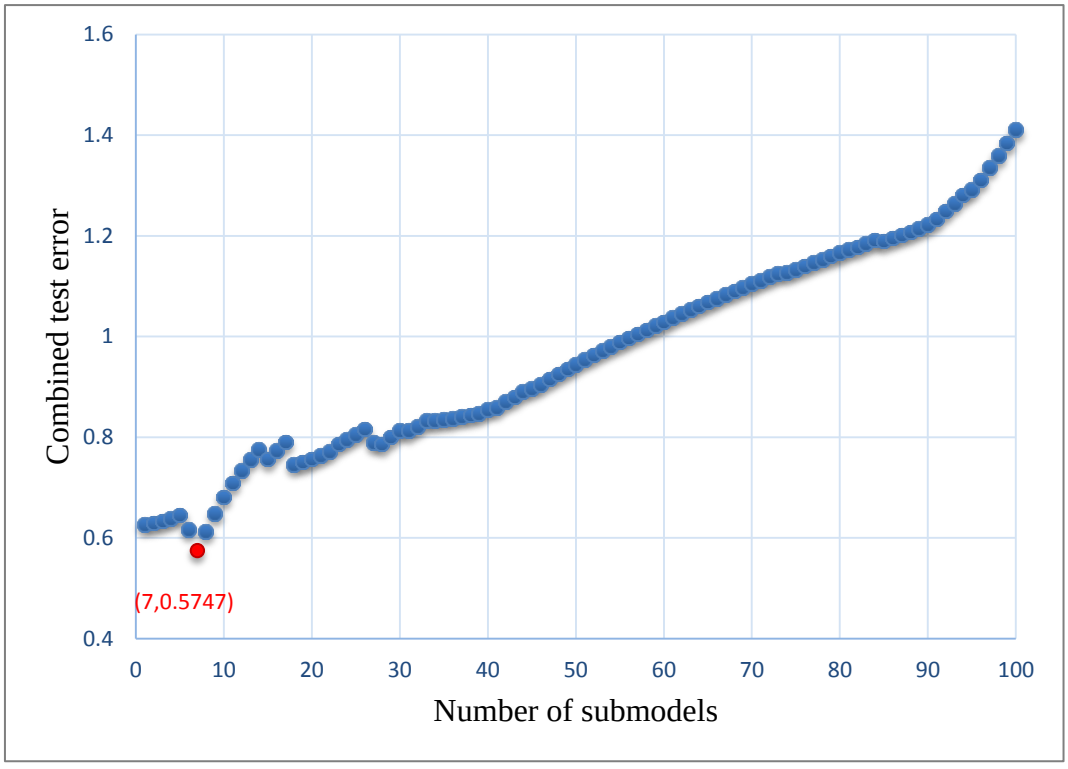

Fig. 71 The combined test error for committees of different sizes (third model).

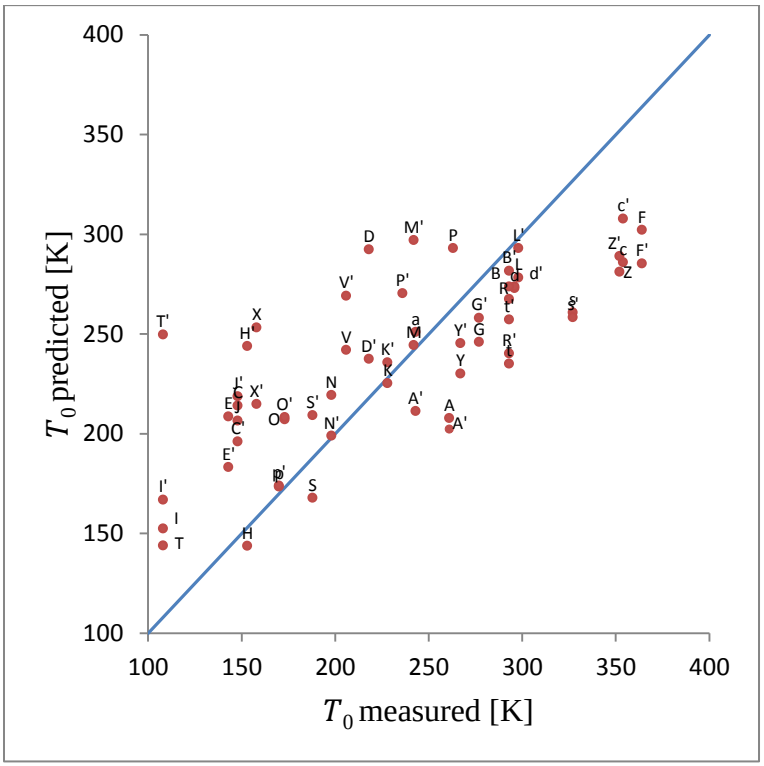

Fig. 72 Prediction of reference temperature in [K] against the measured reference temperature in [K] for the model of tensile properties and reference temperature (third model).

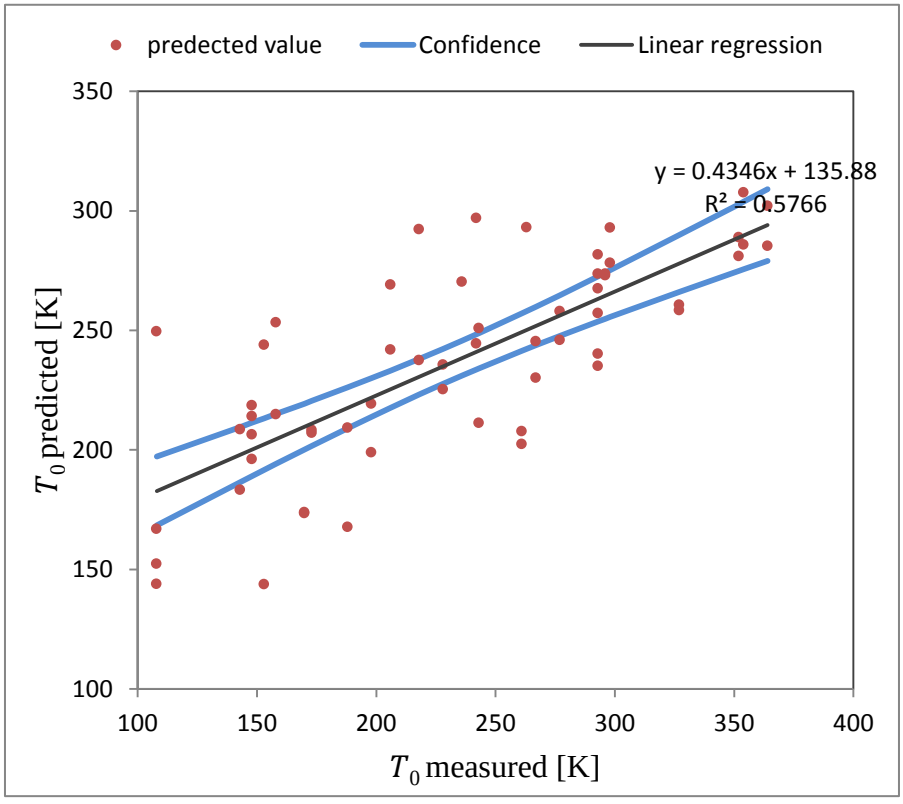

Fig. 73 The confidence band of linear regression at confidence level 95%.

Fig. 73 shows the confidence band of linear regression of data (T_0 measured and T_0 predicted) at confidence level 95%. The linear regression line has an equation of the following form:

$$y = 0.4346x + 135.88\,,\, R^2 = 0.5766, \tag{80}$$

where y refers to T_0 predicted, x refers to T_0 measured and R is the correlation coefficient.

5.2.4 The Fourth Model

The fourth model exploited findings from investigation related to reference temperature used only part of tensile test parameters (hardness, true stress at ultimate stress, fracture deformation, slope) at room temperature. Table 15 shows the input variables. The database was prepared and many submodels trained and sorted according to the log predictive error. Fig. 74 shows the LPE with the number of hidden units, with an optimum LPE value at two hidden units. The test error has the minimum value also at two hidden unit as illustrated in Fig. 75. The optimum number of submodels to form the committee was found to be one, as shown in Fig. 76.

Table 15 The minimum and maximum values for the fourth database

Inputs	Min	Max	Average	StDev
Hardness	90.2	406	217.5	77.68
True stress at ultimate stress	360	1359	760	218.28
Fracture deformation	0.35	I.15	1.15	0.37
Slope	362	1034	590.5	150.59
Reference temperature	108	364	229.4	75.76

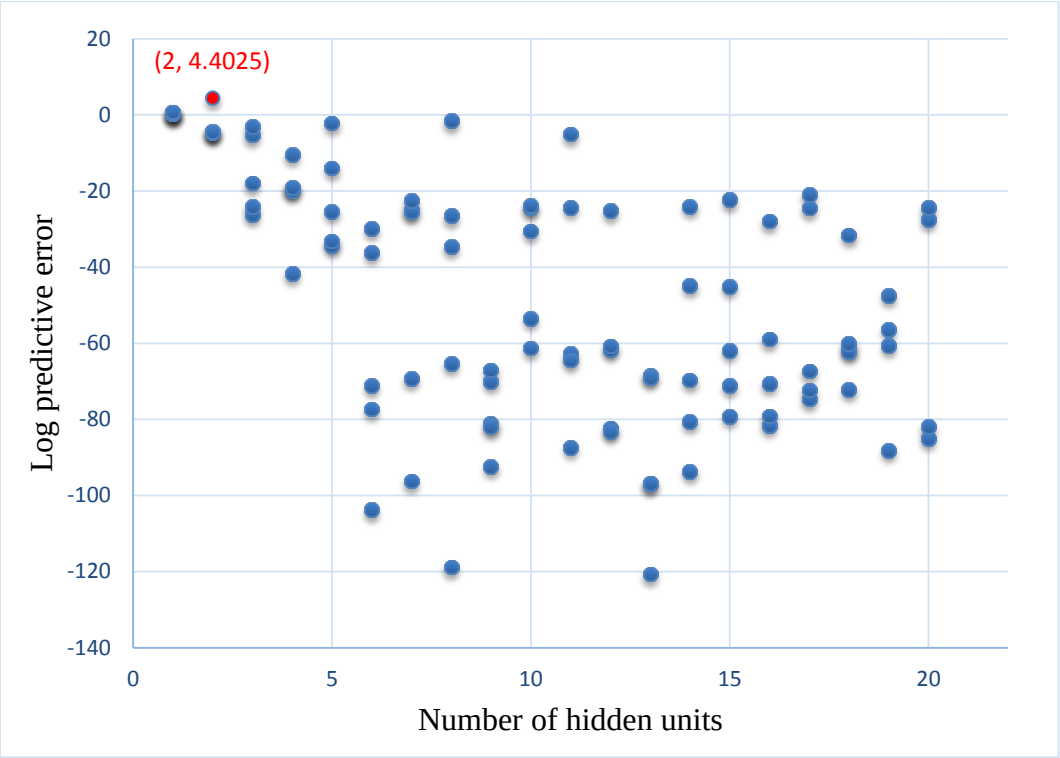

Fig. 74 The log predictive error during the training phase (fourth model).

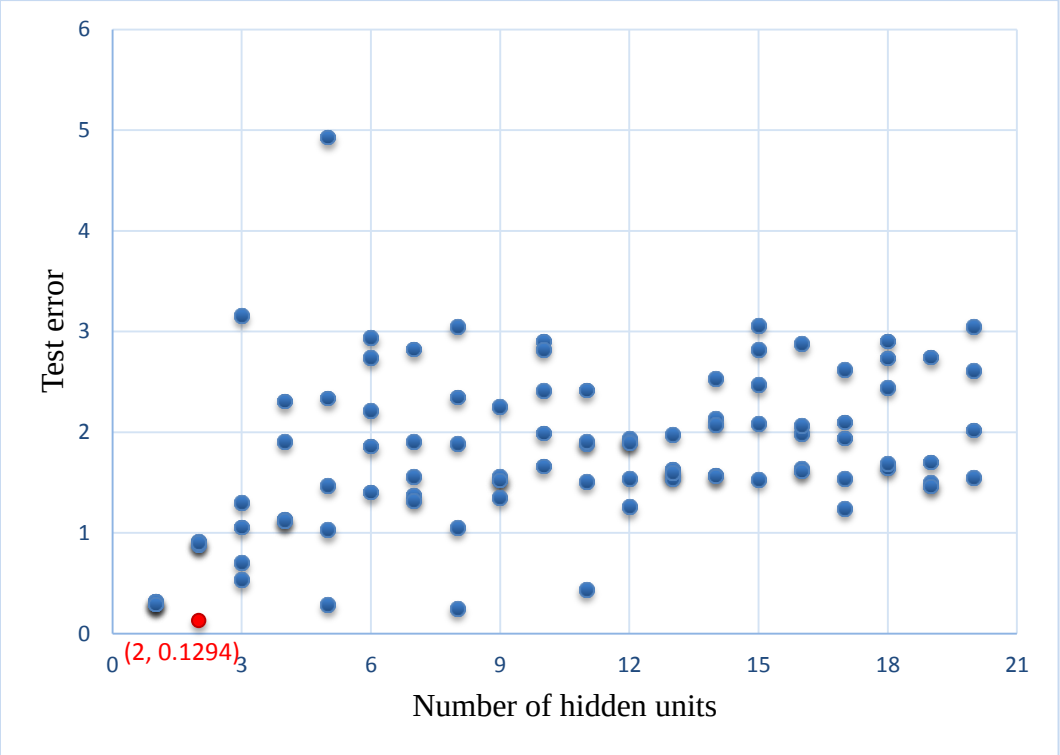

Fig. 75 The test error during the training phase (fourth model).

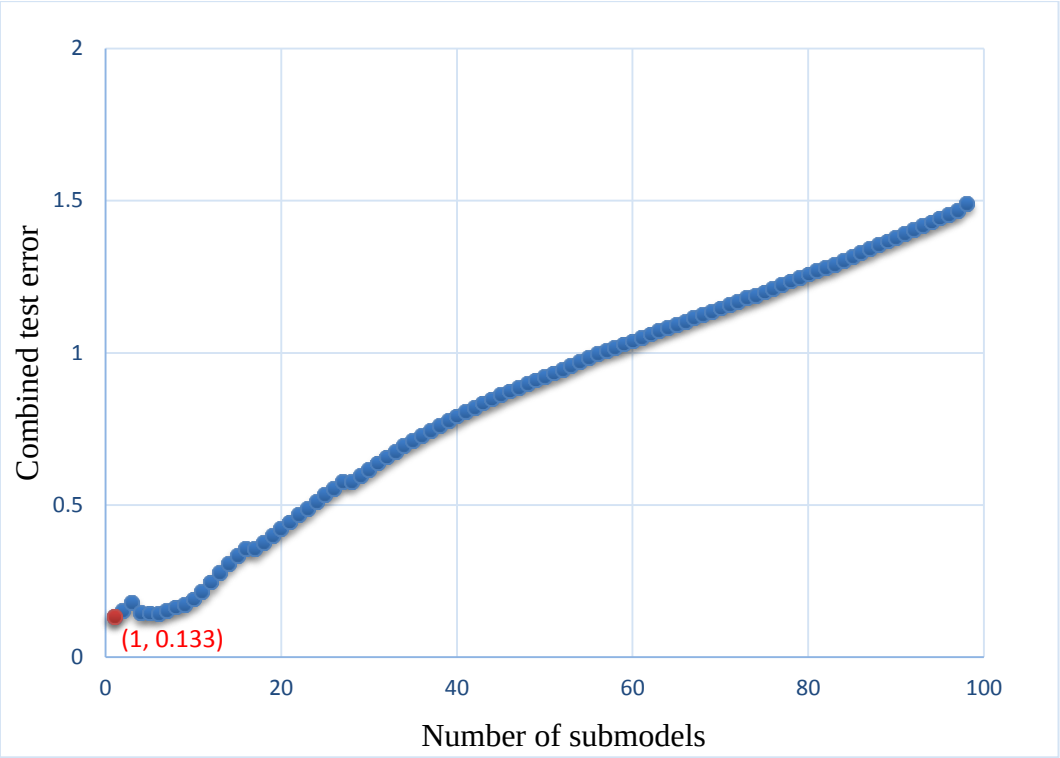

Fig. 76 The combined test error for committees of different sizes (fourth model).

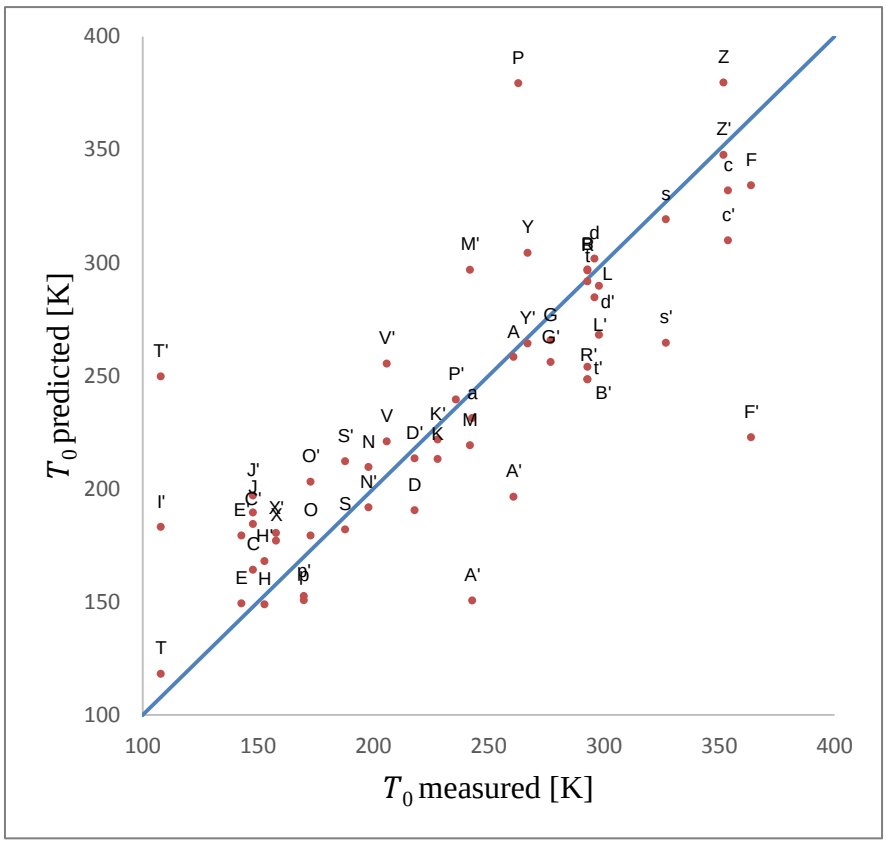

Fig. 77 Prediction of reference temperature in [K] against the measured reference temperature in [K] for the model of selected room temperature tensile properties (fourth model).

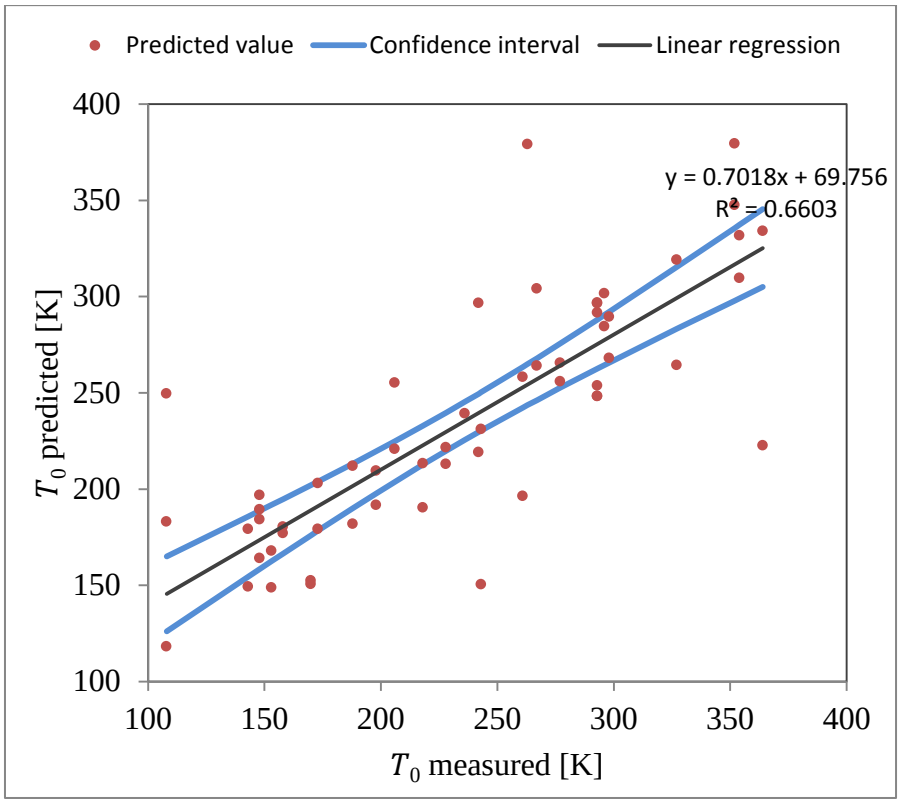

Fig. 78 The confidence band of linear regression at confidence level 95%.

Fig. 77 shows the plot of measured reference temperature versus the predicted reference temperature on output side and shows that this model also has more outliers than the previous models.

Fig. 78 shows the confidence band of linear regression of data (T_0 measured and T_0 predicted) at confidence level 95%. The linear regression line has an equation of the following form:

$$y = 0.7018x + 69.756\,, R^2 = 0.6603, \tag{81}$$

where y refers to T_0 predicted, x refers to T_0 measured and R is the correlation coefficient.

6 DISCUSSION

One of aims of the study has been to verify the validity of the master curve approach for evaluation of the dissimilar weld joint and/or thermally aged weld joints. Solution of this problem consisted from several subtasks: (i) Determination of the reference temperature for the base material, steel C20, and for the most brittle location very near the fusion line between steel C20 and overlay layer of the dissimilar joint; (ii) Verification of the applicability of the master curve concept for the weld material evaluation, in particular when dissimilar microstructures are playing a role; and, (iii) completion of data for reference temperature prediction by applying artificial neural network model developed for this particular case.

Obtained results have shown that for more or less homogeneous microstructures of the low alloy low carbon steel C20, either in as received condition or after thermal ageing applied, as expected, there is no problem related to the applicability of the master curve concept even if the number of fracture toughness values is relatively small. The minimum number of the experimental values recommended is seven [36], the reference temperature determination error is in this particular case usually around ±10 °C [24]. Note that for the investigated steel C20 it was no matter if the fracture toughness parameter was obtained in linear elastic or elastic plastic regime, all fracture toughness values are lying in the 90% probability scatter band. This is important finding, in particular in relation to critical application condition, e.g. in power industry including nuclear power stations, and the master curve approach can be thus applied for residual life predictions etc.

For the location very near to fusion line of the steel C20 with overlay alloy (50 to 80 μm from the fusion line as described in methodology description – chapter 4.1) the results have shown much more complicated figure. As described in chapter 5.1, the number of fracture toughness values lying below the lower 90% probability bound is comparably higher than 10 % of the entire data set. This means that the fracture of some of these samples occurred by micromechanism different form the remaining samples keeping the master curve definition conditions. This is typically an effect of local brittle zones (LBZ) that are often present in weld joints, both homogeneous and heterogeneous, and that control the crack initiation and development. For this particular case special, so called SINTAP procedure has been introduced as discussed in theoretical part of the thesis and based on overview [98]. Note that for application of this probabilistic approach comparably larger set of data is necessary because a number of them are step by step rejected from assessment and

the master curve may be quantified based on remaining data. Another possibility how to evaluate the outlying data can be based on identification of the fracture initiation mechanism acting for the particular samples. It has been shown in Fig. 6, that there are in principle two types of brittle fracture initiations mechanisms controlling the steel facture performance: Weakest link mechanism and accumulation of damage sites. The first type of fracture is identifiable in fracture surface by one initiation location from which the brittle cleavage fracture is propagating into different directions. This micromechanism has been identified in a part of the specimens lying outside the probability scatter band (see example in Fig. 79). The other type is typical by larger initiation region but it is not possible exactly to specify one initiation origin (cleavage facet) or there are several initiation origins from which the fracture propagates (Fig. 80).

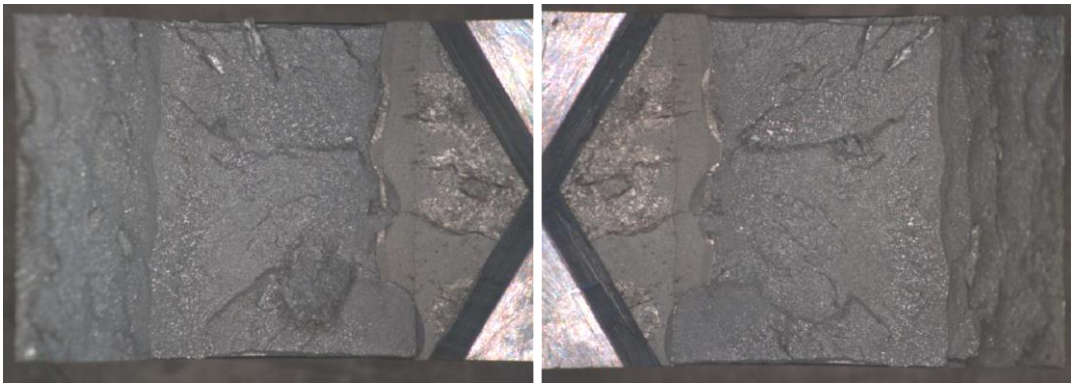

Fig. 79 Example of the fracture surface with linear elastic history showing one initiation origin (sample 103).

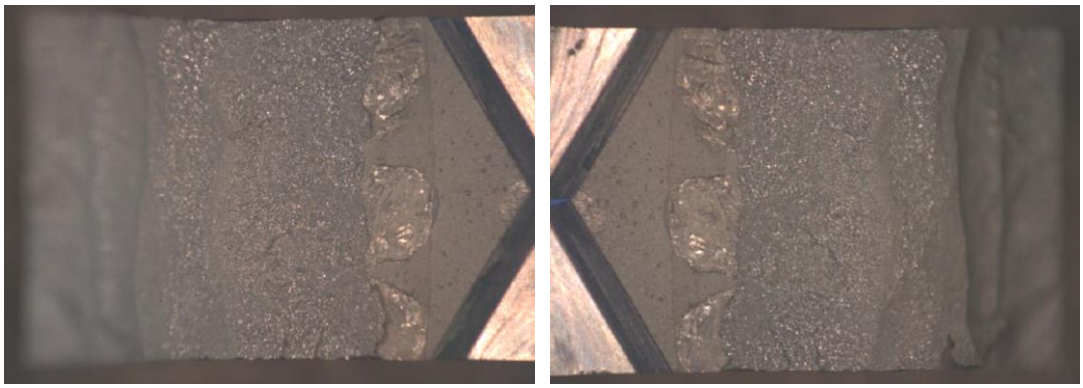

Fig. 80 Example of the fracture surface with linear elastic history showing unclear (several) initiation origins (sample 202).

After reassessment of fracture toughness data having linear elastic loading history and rejecting the values corresponding to accumulation of damage sites mechanism of initiation

the number of values lying outside the 90% probability scatter band dropped to only a few ones lying outside the probability scatter band. This approach appears to be good for explanation of the increased number of outlying data below the 95% bond of the scatter band, but the data cannot be simply rejected from consideration. On the contrary, for evaluation of fracture resistance of weld joint the most conservative values are the most important ones to be accounted because the fracture is controlled primarily by local brittle zones and presence/distribution of which in the particular sample is quite random. The SINTAP iteration process has been suggested to include this aspect into consideration [98] but, as above mentioned, the number of material and samples available did not enabled to apply this approach in our case.

Nevertheless, the experimental data and their good agreement with master curve and 90% probability scatter band clearly showed applicability of the MC concept for evaluation and prediction of fracture toughness data from dissimilar weld joint region showing the lowest fracture resistance.

When developing ANN models one of the intentions was to include the tensile specimens with circumferential notches into the analyses. The main reason was to get purely brittle performance characteristics into the data set of 29 steels predetermined for ANN modelling. This cannot be obtained for smoothed samples. Only with bars of the selected geometry was it possible at a quasistatic loading rate to reach two limit fracture mechanisms – transcrystalline cleavage and ductile tearing. At the reference temperature to be obtained on the output side of the neural analysis there is a predominant occurrence of transcrystalline cleavage fracture, in some cases with small areas of ductile fracture and ductile fracture pre-cracking preceding to cleavage. One of the expected properties of artificial neural network should be its ability to predict the parameter corresponding to the transition area from limit parameters corresponding with lower and upper threshold values, i.e. purely brittle cleavage and purely ductile microvoid coalescence fracture. For this purpose, the selected property of pure cleavage fracture was the general yield temperature T_{gy} determined as the temperature of coincidence of fracture force and force at the limit of macroplastic deformations. The fracture data determined at this temperature were then used, at very beginning of ANN development, as input parameters. Later this intention has been abandoned because of promising results/findings with reference prediction from smoothed samples.

When analysing the accuracy of T_{gy} determination, it was interesting to compare this general yield temperature (for tensile test bars with circumferential notches) with the

reference temperature (determined on the basis of fracture toughness measurement). The data are summarized in Fig. 81. The solid line shows the linear dependence gained by regression analysis (with the correlation coefficient 0.85). The correlation of both values is quite evident, but it was no ambition of authors to analyse this relation more deeply at this stage of investigation. Only in cases where the artificial neural network showed a remarkable deviation between the predicted and experimentally determined reference temperatures this correlation was used to discover whether the deviation was caused by some error in experimental determination of data or not.

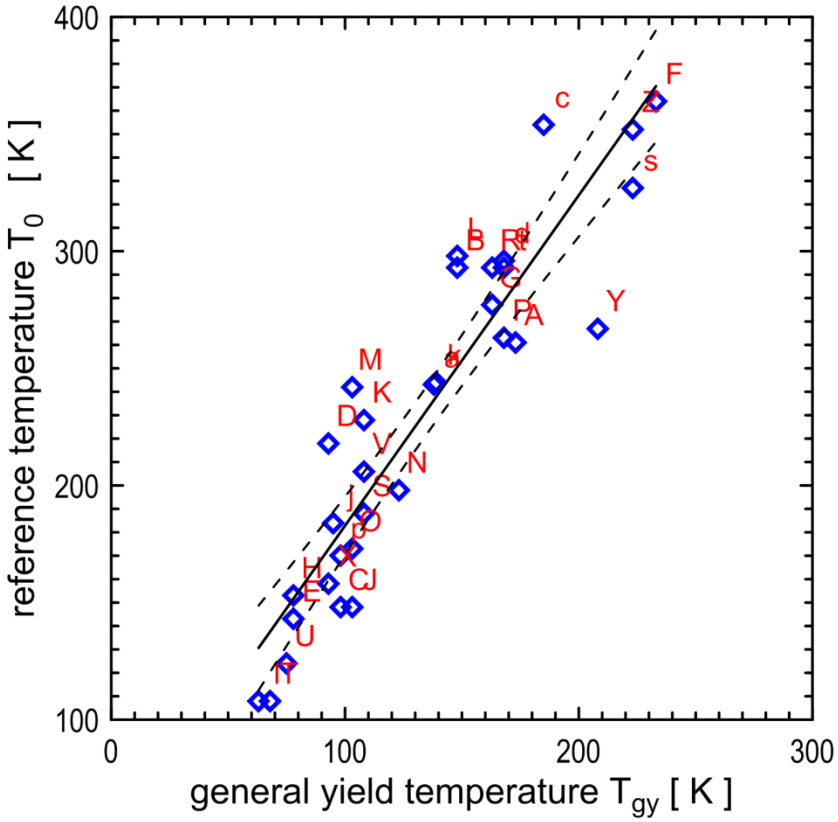

Fig. 81 Reference temperature T_0 correlated to general yield temperature T_{gy} of tensile test specimen with circumferential notch.

The thesis project has been also focused on development of quantitative model for the prediction of the reference temperature by means of artificial neural network. In order to fulfil this aim, it was necessary to carry out: (i) Collection and completion of data sets for suitable steels that could enable ANN development; (ii) Selection and development of the corresponding ANN model suitable for prediction of reference temperature including computing tools; and (iii) verification of the optimised model for the developing data set and for data sets characterising the dissimilar weld joint.

Note that for purposes of ANN training the data generated by different tests must be evidently fully compatible, i.e. made from the same steel batch, analogous orientation. That's why the data set used was relatively limited, only data measured by Brittle Fracture Group during last three decades have been used and when needed completed by additional tensile, fracture toughness and hardness tests. Data from literature are not having corresponding certainty regarding the same material, crack orientation etc. In addition, because of wrong results data sets have been rejected from evaluation based in incompatibility of results. Note that before the incorporating data into training they have been checked in similar way as shown in detail for the first model.

Four models have been investigated in this work. For evaluation of the relevancy of the predicted data two approaches have been applied. As shown in chapter 5.2, e.g. Fig. 47 and Fig. 48, log predictive error and test error during the training phase have been taken as parameters for selection of the right model (including number of hidden units etc.). For evaluation of prediction accuracy standard correlation analysis has been carried out for each of four models developed as shown in corresponding Figs. 63, 68, 73, 78, respectively. Comparison of all parameters is available from Table 16.

Table 16 The log predictive error and test error from ANN training stage and correlation coefficient for reference temperatures T_0 predicted and experimentally measured

	log predictive error	**test error**	**correlation coefficient (*R*)**
first model	-1.113	0.2363	0.82
second model	-0.1242	0.1335	0.91
third model	-3.143	0.575	0.76
fourth model	4.4025	0.1294	0.81

Based on the comparison of accuracy parameters from the four models investigated the best one appears to be the second one, i.e. model incorporating on the input side room temperature tensile test parameters, hardness and general yield temperature for notched tensile specimens. Because the notched tensile specimens are not commonly available (here this sample geometry was used for investigation purposes) the first model is giving also acceptable accuracy. It is the model working with room temperature tensile properties and hardness on the input side.

The analyses showed reliably which input parameters unambiguously influence the prediction of reference temperature. As mentioned nine different properties/numerical inputs of the smoothed and notched tensile specimens were investigated. Nevertheless, the notched bar tensile test and the general yield temperature proved to be exceptionally significant. So the best predictions were achieved by data set containing any parameter associated with the general yield temperature. Among the best predictions (generated for different combinations of input parameters), not one failed to include at least one of the following parameters: general yield temperature T_0, nominal fracture stress R_u, or reduction in area of notched bars Z^*. A surprising result was that in smooth bars, local material properties such as true fracture strain or slope of line beyond the plastic instability limit do not belong among the descriptors with a significant influence on prediction.

Having verified ANN models available the tensile test data from dissimilar weld joint dissimilar weld joint can be used to predict reference temperature of the master curve for the location near to fusion line. Because of material limitation only data from flat tensile test and hardness measurement have been available thus first model was used for these purposes. Steel C20 in as received and thermally aged condition (450°C/700 hrs) and, in addition, material from location very near to fusion line, also in as received and thermally aged conditions, were applied.

The results of these predictions are shown in the Table 17; note that these data have not been included into the training and verification phase of the ANN model development. Correlation of measured and predicted through the first ANN model reference temperatures has been found quite acceptable.

Table 17 Reference temperatures T_0 of the base material C20 and location near to the fusion line

	T_0 measured	**T_0 predicted (2st model)**
C20 as rec	-32.9	-27.1
C20 450°C/700 hrs	30.8	-33.3
W7 as rec	73.5	-64.9
W7 450°C/700 hrs	36	-25.7

It is evident that a limiting factor in the data processing was the limited number of data sets in the training set. This problem was addressed by selecting a prediction model that was suitable for small training sets – regularization neural networks. Additionally, the data sets were not divided into the usual training and testing sets as commonly; this problem was solved by using an iterative division method, i.e. each training set progressively became a testing set.

It is a justifiable assumption that increasing the number of input data sets (i.e. sets of mechanical parameters of steels included in the investigation) enable to develop and use a more complex ANN. This will improve the network's ability to generalize, and it will be possible to predict the reference temperature for the currently problematic steels with greater accuracy.

7 SUMMARY AND CONCLUSIONS

Following the above results, a Bayesian neural network model based on tensile test of smoothed and notched samples and mechanical properties from these tests has been proposed and verified to predict the reference temperature of applied steels group. In total 29 experimental data sets from low alloy steels each containing up to twenty different parameters are applied to learn four models of reference temperature prediction. A limiting factor in the data processing was the small number of data sets in the training set. However, it possible to get good generalization from models trained on small data sets. Bayesian regularization does not require that a validation data set be separate from the training data set; it uses all the data. The general performance of the models can be tested by predicting on all data. These were grouped into those within the range of data used for training and those outside the range (unseen data). The Bayesian approach offers a number of advantages including a solution to the problem of over-fitting. Since it finds the significance of each input and the variables which have little effect in explaining the output will be linked to small weights, there is no need to except any variable prior to the analysis.

This study indicated that the reference temperature T_0 of the master curve is predictable using Bayesian neural network models based on tensile test and mechanical properties. But the uncertainty characterizing the accuracy of the model tends to be large. One of way how to increase the accuracy is more input data need to be collected to improve the predictions of the model.

The best model was achieved when all the parameters were used as input variables (test temperature, hardness, yield strength, ultimate stress, elongation, true stress at ultimate stress, true strain at ultimate stress, fracture stress, fracture deformation, fracture stress corrected and slope). In this case, it is no need to exclude any parameter.

From this part of the present study, the following conclusions may be drawn:

1. Neural network models have been developed for the estimation of reference temperature based on tensile test and mechanical properties. The work has been applied to set of 29 steels containing material of various origins.
2. A neural network model has successfully been used to predict the reference temperature for a wide range of steels, and the model gave satisfactory predictions.
3. A neural network model based on the selected characteristics of a tensile test alone or hardness value alone did not give a satisfactory prediction for reference temperature.

4. For dissimilar weld joint material the prediction based on model including room temperature tensile parameters test parameters only supplied acceptable accuracy, however, a neural network model based on the selected characteristics of tensile test and hardness properties has been proposed to predict the reference temperature characterizing the fracture toughness transition behaviour in low alloy steels with predominantly ferritic structure. In general, the predictions are acceptable but the modelling uncertainty tends to be large. More input data is required for ferritic steels and further published research will improve the predictions of the model.

Eight sets of specimens cut from the dissimilar weld joint being in as received and thermally aged conditions were tested in the transition region. All of these specimens have been tested to obtain fracture toughness data and the results were evaluated relative to the fracture toughness Master Curve. The reference temperature was then calculated from the sets, based on this temperature 90% probability scatter band was then compared with experimental data. Importance of the Master curve concept for quantification of the fracture toughness temperature dependence has been also underlined.

It has been shown that for quantification of the fracture toughness temperature dependence in transition region of ferritic steels the Master curve concept is very useful tool and the transition behaviour can be characterised by single parameter, which is the reference temperature T_0 localizing the transition region on temperature axis. In addition, this concept enable to characterise the steel transition behaviour including the probability scatter band based on limited number of experimental values which is important aspect for designing structures and components

The main conclusions from this part of experimental works can be characterise as follow:

1) The master curve concept in the transition region of dissimilar weld joint materials is verified.
2) This work shows that use of compact tension specimens is possible producing valid results for reference temperature evaluation of ferritic steels as well as for weld metals.
3) The multi-temperature method for evaluating the T_0 has been confirmed as the most effective way to capture the scatter and temperature dependent of fracture toughness when limited number of samples is available.

BIBLIOGRAPHY

[1] M. Williams, "On the Stress Distribution at the Base of a Stationary Crack," *Journal of Applied Mechanics* vol. 24, pp. 109-114, 1957.

[2] N. Perez, *Fracture Mechanics (Mathematics and Its Applications)*: Springer, 2004.

[3] D. P. Miannay, *Fracture Mechanics (Mechanical Engineering Series)*: Springer, 1997.

[4] T. L. Anderson, *Fracture Mechanics Fundamentals and Applications*: CRC Press, 2004.

[5] A. Shukla, *Practical Fracture Mechanics in Design (Mechanical Engineering)*: CRC Press, 2004.

[6] D. Broek, *Elementary Engineering Fracture Mechanics*: Springer, 1982.

[7] G. R. Irwin, "Analysis of Stresses and Strains Near the End of a Crack Traversing a Plate," *SPIE Milestone Series* vol. 137, pp. 167-170, 1997.

[8] A. A. Griffith, "The Phenomena of Rupture and Flow in Solids," *Philosophical Transactions of the Royal society of London*, vol. 221, pp. 163-198, 1921.

[9] A. A. Wells, "Unstable Crack Propagation in Metals - Cleavage and Fast Fracture," *Cranfield Crack Propagation Symposium*, vol. 1, pp. 210-230, 1961.

[10] T. E. García, C. Rodríguez, and F. J. Belzunce, "Development of a New Methodology for Estimating the CTOD of Structural Steels Using the Small Punch Test," *Engineering Failure Analysis*, vol. 50, pp. 88–99, 2015.

[11] J. R. Rice, "A path Independent Integral and the Approximate Analysis of Strain Concentration by Notches and Cracks," *Journal of Applied Mechanics*, vol. 35, pp. 379-386, 1968.

[12] J. W. Hutchinson, "Singular Behaviour at the End of a Tensile Crack in a Hardening Material," *Journal of the Mechanics and Physics of Solids*, vol. 16, pp. 13-31, 1968.

[13] W. A. Sorem, R. H. Dodds, and S. T. Rolfe, "A Comparison of the J-Integral and CTOD Parameters for Short Crack Specimen Testing," *Elastic–Plastic Fracture Test Methods: The User's Experience* vol. 2, pp. 19-41, 1991.

[14] M. T. Kirk and R. H. Dodds, *J and CTOD Estimation Equations for Shallow Cracks in Single Edge Notch Bend Specimens*, 1993.

[15] E399-06e2, *Standard Test Method for Plane-Strain Fracture Toughness of Metallic Materials* vol. 3.01: ASTM International, West Conshohocken, 2008.

[16] "ISO-12135 Metallic materials–Unified method of test for the determination of quasistatic fracture toughness," *International Organization for Standardization, Geneva*, 2007.

[17] "ASTM-E–1820-99a-Standard Test Method for Measurement of Fracture Toughness. Annual Book of Astm Standards," ed: American Society for Testing and Materials, Philadelphia, Pa, USA, 2006.

[18] I. Dlouhy, M. Tarafder, and H. Hadraba, "Micromechanical Aspects of Transgranular and Intergranular Failure Competition," in *Key Engineering Materials*, 2011, pp. 399-402.

[19] P. Novak, R. Yuan, B. Somerday, P. Sofronis, and R. Ritchie, "A Statistical, Physical-Based, Micro-Mechanical Model of Hydrogen-Induced Intergranular Fracture in Steel," *Journal of the Mechanics and Physics of Solids,* vol. 58, pp. 206-226, 2010.

[20] A. Stroh, "The formation of cracks as a result of plastic flow," in *Proceedings of the Royal Society of London A: Mathematical, Physical and Engineering Sciences*, 1954, pp. 404-414.

[21] A. H. Cottrell, "Theory of Brittle Fracture in Steel and Similar Metals," *Trans. Met. Soc. AIME,* vol. 212, pp. 192-203, 1958.

[22] R. O. Ritchie, J. F. Knott, and J. R. Rice, "On the Relationship Between Critical Tensile Stress and Fracture Toughness in Mild Steel," *Journal of the Mechanics and Physics of Solids,* vol. 21, pp. 395-410, 1973.

[23] W.-S. Lei, "A statistical model of cleavage fracture in structural steels with power-law distribution of microcrack size," *Philosophical Magazine Letters,* vol. 96, pp. 101-111, 2016.

[24] I. Dlouhý, *Transferability of Fracture Mechanical Characteristics:* vol. 78: Springer Science and Business Media, 2012.

[25] A. Chatterjee, D. Chakrabarti, A. Moitra, R. Mitra, and A. Bhaduri, "Effect of deformation temperature on the ductile–brittle transition behavior of a modified 9Cr–1Mo steel," *Materials Science and Engineering: A,* vol. 630, pp. 58-70, 2015.

[26] R. Moskovic and B. Neale, "Treatment of Fracture Toughness Data in the Transition Regime," *Journal of Fatigue and Fracture of Engineering Materials and Structures,* vol. 16, pp. 1175-1185, 1993.

[27] A. Pineau, A. A. Benzerga, and T. Pardoen, "Failure of metals I: Brittle and ductile fracture," *Acta Materialia,* vol. 107, pp. 424-483, 2016.

[28] T. Yamamoto, G. Odette, D. Gragg, H. Kurishita, H. Matsui, W. Yang, *et al.*, "Evaluation of Fracture Toughness Master Curve Shifts for JMTR Irradiated F82H Using Small Specimens," *Journal of Nuclear Materials,* vol. 367, pp. 593-598, 2007.

[29] S. Bhowmik, P. Sahoo, S. K. Acharyya, S. Dhar, and J. Chattopadhyay, "Evaluation and Effect of Loss of Constraint on Master Curve Reference Temperature of 20MnMoNi55 Steel," *Engineering Fracture Mechanics,* vol. 136, pp. 142-157, 2015.

[30] A. Elazzizi, M. H. Meliani, A. Khelil, G. Pluvinage, and Y. Matvienko, "The Master Failure Curve of Pipe Steels and Crack Paths in Connection with Hydrogen Embrittlement," *International Journal of Hydrogen Energy,* vol. 40, pp. 2295-2302, 2015.

[31] M. Sokolov and H. Tanigawa, "5276-Application of the Master Curve Methodology to Fracture Toughness Characterization of Ferritic-Martensitic Steel," in *ICF11, Italy 2005*, 2013.

[32] D. E. McCabe, J. G. Merkle, and K. Wallin, *An Introduction to the Development and Use of the Master Curve Method*: ASTM International, 2005.

[33] K. Wallin, "Master Curve Analysis of Ductile to Brittle Transition Region Fracture Toughness Round Robin Data," *Journal of The EURO Fracture Toughness Curve,* 1998.

[34] V. Lyssakov and K. Kang, "Guidelines for Application of the Master Curve Approach to Reactor Pressure Vessel Integrity in Nuclear Power Plants," Electric Power Research Institute United States.2005.

[35] H. V. Viehrig, J. Böhmert, and J. Dzugan, "Some Issues by Using the Master Curve Concept," *Nuclear Engineering and Design,* vol. 212, pp. 115-124, 2002.

[36] D. Łowicki and S. Piotrowska, "Monetary valuation of road noise. Residential property prices as an indicator of the acoustic climate quality," *Ecological Indicators,* vol. 52, pp. 472-479, 2015.

[37] H. G. Pisarski and K. Wallin, "The SINTAP Fracture Toughness Estimation Procedure," *Journal of Engineering Fracture Mechanics,* vol. 67, pp. 613-624, 2000.

[38] E. Lucon and M. Scibetta, "Application of advanced Master Curve approaches to the EURO fracture toughness data set," in *Fatigue and Fracture Mechanics: 37th Volume*, ed: ASTM International, 2011.

[39] E. Martínez-Pañeda, T. E. García, and C. Rodríguez, "Fracture toughness characterization through notched small punch test specimens," *Materials Science and Engineering: A,* vol. 657, pp. 422-430, 2016.

[40] E. Budzakoska, D. Carr, P. Stathers, R. Harrison, A. Hellier, and W. Yeung, "Predicting the J Integral Fracture Toughness of Al 6061 Using the Small Punch Test," *Fatigue & Fracture of Engineering Materials and Structures,* vol. 30, pp. 796-807, 2007.

[41] E. Cárdenas, F. Belzunce, C. Rodriguez, I. Penuelas, and C. Betegon, "Application of The Small Punch Test to Determine the Fracture Toughness of Metallic Materials," *Journal of Fatigue and Fracture of Engineering Materials & Structures,* vol. 35, pp. 441-450, 2012.

[42] M. Abendroth and M. Kuna, "Determination of Deformation and Failure Properties of Ductile Materials by Means of the Small Punch Test and Neural Networks," *Journal of Computational Materials Science,* vol. 28, pp. 633-644, 2003.

[43] J.-Y. Jeon, Y.-J. Kim, S.-Y. Lee, and J.-W. Kim, "Extracting ductile fracture toughness from small punch test data using numerical modeling," *International Journal of Pressure Vessels and Piping,* vol. 139, pp. 204-219, 2016.

[44] J. R. Foulds, P. J. Woytowitz, T. K. Parnell, and C. W. Jewett, "Fracture Toughness by Small Punch Testing," *Journal of Testing and Evaluation,* vol. 23, pp. 3-10, 1995.

[45] T. Wei, D. Carr, E. Budzakoska, W. Payten, R. Harrison, and M. Ripley, "Assessment of the Fracture Toughness of 6061 Aluminium by the Small Punch Test and Finite Element Analysis," in *Materials Forum*, 2006, pp. 39-44.

[46] J. J. Bog and D. Kwon, "Assessment of Fracture Characteristics from Revised Small Punch Test using Pre-Cracked Specimen," *Journal of Metals and Materials,* vol. 4, pp. 742-746, 1998.

[47] M. Young, J. W. Choi, and K. B. Yoon, "Change of Anisotropic Tensile Strength Due to Amount of Severe Plastic Deformation In Aluminum 2024 Alloy," *Journal of Materials Science and Engineering,* vol. 529, pp. 1-8, 2011.

[48] J. J. Bog, J. Jang, and D. Kwon, "Evaluation of Fracture Toughness by Small-Punch Testing Techniques Using Sharp Notched Specimens," *International Journal of Pressure Vessels and Piping,* vol. 80, pp. 221-228, 2003.

[49] R. Cryderman, D. Rickert, K. Puzak, J. Speer, D. Matlock, and M. Burnett, "Effects of Chemical Composition, Heat Treatment, and Microstructure in Splittable Forged Steel Connecting Rods," *SAE International Journal of Materials and Manufacturing,* vol. 8, pp. 1-9, 2015.

[50] A. Kariya, K. Tagaya, T. Kaita, and K. Fujii, "Mechanical Properties of Corroded Steel Plate Under Tensile Force," in *Proceedings of the 3rd International Structural Engineering and Construction Conference (ISEC-03), Japan*, 2005, pp. 105-110.

[51] F. Haggag and R. Nanstad, "Estimating Fracture Toughness Using Tension or Ball Indentation Tests and a Modified Critical Strain Model," vol. 170, ed: PVP, 1989, pp. 41-46.

[52] H. K. Khandelwal, K. Sharma, and R. Chhibber, "Mechanical Property Estimation of Similar Weld using Ball Indentation Technique," *Journal of Minerals and Materials Characterization and Engineering,* vol. 11, pp. 1095-1100, 2012.

[53] K. Sharma, P. Singh, V. Bhasin, and K. Vaze, "Application of Automated Ball Indentation for Property Measurement of Degraded Zr2. 5Nb," *Journal of Minerals & Materials Characterization and Engineering,* vol. 10, pp. 661-669, 2011.

[54] B. Zou, K. S. Guan, and S. B. Wu, "Determination of area reduction rate by continuous ball indentation test," *International Journal of Pressure Vessels and Piping,* vol. 139, pp. 220-227, 2016.

[55] J. Kruzic, D. Kim, K. Koester, and R. Ritchie, "Indentation Techniques for Evaluating the Fracture Toughness of Biomaterials and Hard Tissues," *Journal of the Mechanical Behavior of Biomedical Materials,* vol. 2, pp. 384-395, 2009.

[56] C. S. Catherine, C. Poussard, J. Vodinh, R. Schill, N. Hourdequin, P. Galon, *et al.*, "Finite Element Simulations and Empirical Correlation for Charpy-V and Subsize Charpy Tests on an Unirradiated Low-Alloy RPV Ferritic Steel," *Astm Special Technical Publication,* vol. 1418, pp. 107-136, 2002.

[57] W. Schmitt, H. Talja, W. Boehme, S. Oeser, and H. Stoeckl, "Characterization of Ductile Fracture Toughness Based on Subsized Charpy and Tensile Test Results," *ASTM Special Technical Publication,* vol. 1329, pp. 63-81, 1998.

[58] T. E. Panduro and K. L. Veie, "Classification and valuation of urban green spaces—A hedonic house price valuation," *Landscape and Urban planning,* vol. 120, pp. 119-128, 2013.

[59] K. Wallin, T. Planman, M. Valo, and R. Rintamaa, "Applicability of miniature size bend specimens to determine the master curve reference temperature T0," *Journal of Engineering Fracture Mechanics,* vol. 68, pp. 1265-1296, 2001.

[60] K. Edsinger, G. Odette, G. Lucas, and J. Sheckherd, "The Effect of Size, Crack Depth and Strain Rate on Fracture Toughness -Temperature Curves of a Low Activation Martensitic Stainless Steel," *Journal of Nuclear Materials,* vol. 233, pp. 342-346, 1996.

[61] B. S. Lee, J. H. Hong, W. J. Yang, M. Y. Huh, and S. H. Chi, "Master Curve Characterization of the Fracture Toughness in Unirradiated and Irradiated RPV Steels Using Full-and 1/3-Size Pre-Cracked Charpy Specimens," *International Journal of Pressure Vessels and Piping,* vol. 77, pp. 599-604, 2000.

[62] E. Gaganidze, B. Dafferner, and J. Aktaa, "Fracture Mechanical Experiments on EUROFER 97 and MANET II Mini-bar Specimens," *Journal of Forschungszentrum Karlsruhe, FZKA,* vol. 7252, 2006.

[63] M. Scibetta, E. Lucon, and E. Van Walle, "Optimum Use of Broken Charpy Specimens from Surveillance Programs for the Application of the Master Curve Approach," *International Journal of Fracture,* vol. 116, pp. 231-244, 2002.

[64] H. C. Schneider, "Entwicklung Einer Miniaturisierten Bruchmechanischen Probe Fur Nachbestrahlungsuntersuchungen," *Wissenschaftliche Berichte FZKA,* vol. 7066, 2005.

[65] E. Lucon and M. Scibetta, "Miniature Compact Tension Specimen for Upper Shelf Toughness Measurements on RPV Steels," *Small Specimen Test Techniques: 5th volume, ASTM STP,* vol. 1502, pp. 18-31, 2009.

[66] M. Scibetta, J. Schuurmans, E. Lucon, and E. van Walle, "On the Use of the Crack Tip Opening Angle Parameter to Explain the Ductile Crack Growth Behavior of Miniature Compact Specimens," *Engineering Fracture Mechanics,* vol. 75, pp. 3599-3610, 2008.

[67] M. Sokolov, R. Klueh, R. Odette, K. Shiba, and H. Taginawa, "Fracture Toughness Characterization of Irridiated F82H in The Transition Region," in *Effects of Radiation on Materials: 21st International Symposium, ASTM STP,* 2004, pp. 408-416.

[68] M. Li, M. Sokolov, and S. Zinkle, "Tensile and Fracture Toughness Properties of Neutron-Irradiated CuCrZr," *Journal of Nuclear Materials,* vol. 393, pp. 36-46, 2009.

[69] G. Odette, T. Yamamoto, H. Kishimoto, M. Sokolov, P. Spätig, W. Yang, *et al.*, "A Master Curve Analysis of F82H Using Statistical and Constraint Loss Size Adjustments of Small Specimen Data," *Journal of Nuclear Materials,* vol. 329, pp. 1243-1247, 2004.

[70] L. I. Perlovsky, *Neural Networks and Intellect: using model-based concepts*: Oxford University Press New York, 2001.

[71] A. Powar and P. Date, "Modeling of microstructure and mechanical properties of heat treated components by using Artificial Neural Network," *Materials Science and Engineering: A,* vol. 628, pp. 89-97, 2015.

[72] K. Guan, L. Jia, X. Chen, J. Weng, F. Ding, and H. Zhang, "Improvement of fracture toughness of directionally solidified Nb-silicide in situ composites using artificial neural network," *Materials Science and Engineering: A,* vol. 605, pp. 65-72, 5/27/ 2014.

[73] G. Partheepan, D. K. Sehgal, and R. K. Pandey, "Fracture toughness evaluation using miniature specimen test and neural network," *Computational Materials Science,* vol. 44, pp. 523-530, 12// 2008.

[74] A. Seibi and S. Al-Alawi, "Prediction of fracture toughness using artificial neural networks (ANNs)," *Engineering fracture mechanics,* vol. 56, pp. 311-319, 1997.

[75] M. Çöl, H. Ertunç, and M. Yılmaz, "An artificial neural network model for toughness properties in microalloyed steel in consideration of industrial production conditions," *Materials & design,* vol. 28, pp. 488-495, 2007.

[76] M. E. Haque and K. Sudhakar, "ANN back-propagation prediction model for fracture toughness in microalloy steel," *International Journal of Fatigue,* vol. 24, pp. 1003-1010, 2002.

[77] J. Kang, B. Choi, and H. Lee, "Application of artificial neural network for predicting plain strain fracture toughness using tensile test results," *Fatigue & fracture of engineering materials & structures,* vol. 29, pp. 321-329, 2006.

[78] D. Dunne, H. Tsuei, and Z. Sterjovski, "Artificial neural networks for modelling of the impact toughness of steel," *ISIJ international,* vol. 44, pp. 1599-1607, 2004.

[79] A. Abdulbaky, D. Al-Fatta, H. Bhadeshia, and T. A. Jabbar, "A Model for The Prediction of Fracture Toughness Using Neural Network," *Eng. & Tech. Journal,* vol. 30, pp. 868-885, 2012.

[80] A. Al Hamdany, D. Al Fattal, T. Jabbar, and H. Bhadeshia, "Estimation of fracture toughness of tempered nanostructured bainite," *Materials Science and Technology,* vol. 28, pp. 685-689, 2012.

[81] M. Abendroth and M. Kuna, "Identification of ductile damage and fracture parameters from the small punch test using neural networks," *Engineering Fracture Mechanics,* vol. 73, pp. 710-725, 4// 2006.

[82] D. J. MacKay, "A practical Bayesian framework for backpropagation networks," *Neural computation,* vol. 4, pp. 448-472, 1992.

[83] J. Pak, J. Jang, H. Bhadeshia, and L. Karlsson, "Optimization of neural network for Charpy toughness of steel welds," *Materials and Manufacturing Processes,* vol. 24, pp. 16-21, 2008.

[84] K. Ichikawa, H. Bhadeshia, and D. MacKay, "Model for solidification cracking in low alloy steel weld metals," *Journal of Science and Technology of Welding and Joining,* vol. 1, pp. 43-50, 1996.

[85] T. Cool, H. Bhadeshia, and D. MacKay, "The yield and ultimate tensile strength of steel welds," *Journal of Materials Science and Engineering,* vol. 223, pp. 186-200, 1997.

[86] H. Bhadeshia, "Neural networks in materials science," *International Journal of The Iron and Steel Institute of Japan ISIJ* vol. 39, pp. 966-979, 1999.

[87] K. Wallin, "The scatter in K Ic-results," *Engineering Fracture Mechanics,* vol. 19, pp. 1085-1093, 1984.

[88] Y. Zhang, T. Yan, J. Tian, Q. Hu, G. Wang, and Z. Li, "TOHIP: A topology-hiding multipath routing protocol in mobile ad hoc networks," *Ad hoc networks,* vol. 21, pp. 109-122, 2014.

[89] T. Smida, J. Babjak, and I. Dlouhy, "Prediction of fracture toughness temperature dependence from tensile test parameters," *kovove Materialy-Metallic Materials,* vol. 48, pp. 345-352, 2010.

[90] M. H. Hassoun, *Fundamentals of Artificial Neural Networks*: Massachusetts Institute of Technology, 1995.

[91] K. Kasiviswanathan, K. Sudheer, and J. He, "Quantification of Prediction Uncertainty in Artificial Neural Network Models," in *Artificial Neural Network Modelling*, ed: Springer, 2016, pp. 145-159.

[92] K. J. Hoon, C. D. Thanh, Z. Goangseup, L. W. Woo, and K. J. Sik, "Probabilistic fatigue integrity assessment in multiple crack growth analysis associated with equivalent initial flaw and material variability," *Engineering Fracture Mechanics,* vol. 156, pp. 182-196, 2016.

[93] H. Lee, *Bayesian nonparametrics via neural networks* vol. 13: SIAM, 2004.

[94] M. Maarouf, A. Sosa, B. Galván, D. Greiner, G. Winter, M. Mendez*, et al.*, "The Role of Artificial Neural Networks in Evolutionary Optimisation: A Review," in *Advances in Evolutionary and Deterministic Methods for Design, Optimization and Control in Engineering and Sciences*, ed: Springer, 2015, pp. 59-76.

[95] A. Powar and P. Date, "Modeling of microstructure and mechanical properties of heat treated components by using Artificial Neural Network," *Journal of Materials Science and Engineering,* vol. 628, pp. 89-97, 2015.

[96] A. Torre, F. Garcia, I. Moromi, P. Espinoza, and L. Acuña, "Prediction of compression strength of high performance concrete using artificial neural networks," *Journal of Physics: Conference Series,* vol. 582, pp. 1-6, 2015.

[97] A. Abdubaky, H. Bhadeshia, and T. Jabbar, "A Model for The Prediction of Fracture Toughness Using Neural Network," *Engineering and Technology Journal,* vol. 30, pp. 868-885, 2012.

[98] I. Dlouhý, "Recent Approaches of Evaluation of Brittle Fracture Properties of Steels (Key for Evaluation of Fracture Resistance of Weld Joints)," *In Weldability and properties degradation mechanisms of HAZ in Wled Joints.* : IBOK Bratislava, 2008.

AUTHOR'S PUBLICATIONS

1. AL KHADDOUR, S.; STRATIL, L.; VÁLKA, L.; DLOUHÝ, I. Prediction of fracture toughness transition from tensile test data using artificial neural networks. In Multi-Scale Design of Advanced Materials - conference proceedings. Brno: Brno University of Technology, 2016. pp. 79-86. ISBN: 978-80-214-5358- 6.
2. AL KHADDOUR, S.; DLOUHÝ, I. "Evaluation of Fracture Toughness by Master Curve Approach Using Compact Tension C(T) Specimens" Damascus University Journal of Engineering Science, 2015, vol. 2, pp. 63-73. ISSN: 1999-7302.
3. AL KHADDOUR, S., STRATIL,L., VÁLKA, L., DLOUHÝ, I. Correlation of reference temperature with general yield temperature for notched tensile specimens. In Multi-Scale Design of Advanced Materials - conference proceedings. Brno: Brno University of Technology, 2015. pp. 24-29. ISBN: 978-80-214-5146- 9.
4. STRATIL, L.; AL KHADDOUR, S.; HADRABA, H.; DLOUHÝ, I. Neural network prediction of fracture toughness from tensile test. Karlsruhe(SRN): 2010.

AUTHOR'S RESEARCH REPORTS

1. DLOUHÝ, I.; ČUPERA, P.; AL KHADDOUR, S.: Určení lomové houževnatosti oceli pro svařované rotory (Etapa III - dílčí zpráva pro VUT v Brně), HS 47/2012.
2. DLOUHÝ, I.; ČUPERA, P.; AL KHADDOUR, S.: Určení lomové houževnatosti oceli pro svařované rotory (Etapa IV - dílčí zpráva pro VUT v Brně), 47/2012.
3. DLOUHÝ, I.; ČUPERA, P.; AL KHADDOUR, S.: Určení lomové houževnatosti oceli pro svařované rotory (Etapa VI - dílčí zpráva pro VUT v Brně) HS47/2012
4. DLOUHÝ, I.; HADRABA, H.; CHLUP, Z.; ČUPERA, P.; AL KHADDOUR, S.: Podklady k výpočtům tahových zatěžovacích křivek z indentačních křivek a hodnocení stárnutí heterogenního svaru, technická zpráva pro ÚAM Brno - HS29/12.
5. DLOUHÝ, I.; HADRABA, H.; STODOLA, M.; ČUPERA, P.; AL KHADDOUR, S.: Hodnocení stárnutí heterogenního svaru na základě instrumentované indentace, technická zpráva pro ÚAM Brno - HS29/12.

LIST OF FIGURES

LIST OF TABLES

TERMS AND DEFINITIONS

Symbol	Unit	Designation
$\bar{y}$		Prediction of a committee of models
ε_{ij}	$[-]$	Strain tensor components
θ_J		Material properties that depend on microstructure and temperature
θ_K		Material properties that depend on microstructure and temperature
σ_f	$[MPa]$	Fracture stress for a penny-shaped crack
σ_{ij}	$[MPa]$	Stress tensor component
Δa	$[mm]$	Crack extension equal to $a - a_0$
A		Number of models in the committee
a_0	$[mm]$	Initial crack length
B	$[mm]$	Specimen thickness
b_0	$[mm]$	Original crack ligament
B_N	$[mm]$	Net section thickness for a side grooved specimen
C	$[mm]$	The length of the surface trace of the half penny crack
C_0	$[mm]$	The diameter of particle
D_r	$[mm]$	The diameter outside of neck
D_u	$[mm]$	The diameter in the narrowest part of the neck
E	$[GPa]$	Young's modulus
E_{bar}		Average size of error bars
E_D		Overall error
E_i		The error accompanying each prediction
F	$[N]$	Applied force
$f_{ij}(\theta)$	$[-]$	Dimensionless angular function

F_m		Yield of strength
F_{max}	$[N]$	Maximum value of force
F_Q	$[N]$	A provisional force
F_u		Fracture strength
G	$[GPa]$	Shear modulus
$g_{ij}(\theta)$	$[-]$	Dimensionless function
h_i		The hidden layer
J	$[kJ.m^{0.5}]$	Fracture resistance for a non-linear solid
J_e	$[kJ.m^{0.5}]$	Elastic component of J-integral
J_P	$[kJ.m^{0.5}]$	Plastic component of J-integral
K_0	$[MPa.m^{0.5}]$	A scale parameter equal to the fracture toughness corresponding to 63.2% failure probability
K_C	$[MPa.m^{0.5}]$	Critical value of K_I
K_I K_{II} K_{III}	$[MPa.m^{0.5}]$	Stress intensity factor for different modes
K_{IC}	$[MPa.m^{0.5}]$	K_c for Plane strain fracture toughness
K_{JC}	$[MPa.m^{0.5}]$	Elastic-plastic fracture toughness converted from critical J_c-integral values
$K_{JC(limit)}$	$[MPa.m^{0.5}]$	The limit of valid value of elastic-plastic fracture toughness
$K_{JC(med)}$	$[MPa.m^{0.5}]$	Fracture toughness median value
K_{min}	$[MPa.m^{0.5}]$	Minimum value of stress intensity factor
K_Q	$[MPa.m^{0.5}]$	A provisional value of K_{IC}
l		Model used to give the corresponding prediction y^l
l_0	$[mm]$	The characteristic distance ahead of the crack tip
m	$[-]$	Dimensionless constant
N		Total number of predictions

R, θ		Polar coordinate system
R_e	$[MPa]$	Yield strength
r_p	$[mm]$	Second-order plastic zone size or plastic rotation factor
R_{test}		The root mean square residual
R_y	$[MPa]$	The yield strength of a selected zone of the welded joint
r_y	$[mm]$	First-order plastic zone size
T	[℃]	Temperature
T_0	[℃]	Reference temperature
T_i		Traction components
t^k	$[-]$	Set of output
U_e	$[J]$	Elastic part of the area under curve of force versus load line displacement
u_i	$[mm]$	Displacement vector
U_P	$[J]$	Plastic part of the area under curve of force versus load line displacement
W	$[mm]$	Width of specimens
w	$[-]$	Elastic strain energy density
w_{ij}	$[-]$	Weights which define the network
x_i		Inputs
y^k		Set of corresponding network outputs
z		Output function
v	$[-]$	Poisson factor
Γ		The integration path around the crack tip
α, β		Control parameters which define the complexity of the program in ANN
δ	$[mm]$	Crack tip opening displacement (CTOD)

LIST OF ABBREVIATIONS

ANN	Artificial neural network
BCC	Body cantered cubic
CT	Compact tension specimen
CTOD	Crack tip opening displacement
DCT	Disc shape specimen
EPFM	Elastic plastic fracture mechanics
HAZ	Heat affected zone
HCP	Hexagonal close packed
KLST	Sub-sized precracked three-point bend specimen
LBZ	Local brittle zone
LEFM	Linear elastic fracture mechanics
LPE	Log predictive error
MCT	Modified compact tension specimen
MML	Method of maximum likelihood
RKR	Ritchie-Knott-Rice model
SENB	Single edge notched bend
SINTAP	Structural integrity assessment procedures
SPT	Small punch test
SSY	Small scale yielding

ANNEX:

Table 18 The ranking of the submodels depending on the LPE.

Number of submodel	Number of hidden units	Test error	Log predictive error
1	1	0.236	-1.11
2	2	0.353	-1.23
3	2	0.361	-1.33
4	2	0.332	-3.13
5	1	0.345	-3.69
6	1	0.346	-3.69
7	1	0.343	-3.71
8	1	0.347	-3.72
9	3	0.381	-6.43
10	3	0.519	-11.76
11	3	0.526	-13.02
12	2	0.603	-13.06
13	2	0.621	-14.22
14	4	0.63	-17.17
15	7	0.646	-17.84
16	5	0.649	-17.98
17	11	0.644	-18.15
18	5	0.662	-18.19
19	10	0.647	-18.36
20	16	0.647	-18.36
21	17	0.653	-18.63
22	17	0.644	-18.82
23	7	0.641	-18.89
24	15	0.642	-19.09

25	20	0.643	-19.09
26	13	0.642	-19.15
27	6	0.641	-19.17
28	14	0.63	-19.25
29	20	0.641	-19.32
30	13	0.639	-19.57
31	7	0.638	-19.72
32	8	0.64	-19.8
33	12	0.643	-19.83
34	18	0.633	-19.94
35	9	0.636	-20.08
36	11	0.637	-20.11
37	9	0.641	-20.2
38	5	0.636	-20.21
39	8	0.636	-20.21
40	11	0.641	-20.42
41	15	0.635	-20.6
42	12	0.629	-20.7
43	6	0.521	-20.79
44	6	0.609	-20.8
45	6	0.622	-20.81
46	19	0.635	-20.88
47	17	0.629	-20.9
48	5	0.61	-20.95
49	16	0.63	-20.96
50	16	0.617	-21
51	14	0.62	-21.03

52	14	0.634	-21.03
53	7	0.576	-21.07
54	4	0.586	-21.14
55	9	0.588	-21.14
56	14	0.625	-21.17
57	17	0.569	-21.25
58	15	0.61	-21.27
59	18	0.589	-21.31
60	10	0.624	-21.31
61	7	0.62	-21.32
62	19	0.598	-21.33
63	19	0.624	-21.41
64	11	0.622	-21.43
65	12	0.617	-21.5
66	16	0.579	-21.53
67	18	0.638	-21.56
68	13	0.586	-21.57
69	10	0.607	-21.59
70	18	0.599	-21.72
71	15	0.616	-21.78
72	12	0.573	-21.86
73	10	0.615	-21.88
74	9	0.621	-21.98
75	12	0.632	-21.99
76	10	0.613	-22.26
77	4	0.495	-22.32
78	13	0.508	-22.41

79	8	0.495	-22.47
80	11	0.544	-22.83
81	9	0.541	-22.87
82	16	0.536	-22.89
83	8	0.49	-23.6
84	20	0.519	-23.93
85	6	0.529	-23.94
86	3	0.517	-24.2
87	4	0.504	-25.25
88	8	0.511	-25.4
89	4	0.493	-27.99
90	5	0.464	-28.55
91	3	0.497	-33.54